Transformations of Gaussian laser beams via conical diffraction: Theory, Experiment and Applications

A thesis submitted for the degree of
Doctor in Philosophy

Trinity College Dublin

2011

Ciaran Phelan

Declaration

I declare that the work in this thesis has not been previously submitted as an exercise for a degree at this or any other University.

The work presented here is entirely my own except for the assistance mentioned in the acknowledgements and the collaborative work mentioned in the list of publications.

I agree that Trinity College library may lend or copy this thesis on request.

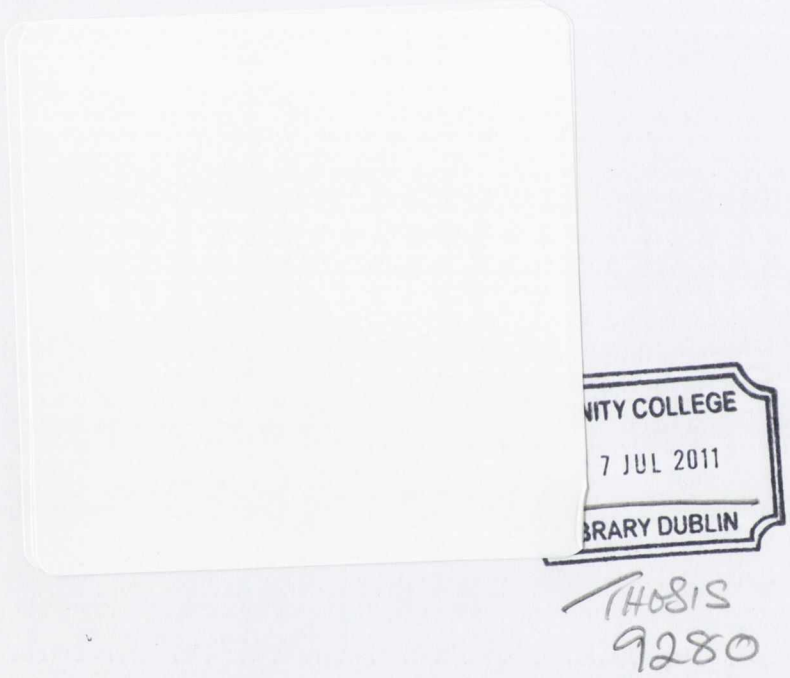

Published material included in the thesis

Aspects of the following published material are included in this thesis:

Publications:

Phelan, C. F., O'Dwyer, D. P., Rakovich, Y. P., Donegan, J. D., & Lunney, J. G. (2009). Conical diffraction and Bessel beam formation with a high optical quality biaxial crystal. *Optics Express, 17*, 12891.

O'Dwyer, D. P., Phelan, C. F., Rakovich, Y. P., Eastham, P. R., Lunney, J. G., & Donegan, J. F. (2010). Generation of continuously tunable fractional optical orbital angular momentum using internal conical diffraction. *Optics Express, 18* (16), 16480-16485.

Conference presentations:

Phelan, C. F., O'Dwyer, D. P., & Lunney, J. G., Donegan, J. D., Rakovich, Y. P., Conical diffraction and Bessel beam formation with a high quality biaxial crystal. Poster presention at the Photonics Ireland conference, Kinsale, Cork, September 2009.

Phelan, C. F., O'Dwyer, D. P., Rakovich, Y. P., Donegan, J. D., Lunney, J. G. , Conversion of spin to orbital angular momentum and creation and annihilation of optical vortices via conical diffraction. Poster presentation at the International Conference on Orbital Angular Momentum (ICOAM), York University, April 2010.

Acknowledgements

I wish to acknowledge the following people who made valuable contributions to the work presented here:

My supervisor Professor James Lunney and co-supervisor Professor John Donegan, both of whom provided valuable ideas for, and criticisms of my work at every stage of its development; I especially want to thank Prof. Lunney for providing me with the opportunity to do the research reported in thesis.

My colleague David O'Dwyer with whom I worked closely on many aspects of the work presented here, especially the experimental parts;

Dr. Yuri Rakovich for his advice and participation in the research of our group during the time I spent here;

The semi-conductor photonics group;

Dr. Richard Winfield of the Tyndall National Institute with whom the work on two photon polymerization was collaborated on;

Dr. Paul Eastham for helpful discussions and clarifications;

Professor Sir Michael Berry for helpful correspondences (and for formulating paraxial conical diffraction theory in the form in which it is used here);

Professor Kishan Dholakia and Dr Tomas Cizmar of St. Andrews University for helping with the production of non-diverging beams and allowing us to use their facilities;

My internal examiner Dr. Eric Finch for his advice on presentation;

I would also like to thank my parents for their support and encouragement during the course of my research.

This research was funded by Science Foundation Ireland.

The work on two-photon polymerization carried out at Tyndall National Institute was funded by The National Access Program.

Summary of results obtained and methods used

The work reported in this thesis concerns the shaping of Gaussian laser beams using conical diffraction. Conical diffraction is the extension to wave optics of internal conical refraction, in which a ray of light incident along the optic axis of a biaxial crystal is converted into a hollow cone of light within the crystal and refracted into a hollow cylinder on exiting the crystal.

The predictions of the paraxial optics theory of conical diffraction are tested in the laboratory for a range of Gaussian beam parameters. Simple optical arrangements involving conical diffraction are used to transform a standard Gaussian beam into a range of useful laboratory beams including non-diverging zeroth and first order Bessel beams. These transformations exploit the strong dependence of the conically diffracted Gaussian on the incident beam waist as well as its unique polarization profile.

Next, the paraxial optics theory is extended to the case of conical diffraction by two crystals in series, or cascade. The main predictions regarding the polarization and intensity profiles of the cascade conically diffracted beams are confirmed by experiment for the cases of two biaxial crystals with a relative rotation between the crystals and for the separate cases of two biaxial crystals having equivalent and distinct conical refraction parameters.

An optical arrangement consisting of just a single biaxial crystal and a Mach-Zehnder interferometer is used to convert a linearly polarized Gaussian beam into a radially or azimuthally polarized beam. Two qualitatively distinct methods are used to achieve this.

Finally, the ring and Bessel-like profiles associated with the near and far field regions of conically diffracted Gaussian are used to write micron scale objects via two photon polymerisation with a femto-second laser. The potential of the first order component to write tube like structures was investigated.

Contents

Chapter 1. Introduction

The purpose of this chapter is to develop the paraxial theory of conical diffraction which will be used throughout this thesis. A brief summary of the fascinating historical context of the discovery of conical refraction is presented, followed by an account of more recent work on the phenomenon in the first section. In Section 1.2 the optical properties of biaxial crystals are introduced in terms of electromagnetic theory. The dispersion surface, described by Fresnel's equation, is derived and discussed. Internal conical refraction is shown to occur when a wave is incident along the optic axis of a biaxial crystal in Section 1.3. In Section 1.4 conical refraction of a wave is extended to conical diffraction of a general paraxial superposition of plane waves. Integral expressions that relate the incident paraxial beam to the conically diffracted beam are obtained.

1.1. History

Hamilton's prediction, and Lloyd's subsequent experimental confirmation, of conical refraction in 1832 marked a significant event in the development of the transverse wave theory of light, (Hamilton, 1837), (Lloyd, 1833). The phenomenon, which involves the transformation of a light ray, incident along an optic axis of a transparent biaxial crystal, into a hollow cone of light, had never before been observed and was shown by Hamilton to be a direct consequence of Fresnel's transverse wave theory of light.

The transverse wave theory of light that Hamilton used to predict conical refraction was the result of a series of refinements made to Huygens's principle to take into account the effects of polarization and diffraction. In 1672 Huygens proposed that light propagates as a wave in the æther with every point on the wave-front serving as a source of secondary wavelets and with the envelope of these wavelets forming the wave-front at a later time. Based on this principle he was able to derive the laws of reflection, refraction and propagation of light. He was also able to show that a light source in medium that is anisotropic with respect to the speed of light will spread into two waves, with one being spherical and the other ellipsoidal (Huygens, 1690). This last theoretical discovery explained the results of Bartholinus who had observed double refraction in Iceland spar (calcite) (Bartholin, 1669). Huygens can be considered as the discoverer of polarization as he noted that when a calcite crystal is rotated about the direction

of propagation of the ordinary or extraordinary ray emerging from another crystal of calcite, the ordinary ray is blocked by the second crystal at one angle and the extraordinary ray is blocked by the second crystal at the orthogonal angle.

Over a century later Augustin-Jean Fresnel incorporated Thomas Young's principle of interference into Huygens' principle to explain diffraction phenomena within the wave theory of light (1818) (Fresnel, 1866). A few years after this, Fresnel discovered experimentally that light rays polarized orthogonally to each other could not interfere. Thomas Young realized that this could be explained if light was composed of transverse waves (Buchwald, 1989). The idea of light as a transverse vibration in the æther, combined with the Huygens-Fresnel principle, provided the foundations of Fresnel's theoretical explanation of the phenomena of crystal optics including double refraction. He was able to show that anisotropic crystals (describing a crystal as being anisotropic with respect to the velocity of light means that light will propagate in the crystal at a speed determined by the direction in which the light is travelling) could be divided into three classes and in the case of maximum anisotropy a source within the crystal would spread in all directions with a complex two sheeted surface (in 3D space) as wave-front. For every direction in the crystal there were two possible waves, each linearly polarized in a specific direction. The direction of the light energy or ray would, in general, be different to that of the corresponding wave.

Fresnel did not seem to notice that at four points along two axes (optic axes) on his wave-surface, the two sheets met and there was only one possible wave. At these points all polarizations were permissible. In 1832 Hamilton used his method of geometrical optics to investigate the ray (or energy) directions associated with waves along these optic axes. He was able to show that the rays associated with a wave along one of the optic axes lay on the surface of a cone and were linearly polarized with a half turn of polarization in a circuit of the cone's axis (Hamilton, 1837). Hamilton's colleague Humphrey Lloyd experimentally verified Hamilton's prediction later that year (Lloyd, 1833).

Despite the fact that Hamilton's formulation of conical refraction took into account the transverse wave nature of light, it was still somewhat of an idealisation. This was because an incident infinitely thin, perfectly collimated, geometric ray is physically unrealistic. We now know that any realistic light beam will be a superposition of waves over a range of directions, with a minimum thickness or waist depending on the wavelength of the light. Evidence that Hamilton had not uncovered the full story emerged in the form of more accurate experiments (Potter, 1841) that showed that a cross-section of the cylinder that emerges from a biaxial

crystal is in fact two concentric rings of light surrounding a dark ring. This result was explained by Voigt (Voigt, 1905). Recently a comprehensive paraxial optics formulation of conical diffraction (diffraction rather than refraction since the paraxial theory predicts the observed diffraction effects) has emerged with the initial results of Belskii et al (Belskii & Khapalyuk, 1978(a)), (Belskii & Khapalyuk, 1978(b)) being elegantly reformulated by Berry who views propagation along the optic axis of the biaxial crystal as a linear Hamiltonian operator that transforms the state on the incident paraxial beam into a diffracting double ring (Berry, 2004). Berry's equations describing the intensity profiles of the evolving conically diffracted Gaussian have been shown to agree with experiment to a high degree of accuracy (Phelan, O'Dwyer, Rakovich, Donegan, & Lunney, 2009).

1.2. Crystal optics

The purpose of this section is to express Fresnel's theory of the interaction of light with anisotropic media in the language of modern electromagnetic theory. In order to do this we consider the case of a plane wave that satisfies Maxwell's equations propagating in a general direction in an electrically anisotropic medium. The treatment below is based on that given in (Landau, Lifshitz, & Pitaevskii, 1984).

When an electrically anisotropic medium is exposed to an electric field, positive and negative charges separate causing a dipole moment. The anisotropic dipole moment per unit volume is called the polarization $\vec{P}$ and it is given by

$$\vec{P} = (\epsilon - \epsilon_0)\vec{E} = \vec{D} - \varepsilon_0\vec{E} \qquad 1.2.1.$$

If we presume that this polarization is linearly related to the applied electric field then $\vec{E}$ & $\vec{D}$ must be related by a linear transformation. In index notation with i and j running between 1 and 3, and with the convention that we sum over repeated indices in operation, we write this transformation as

$$D_i = \varepsilon_{ij}E_j \qquad 1.2.2.$$

It can be shown that the 3 x 3 matrix that represents ε_{ij}must be real and symmetric (Born & Wolf, 2001). This implies that ε_{ij} can be written as a diagonal matrix. The co-ordinate system in which ε_{ij} is diagonal is referred to as the principal dielectric co-ordinate system. In this co-ordinate system, the diagonal elements of ε_{ij}, ($\varepsilon_{11} \equiv \varepsilon_1, \varepsilon_{22} \equiv \varepsilon_2, \varepsilon_{33} \equiv \varepsilon_3$), are referred to as the principal dielectric constants with the principal refractive indices, n_i, defined as

$$\varepsilon_i = n_i^2, \qquad 1.2.3.$$

with i running from 1 to 3.

Maxwell's equations for the medium defined by equation 1.2.2 are

$$\vec{\nabla} \cdot \vec{D} = \rho, \qquad 1.2.4.$$

$$\vec{\nabla} \cdot \vec{B} = 0, \qquad 1.2.5.$$

$$\vec{\nabla} \times \vec{E} = -\partial_t \vec{B}, \qquad 1.2.6.$$

$$\vec{\nabla} \times \vec{H} = \partial_t \vec{D}. \qquad 1.2.7.$$

In the case of a monochromatic plane wave with electric field of the form

$$\vec{\mathrm{E}}(\mathrm{r},\mathrm{t}) = \overrightarrow{\mathrm{E}_0} \times \exp\left(i(\vec{k}.\vec{r} - \omega t)\right) \qquad 1.2.8.$$

where $\vec{k}$ is the wave vector inside the anisotropic medium (we will denote the free space wave vector as $\overrightarrow{k_0}$), equations 1.2.6 and 1.2.7 become

$$\vec{\mathrm{k}} \times \vec{E} = \omega \vec{B} \qquad 1.2.9.$$

$$\vec{\mathrm{k}} \times \vec{H} = -\omega \vec{D} \qquad 1.2.10.$$

Examining equations 1.2.9 and 1.2.10, it is seen that the relation between the quantities $\vec{E}, \vec{D}, \vec{k}$ and the Poynting vector $\vec{S} = \frac{1}{\mu_0} \vec{E} \times \vec{B}$ is as depicted in Fig 1.2.1

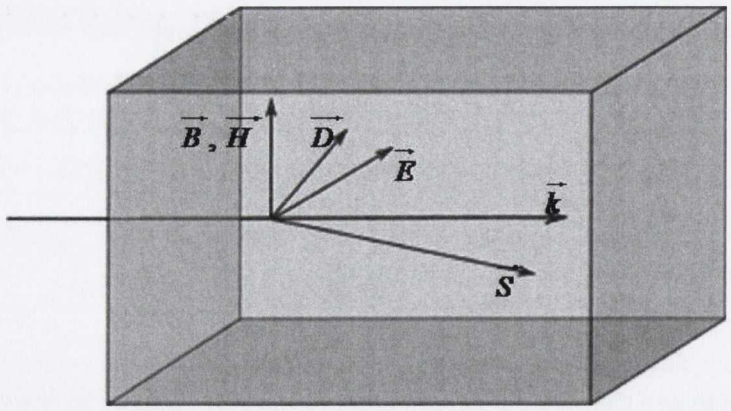

Fig 1.2.1 The relative orientations of $\vec{E}$, $\vec{D}$, $\vec{S}$ and $\vec{k}$ for a wave in a biaxial medium (grey cuboid). The electric field $\vec{E}$ is orthogonal to the Poynting vector $\vec{S}$ while the electric displacement $\vec{D}$ is orthogonal to the wave-vector $\vec{k}$.

Next we define $\vec{\eta} = {}^{1}/_{k_0}\,\vec{k}$ as a vector that points in the same direction as the wave vector, $\vec{k}$, and has a magnitude equal to the refractive index (i.e. $\sqrt{\eta_1^2 + \eta_2^2 + \eta_3^2} = \eta = n$). Combining equations 1.2.9 & 1.2.10 to eliminate $\vec{H}$, and using the definition of $\vec{\eta}$, leads to

$$\vec{D} = \vec{\eta} \times (\vec{E} \times \vec{\eta}) = \eta^2 \vec{E} - (\vec{\eta} \cdot \vec{E})\vec{\eta}. \qquad 1.2.11.$$

Applying the relation 1.2.2 to 1.2.11 we have

$$(n^2 \delta_{ij} - \eta_i \eta_j - \varepsilon_{ij}) E_j = 0, \qquad 1.2.12.$$

where we have replaced η^2 with n^2. Equation 1.2.12 can be written in matrix form as

$$\begin{pmatrix} n^2 - \eta_1^2 - \varepsilon_1 & -\eta_1\eta_2 & -\eta_1\eta_3 \\ -\eta_2\eta_1 & n^2 - \eta_2^2 - \varepsilon_2 & -\eta_2\eta_3 \\ -\eta_3\eta_1 & -\eta_3\eta_2 & n^2 - \eta_3^2 - \varepsilon_3 \end{pmatrix} \begin{pmatrix} E_1 \\ E_2 \\ E_3 \end{pmatrix} = 0, \qquad 1.2.13.$$

where ε_{ij} has been expressed in principal dielectric co-ordinates.

Equation 1.2.13 has non-trivial solution only if the determinant of the 3 x 3 matrix vanishes. Setting this determinant to zero, we arrive at:

$$\begin{aligned} n^2(\varepsilon_1\eta_1^2 + \varepsilon_2\eta_2^2 + \varepsilon_3\eta_3^2) \\ - \big(\varepsilon_1\eta_1^2(\varepsilon_2 + \varepsilon_3) + \varepsilon_2\eta_2^2(\varepsilon_1 + \varepsilon_3) \\ + \varepsilon_3\eta_3^2(\varepsilon_1 + \varepsilon_2)\big) + \varepsilon_1\varepsilon_2\varepsilon_3 = 0. \end{aligned} \qquad 1.2.14.$$

Equation 1.2.14 is the electromagnetic form of Fresnel's equation, describing light propagation in anisotropic media.

We will examine the most general case, that in which all three principal dielectric indices (and hence principal refractive indices) are different. With $\varepsilon_1 < \varepsilon_2 < \varepsilon_3$, Fresnel's equation describes a double sheeted surface in direction space. Figure 1.2.2 shows a plot of this surface ($n$as a function of $\vec{\eta}$) in direction space ($\eta_1 - \eta_2 - \eta_3$ space).

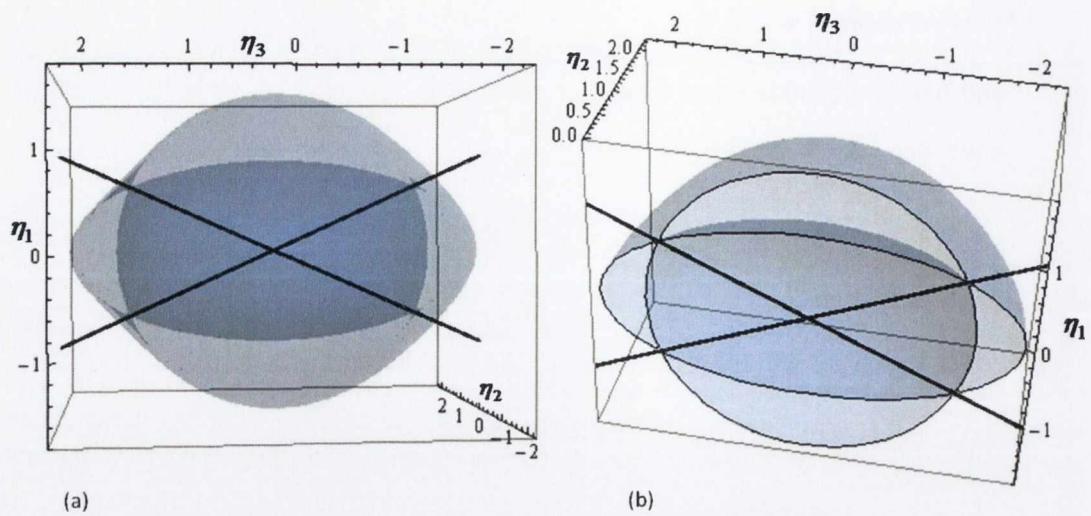

Fig 1.2.2 (a) The two sheeted dispersion surface plotted for a medium with principal refractive indices of 1, $\sqrt{3}$ and $\sqrt{5}$. (b) The same surface plotted with the co-ordinate η_3 running from 0 to 3 to show the inside of the wave surface and the points where it intersects itself.

The fact that the dispersion surface is two sheeted implies that there are two indices of refraction for every direction in the crystal except for the two points where the surfaces meet where there is only one index of refraction. The directions corresponding to the points of intersection are called the optic axes and the fact that there are two of them is the reason we call media with these wave surfaces biaxial.

The polarizations of the waves that can propagate in a given direction in the biaxial medium are also determined by Fresnel's equation. If we consider a plane wave in the biaxial crystal in a co-ordinate system with one of the Cartesian axes, say the 3 – axis, along the wave vector then $\vec{D}$, which is orthogonal to $\vec{\eta}$, lies in the 1,2 plane. Thus, using equation 1.2.2, we can re-write equation 1.2.12 as

$$\left({}^{1}/_{n^2}\,\delta_{ij} - \varepsilon_{ij}^{-1}\right) D_j = 0, \qquad 1.2.15.$$

with the indices *i,j* running from 1 to 2.

The implications of this equation are more obvious when it is written in matrix form

$$\begin{pmatrix} {}^{1}/_{n^2} - \varepsilon_{11}^{-1} & \varepsilon_{12}^{-1} \\ \varepsilon_{21}^{-1} & {}^{1}/_{n^2} - \varepsilon_{22}^{-1} \end{pmatrix} \begin{pmatrix} D_1 \\ D_2 \end{pmatrix} = 0. \qquad 1.2.16.$$

We can see from equation 1.2.15 that the two $\vec{D}$ vectors permitted are polarised along the principal axes of the ellipse defined by the 2 x 2 matrix in equation 1.2.16 and, thus, are orthogonal to each other. Thus for each direction in the crystal, two orthogonally polarized waves are allowed to propagate. As we have seen, If the beam is directed along the optic axis,

there is only one value for n. This implies that all linear polarizations are permissible since the ellipse defined by the 2 x 2 matrix in equation 1.2.16 will have degenerated into a circle.

It was mentioned earlier that the direction of energy propagation is generally not the same as the wave vector direction. It can be shown that the direction of energy flow, or ray direction, associated with a given wave vector direction is orthogonal to a tangent to the dispersion surface at the point defined by that wave vector (Landau, Lifshitz, & Pitaevskii, 1984). In the next section we will look at the behaviour of the normals to the dispersion surface in the region of direction space surrounding the optic axis.

1.3. Conical refraction

In the previous section it was mentioned that there are directions in the crystal where the two sheets of the dispersion surface meet. In this section we investigate what happens when a ray is incident along one of these directions (optic axes). **Fresnel's equation (equation 1.2.14)** implies that in the case of $\varepsilon_1 < \varepsilon_2 < \varepsilon_3$, the optic axes are situated in the $\{\eta_1, \eta_3\}$ plane with the co-ordinates of the points of intersection given by

$$\eta_1^2 = \frac{\varepsilon_3(\varepsilon_2 - \varepsilon_1)}{\varepsilon_3 - \varepsilon_1}, \eta_3^2 = \frac{\varepsilon_1(\varepsilon_3 - \varepsilon_2)}{\varepsilon_3 - \varepsilon_1}. \qquad 1.3.1.$$

The angle, α, that these optic axes make with the η_3 axis is given by

$$\pm\tan\alpha = {}^{\eta_1}/_{\eta_3} = \pm\sqrt{\frac{\varepsilon_3(\varepsilon_2 - \varepsilon_1)}{\varepsilon_1(\varepsilon_3 - \varepsilon_2)}}. \qquad 1.3.2.$$

In Figure 1.3.1, the dispersion surface is plotted in the positive quadrant of the $\{\eta_1, \eta_3\}$plane with the optic axis shown.

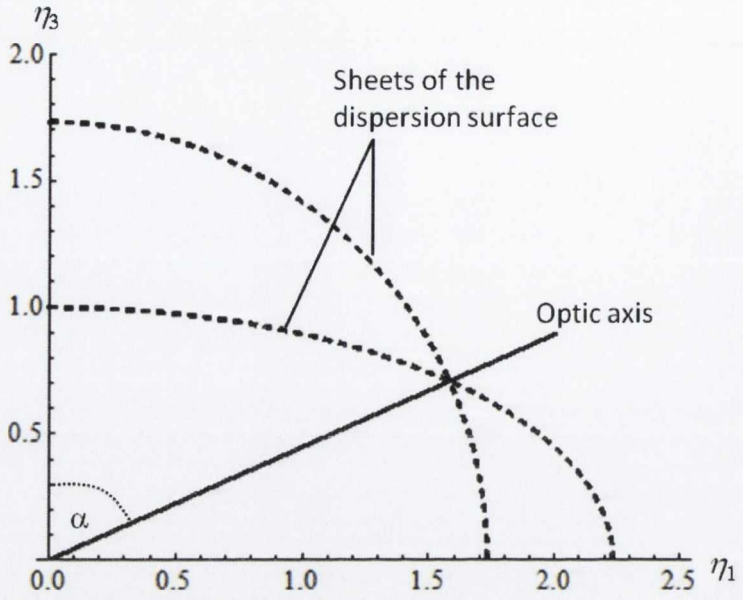

Figure 1.3.1: A section of the dispersion surface in the $\{\eta_1, \eta_3\}$ plane showing the orientation of the optic axis. The values used of the principal refractive indices used in this plot are 1, $\sqrt{3}$ and $\sqrt{5}$.

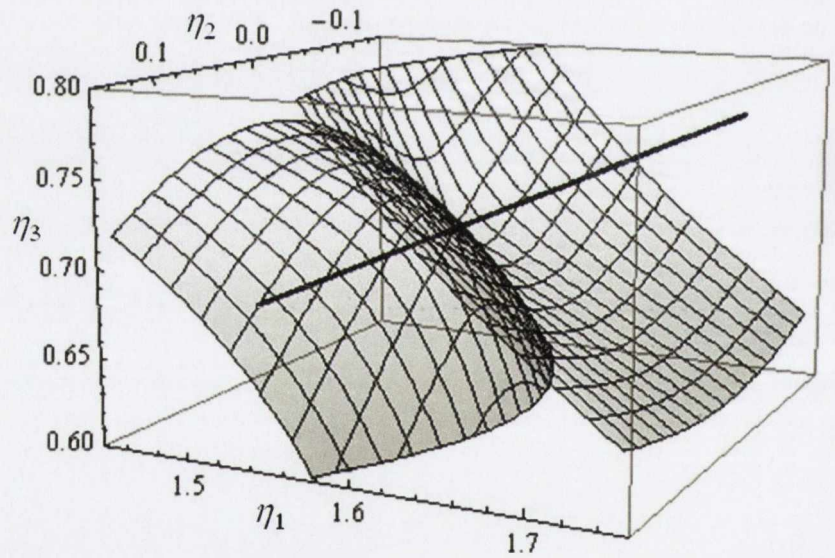

Figure 1.3.2: The wave surface in a small area of direction space near the optic axis (black line).

It was noted in the previous section that the ray direction associated with a given wave direction in the biaxial medium is orthogonal to the tangent to the dispersion surface at the point on the dispersion surface to which that wave corresponds. However, the normal to the dispersion surface is undefined at the optic axis. In order to find out the ray directions for a wave directed along the optic axis, we can examine the dispersion surface in a small region surrounding the optic axis. Figure 1.3.2 shows a 3D plot of the dispersion surface in a region of direction space near the optic axis for the same parameters used for Figure 1.3.1.

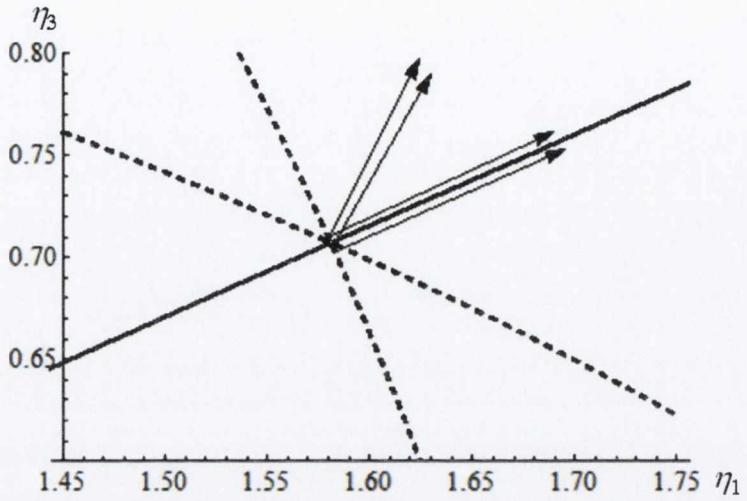

Figure 1.3.3: A section of the two sheeted dispersion surface near the conical intersection. The arrows are orthogonal to the dispersion surface at points very close to the optic axis. The section of the dispersion surface is a close up the same dispersion surface shown in Figure 1.3.1.

Figure 1.3.3 shows a two dimensional section of the dispersion surface near the optic axis. It can be seen from the figure that the shape of the dispersion surface is approximately a double cone. It follows that the orthogonal directions to it will also form a cone.

This can be made more precise in the following way: First we rotate the co-ordinate system so that the optic axis is along the η_3-axis. Next we switch to the spherical polar co-ordinates shown in Figure 1.3.4

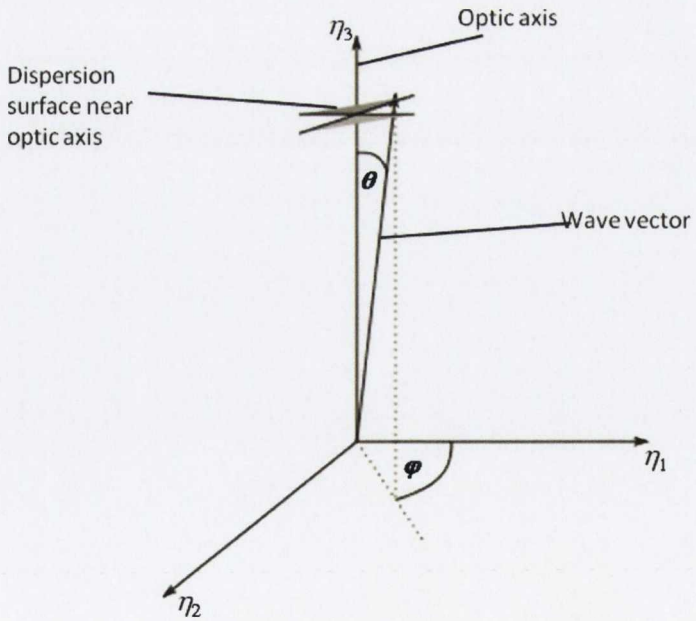

Figure 1.3.4: Spherical polar co-ordinates in direction space with the optic axis aligned with η_3 axis. The dispersion surface near the conical intersection is shown intersecting the η_3 axis.

A wave vector directed off optic axis by angle θ has the form

$$\frac{\omega}{k}\vec{\eta} = nk_0 \begin{pmatrix} \cos\theta \\ \sin\theta\sin\phi \\ \sin\theta\cos\phi \end{pmatrix}. \qquad 1.3.3.$$

Assuming θ to be small we have

$$\frac{\omega}{k}\vec{\eta} = nk_0 \begin{pmatrix} \left(1-\frac{1}{2}\theta^2\right) \\ \theta\sin\phi \\ \theta\cos\phi \end{pmatrix}. \qquad 1.3.4.$$

It can been shown, (Portigal & Burstein, 1969) (Berry & Dennis, 2003), that if we insert these wave vector components into the Fresnel equation (equation 1.2.14) and assume small differences between the principal refractive indices, then solving Fresnel's equation for n leads to

$$n_{\pm}(\theta) = n_2(1 + A\theta\cos\phi \pm A\theta), \qquad 1.3.5.$$

where

$$A = \frac{1}{n_2}\sqrt{(n_2 - n_1)(n_3 - n_2)}. \qquad 1.3.6.$$

This describes a double cone with cone half angle $\frac{\pi}{2} - A$ which leads us to expect that the normals to this surface near the conical point will form a cone with half angle A. Figure 1.3.5 shows the eigen-value surfaces (two-sheeted dispersion surface), defined by equation 1.3.5, plotted for a few different values of the parameter A, which is a measure of the anisotropy of the biaxial medium.

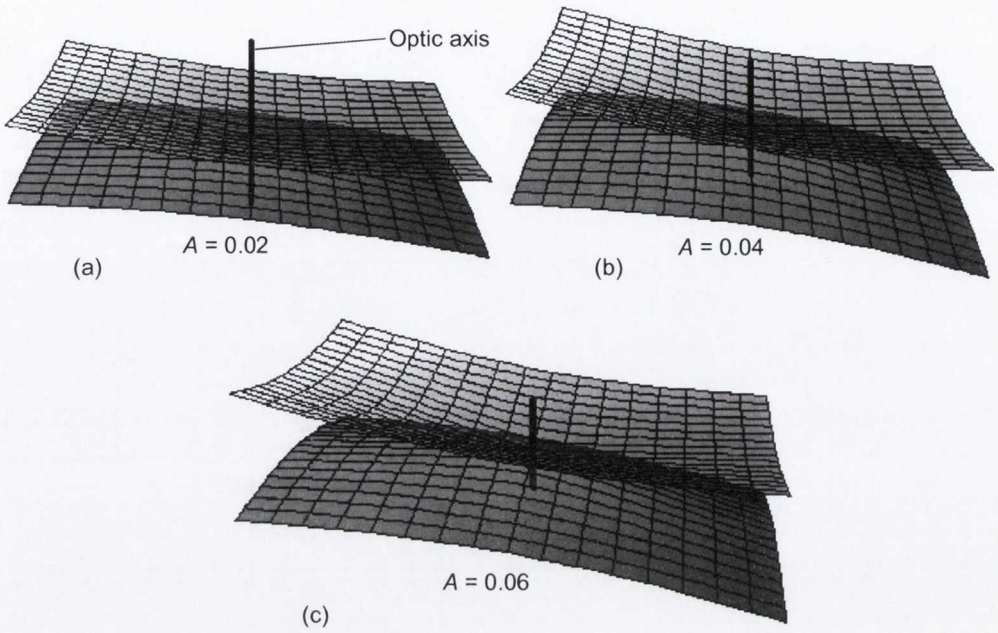

Figure 1.3.5: The eigen-value surfaces (dispersion surfaces) near the conical intersection (the black line is the optic axis) calculated from approximation 1.3.6 for a range of values of A. The double cone becomes more apparent as A, the biaxiality parameter is increased.

The eigen polarizations for each of these eigenvalues ($n_{\pm}(\theta)$) can also be calculated from Fresnel's equation and the result is given by

$$\overrightarrow{D_+} = D\overrightarrow{e_+} = D\begin{pmatrix}\cos\frac{1}{2}\phi\\ \sin\frac{1}{2}\phi\end{pmatrix}, \qquad 1.3.7.$$

$$\overrightarrow{D_-} = D\overrightarrow{e_-} = D\begin{pmatrix}\sin\frac{1}{2}\phi\\ -\cos\frac{1}{2}\phi\end{pmatrix}. \qquad 1.3.8.$$

Thus there are two orthogonally polarized eigen-modes for a wave directed off axis by θ with the eigen-polarizations undergoing a π rotation as the off axis wave vector direction is rotated (i.e. ϕ is varied) about the optic axis. The Poynting vector can be calculated for each eigen polarization via Maxwell's equations and the result (Portigal & Burstein, 1969) is

$$\overrightarrow{P_\pm} \propto \begin{pmatrix}2A\cos^2\frac{\phi}{2} \pm \theta\cos\phi\\ \pm 2A\cos\frac{\phi}{2}\sin\frac{\phi}{2} + \theta\sin\phi\\ 1\end{pmatrix} \qquad 1.3.9.$$

The two ($\pm$) modes are plotted in Figure 1.3.6 as the off axis-angle θ is varied between 0.1 and zero radians. The result shows two concentric cones with a common origin that gradually merge into one cone as θ goes to zero. This result can be interpreted as follows: Each wave incident at a slight angle to the optic axis is double refracted. The envelope of all the double refracted rays forms a double cone as the off-axis component of the incident wave is rotated

from zero to 2π in the $\{r, \phi\}$ plane. As the incident wave vector is brought closer to the optic axis the double cone merges into the cone corresponding to the singular case of conical refraction.

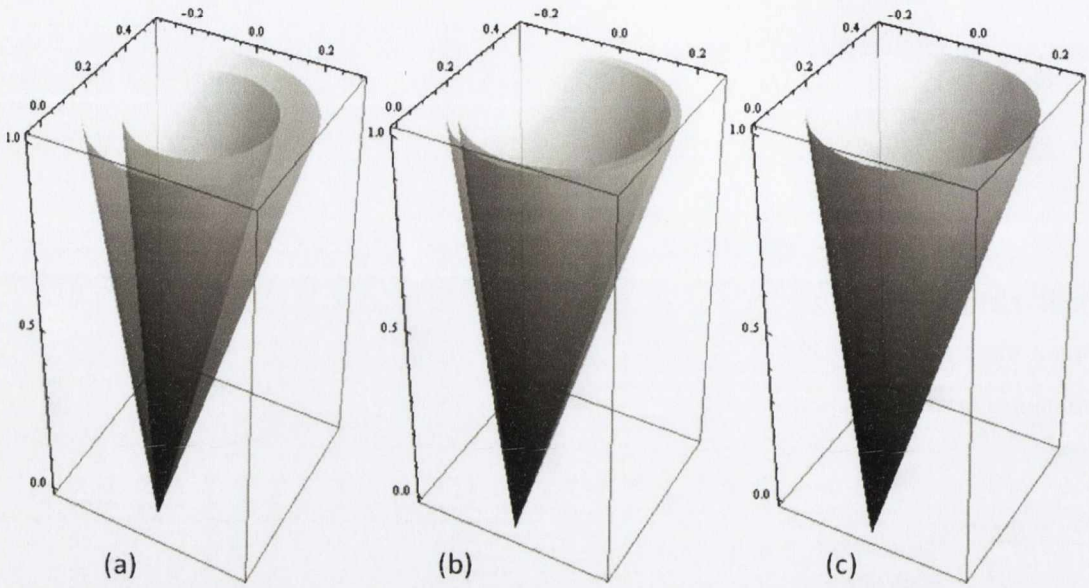

Figure 1.3.6: The cones of refraction that the two Poynting vector modes sweep out as ϕ is varied between zero and 2π. The cone of refraction is obtained as the off-axis angle θ goes to zero. The off axis angles were (a) 0.1; (b) 0.05 and (c) 0 radians respectively.

1.4. Paraxial optics and conical diffraction

It was demonstrated in the last section that the cone of refracted rays can be viewed as the envelope of double refracted rays with wave vectors at a given angle to the optic axis in the limiting case of that angle going to zero. However a realistic light beam will always be composed of a superposition of plane waves spanning a range of directions. This means that a finite area of the wave vector surface will have to be considered rather than just the wave vectors at a certain small angle to the optic axis or exactly along the optic axis, i.e. diffraction theory is required.

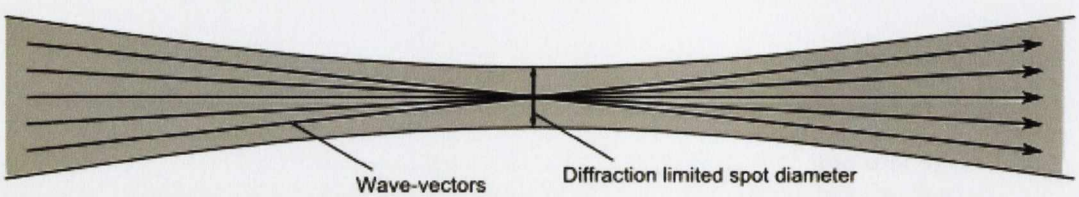

Figure 1.4.1: A beam composed of a superposition of plane waves with a small range of directions centred on the propagation direction of the beam.

Since the fine features of conical diffraction can only be observed with highly directional light sources it makes sense to incorporate wave effects into conical refraction in the paraxial regime. Berry and Jeffrey have also shown that the paraxial approximation leads to a considerable simplification of the analysis (Berry, 2004), (Berry & Jeffrey, 2007).

In the following discussion the *z* axis will be the propagation direction of our paraxial beam with small transverse components in the *x* and *y* directions. We first write the wave vector of a plane wave in an isotropic medium as

$$\vec{k} = |\vec{k}|\hat{k} = k\hat{k} = \begin{pmatrix} k_x \\ k_y \\ \sqrt{k^2 - (k_x^2 + k_y^2)} \end{pmatrix} = \begin{pmatrix} \overrightarrow{k_t} \\ k_z \end{pmatrix} \qquad 1.4.1.$$

The phase associated with this wave vector is:

$$\vec{k} \cdot \vec{r} = k_x x + k_y y + z\sqrt{k^2 - (k_x^2 + k_y^2)}. \qquad 1.4.2.$$

We want to specify that the *z* component of this beam has a much bigger magnitude than the transverse components so we write the transverse part of the wave vector as:

$$\overrightarrow{k_t} = \begin{pmatrix} k_x \\ k_y \end{pmatrix} = k \begin{pmatrix} P_x \\ P_y \end{pmatrix}, \qquad 1.4.3.$$

with $P = \sqrt{P_x^2 + P_y^2} \ll 1$ (in the spherical polar co-ordinates used in the last section we would have $\vec{P} = \begin{pmatrix} \theta \cos\phi \\ \theta \sin\phi \end{pmatrix}$ with $\theta \ll 1$). Assuming small transverse components allows us to expand the square root in equation 1.4.2 as follows:

$$k_z = \sqrt{k^2 - k^2(P_x^2 + P_y^2)} \approx k - \frac{1}{2}kP^2. \qquad 1.4.4.$$

The substitution:

$$k_j \to i\partial_j, \qquad 1.4.5.$$

where *j* represents each Cartesian co-ordinate, leads to the paraxial wave equation

$$(\partial_x^2 + \partial_y^2 + k)\vec{E} = 2ik\partial_z\vec{E}. \qquad 1.4.6.$$

This equation has solutions of the form:

$$\exp\left(i(k\vec{P}\cdot\vec{r}-\frac{1}{2}kP^2z)\right)\exp\left(ikz\right) \qquad 1.4.7.$$

The paraxial wave equation can be recast in the Hamiltonian form:

$$\left(\partial_x^2+\partial_y^2\right)\vec{E}=k^2P^2\boldsymbol{I}\vec{E}=\boldsymbol{H}\vec{E}=2ik\partial_z\vec{E}\,, \qquad 1.4.8.$$

where $\boldsymbol{I}$ is the two by two identity matrix. The Hamiltonian for free space paraxial propagation can be generated from any two orthogonal polarization states. In a basis of linear polarizations it is just the identity matrix $\boldsymbol{I}$. The solution to the Hamiltonian equation 1.4.8 is

$$E(\vec{r},z)=\exp\left(ik\boldsymbol{H}(z-z_0)\right)E(\vec{r},z_0). \qquad 1.4.9.$$

Now we will derive the Hamiltonian equation for propagation through a biaxial crystal along the optic axis. The plane waves that can propagate in the crystal in the vicinity of the optic axis are given (Berry, 2004) by:

$$\exp\left(ik(\vec{P}\cdot\vec{r}+z(P^2\pm AP))\right)\overrightarrow{e_\pm}, \qquad 1.4.10.$$

where

$$\overrightarrow{e_+}=\begin{pmatrix}\cos\frac{1}{2}\varphi_P\\ \sin\frac{1}{2}\varphi_P\end{pmatrix}\text{ and }\overrightarrow{e_-}=\begin{pmatrix}\sin\frac{1}{2}\varphi_P\\ -\cos\frac{1}{2}\varphi_P\end{pmatrix}. \qquad 1.4.11.$$

The plane waves described by equation 1.4.10 and 1.4.11 are written using the cone centred cylindrical polar co-ordinates in Figure 1.4.2.

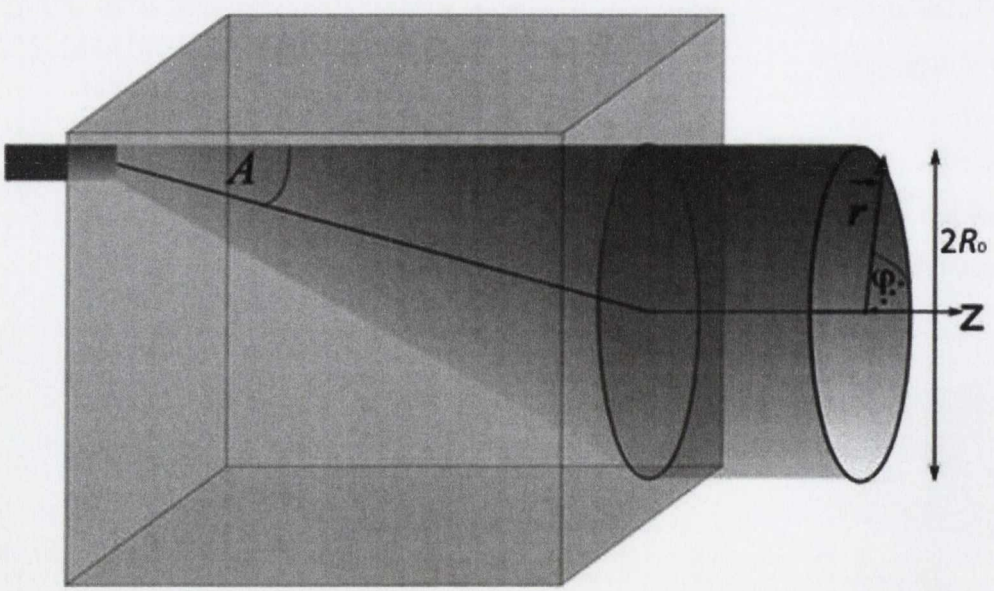

Figure 1.4.2: The geometry of conical refraction/diffraction. The real space co-ordinates in which the conically diffracted electric field in described are shown on the diagram.

From these orthogonal eigenstates we can construct the Hamiltonian $\boldsymbol{H}(\vec{P})$ that determines the propagation of the beam in the crystal for all directions in a region of direction space centred on the optic axis. It is:

$$\boldsymbol{H}(\vec{P}) = (P^2 + AP)\begin{pmatrix}\cos\frac{1}{2}\varphi_P \\ \sin\frac{1}{2}\varphi_P\end{pmatrix}\left(\cos\tfrac{1}{2}\varphi_P \quad \sin\tfrac{1}{2}\varphi_P\right) + \\ ((P^2 - AP)\begin{pmatrix}\sin\frac{1}{2}\varphi_P \\ -\cos\frac{1}{2}\varphi_P\end{pmatrix}\left(\sin\tfrac{1}{2}\varphi_P \quad -\cos\tfrac{1}{2}\varphi_P\right). \qquad 1.4.12.$$

Multiplying out equation 1.4.12 leads to

$$\boldsymbol{H}(\vec{P}, z) = P^2\boldsymbol{I} + AP\begin{pmatrix}\cos\varphi_P & \sin\varphi_P \\ \sin\varphi_P & -\cos\varphi_P\end{pmatrix} = P^2\boldsymbol{I} + AP\boldsymbol{M}(\varphi_P), \qquad 1.4.13.$$

where here, and hereafter, the matrix $\boldsymbol{M}$ is defined as

$$\boldsymbol{M}(x) = \begin{pmatrix}\cos x & \sin x \\ \sin x & -\cos x\end{pmatrix}. \qquad 1.4.14.$$

Outside the crystal the beam will be a superposition of the eigenstates of free space propagation so the Hamiltonian that describes the transformation of a beam through a crystal of length l to a point z in the space beyond it can be written as

$$\boldsymbol{H}(\vec{P}, z) = \left(P^2\boldsymbol{I} + AP\boldsymbol{M}(\varphi_k)\right)U(l - z) + {}^1\!/_2\, n_2 P^2 \boldsymbol{I} U(z - l), \qquad 1.4.15.$$

where

$$U(n) = \begin{cases}0, & x < 0 \\ 1 & x \geq 0\end{cases} \qquad 1.4.16.$$

and the ${}^1\!/_2\, n_2 P^2$ factor represents the free space paraxial wave equation (cf substitution 1.4.5 and equation 1.4.8). The Hamiltonian equation is solved in the same way as in the elementary case mentioned above.

$$\vec{E}(\vec{r}, z) = \exp\left[ik\int_0^z \boldsymbol{H}(z`)\, dz`\right]\vec{E}(\vec{r}, 0) \qquad 1.4.17.$$

After substituting the definition of the Hamiltonian in equation 1.4.15 into 1.4.17 and performing the integral over $z`$, the right hand side of equation 1.4.17 becomes

$$\exp\left[ik\left(P^2\boldsymbol{I} + AP\boldsymbol{M}(\varphi_k)\right)l + {}^1\!/_2\, n_2 P^2 \boldsymbol{I}(z - l)\right]\vec{E}(\vec{r}, 0)\,, \qquad 1.4.18.$$

To evaluate this expression the matrix exponential can be written as a Taylor series, using $e^x = \sum_{n=0}^{\infty} \frac{x^n}{n!}$. The result, obtained in (Berry, 2004) is

$$\vec{E}(\vec{r}, Z) = \frac{k}{2\pi} \iint e^{ik\vec{P}\cdot\vec{r}} e^{-\frac{1}{2}ikP^2 Z} [\cos(kPR_0)\, \boldsymbol{I} - i\sin(kPR_0)\, \boldsymbol{M}(\varphi_P)] \vec{a}(\vec{P}) d\vec{P} \quad 1.4.19.$$

where the geometric ring radius associated with conical refraction is given by

$$R_0 = Al, \quad 1.4.20.$$

and the effective propagation distance is defined as:

$$Z = l + (z - l)n_2. \quad 1.4.21.$$

This effective propagation distance measures distance from the virtual image of the position on the z axis of $E(\vec{r}, 0)$. This is the position at which $E(\vec{r}, 0)$ would seem to occur to someone observing the beam beyond the crystal. $E(\vec{r}, 0)$ will refer to the electric field at the position of minimum beam waist in all calculations where we are dealing with Gaussian beams unless indicated otherwise. We will refer to the plane at which $Z = 0$ as the focal image plane (FIP), following Berry (Berry, 2004).

If we presume that the incident beam is circularly symmetric (i.e. $\vec{a}(\vec{P}) = \vec{a}(P)$)), we can rewrite this integral in polar co-ordinates $\{P, \varphi_P\}$ and, integrating over φ_P, we have

$$\vec{E}(\vec{r}, Z) = k \int_{\mathbf{0}}^{\infty} P e^{-\frac{1}{2}ikP^2 Z} [J_0(kPr)\cos(kPR_0)\, \boldsymbol{I} + J_1(kPr)\sin(kPR_0)\, \boldsymbol{M}(\varphi)] \vec{a}(P) dP, \quad 1.4.22.$$

where J_m is an m^{th} order Bessel function of the first kind, and we have used

$\int_0^{2\pi} d\theta e^{ikr\cos(\varphi-\theta)} = 2\pi J_0(kr)$ and $\int_0^{2\pi} d\theta e^{ikr\cos(\varphi-\theta)}\cos(\theta) = 2\pi J_1(kr)\cos(\varphi)$.

If we presume $\vec{a}(P)$ is uniformly polarized, so that $\vec{a}(P) = a(P)\hat{e}$, where $\hat{e} = \begin{pmatrix} e_x \\ e_y \end{pmatrix}$ is the incident polarization vector, then the expression for the conically diffracted field becomes

$$\vec{E}(\vec{r}, z) = (\mathrm{B}_0 \boldsymbol{I} + \mathrm{B}_1 \boldsymbol{M}(\varphi)) \begin{pmatrix} e_x \\ e_y \end{pmatrix}, \quad 1.4.23.$$

with

$$B_0(r,Z) = k\int_0^\infty Pe^{-\frac{1}{2}ikP^2Z}\cos(kPR_0)J_o(kPr)a(P)dP, \qquad 1.4.24.$$

$$B_1(r,Z) = k\int_0^\infty Pe^{-\frac{1}{2}ikP^2Z}\sin(kPR_1)J_1(kPr)a(P)dP. \qquad 1.4.25.$$

Equation 1.4.23 and the integral expressions 1.4.24 and 1.4.25 fully describe a general paraxial beam after conical diffraction.

The intensity

$$I(\vec{r},Z) = \vec{E}\cdot\overrightarrow{E^*} = B_0B_0^* + B_1B_1^* + \left(e_xe_x^* - e_ye_y^*\right)(B_0B_1^* + B_1B_0^*)\cos\varphi + e_ye_x^*\sin\varphi\,(B_1B_0^* + B_0B_1^*) + e_xe_y^*\sin\varphi\,(B_1B_0^* + B_0B_1^*). \qquad 1.4.26.$$

For circular incident polarization equation 1.4.26 reduces to

$$I(\vec{r},Z) = B_0B_0^* + B_1B_1^*, \qquad 1.4.27.$$

and for linear incident polarization, say horizontal {1, 0}, equation 1.4.26 reduces to

$$I(\vec{r},Z) = \vec{E}\cdot\overrightarrow{E^*} = B_0B_0^* + B_1B_1^* + (B_0B_1^* + B_1B_0^*)\cos\varphi. \qquad 1.4.28.$$

Thus a circularly symmetric paraxial beam is converted into a circularly symmetric beam by conical diffraction if it is circularly polarized and into a non-circularly symmetric beam if it is linearly or elliptically polarized (this is to be expected since a circularly polarized beam can be decomposed into any pair of orthogonal linear polarizations with equal amplitudes). In the next chapter we will explore the consequences of the paraxial theory developed here for the case of a conically diffracted Gaussian beam.

Chapter 2. Conical diffraction of a Gaussian beam

In this chapter we examine some of the predictions of paraxial conical diffraction theory and compare them with experiment for the case of a Gaussian incident beam. In section 2.1 the predictions of paraxial theory are outlined for a range of incident beam parameters and for various optical arrangements. The dependence of the conically diffracted Gaussian beam on incident beam waist and polarization is shown to facilitate the transformation of Gaussian beams into Lagurerre-Gaussian, Hermite-Gaussian and other useful beams. These transformations are demonstrated experimentally in Section 2.2 and the predictions of paraxial theory regarding the radial intensity distributions of the conically diffracted beam are also experimentally validated. In Section 2.3, the conversion of a Gaussian beam into a non-diverging zeroth order and first order Bessel beam via conical diffraction is demonstrated.

2.1. Shaping the conically diffracted Gaussian

A Gaussian beam with transverse electric field profile e^{-r^2/ω_0^2} at the position of its minimum beam radius, and Fourier transform $\sqrt{\pi\omega_0^2}e^{-\frac{1}{4}\omega_0^2k^2P^2}$, is transformed by conical diffraction into the superposition of orthogonally polarized beams introduced in the last section (equations 1.4.23 – 1.4.25) with

$$\mathrm{B}_0(r,z) = \sqrt{\pi k^2\omega_0{}^2}\int_0^\infty Pe^{-\frac{1}{2}ikP^2Z}\cos(kPR_0)J_o(kPr)e^{-\frac{1}{4}\omega_0^2k^2P^2}dP, \qquad 2.1.1$$

$$\mathrm{B}_1(r,z) = \sqrt{\pi k^2\omega_0{}^2}\int_0^\infty Pe^{-\frac{1}{2}ikP^2Z}\sin(kPR_0)J_1(kPr)e^{-\frac{1}{4}\omega_0^2k^2P^2}dP. \qquad 2.1.2$$

Examining equations 2.1.1 and 2.1.2, it is apparent that the only parameters that can affect the spatial shape of the conically diffracted beam are the waist of the incident Gaussian and the geometrical radius, R_0, associated with the biaxial crystal. This fact has been emphasised by

Berry, who has introduced the parameter $\rho_0 = {}^{R_0}/_{\omega_0}$ (Berry, 2004). Since, from an experimental point of view, it is easier to vary the waist than the geometric ring radius associated with the crystal, we will be considering the dependence of the conically diffracted beam on the waist ω_0 of the incident Gaussian beam and keeping R_0 constant in the following discussion.

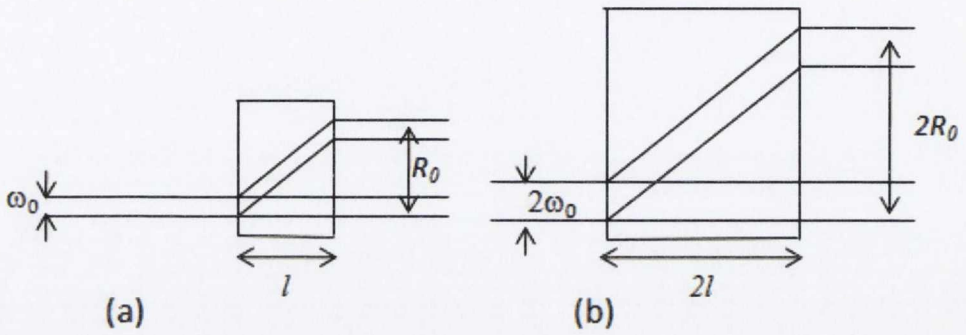

Figure 2.1.1: An illustration of the use of the parameter ρ_0 in characterising the shape of the conically diffracted Gaussian beam. The value of ρ_0 in part (a) is the same as in part (b). The only difference between the beams emerging from the crystals in each case is the scale.

Increasing the beam waist from a value that is small compared to R_0 gradually increases the thickness of the rings until we reach a point where the two rings merge into a single ring. This occurs when ω_0 is about equal to R_0. If we increase the waist still further so that $\omega_0 \approx 2R_0$, we no longer even have a single ring and the Gaussian is transformed into a beam with a top hat shaped profile. To achieve this in practice a thin crystal should be used. Calculated focal image plane profiles are shown in Figure 2.1.2 for R_0 = 0.53 mm and for four values of ω_0.

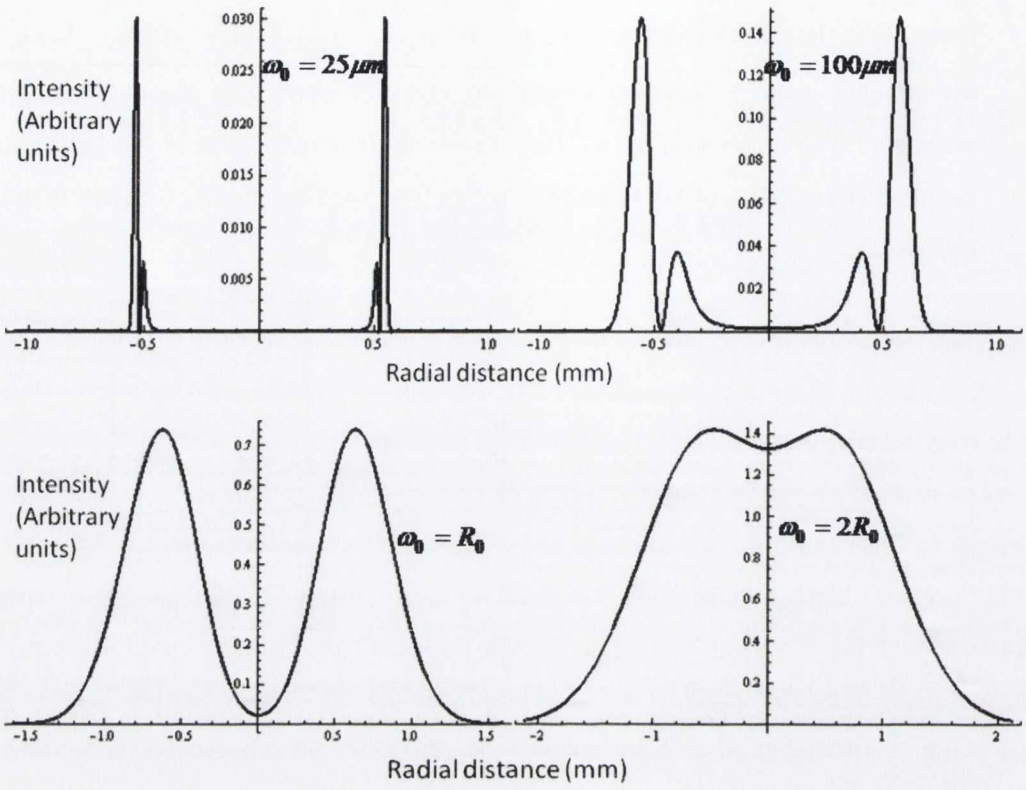

Figure 2.1.2: Linear intensity plots of the focal image plane profile, for R_0 = 0.53 mm and several values of ω_0. There is a uniform broadening of the rings as ω_0 is increased from zero to R_0 after which the two sides of the ring begin to merge.

Referring to Figure 2.1.2, it is seen that the double ring profile is at its sharpest when the waist is small compared to the geometric ring radius.

Regardless of the value of the incident waist, the conically diffracted Gaussian remains a separable superposition of a beam with uniform phase as a function of azimuthal angle that is polarized in the same manner as the incident beam, and a beam with a first order phase vortex that is polarized orthogonally to the incident beam. The intensity profiles of the B_0 and B_1 components are plotted for a range of incident beam waist values in Figure 2.1.3. The corresponding electric field profiles are shown in Figure 2.1.4.

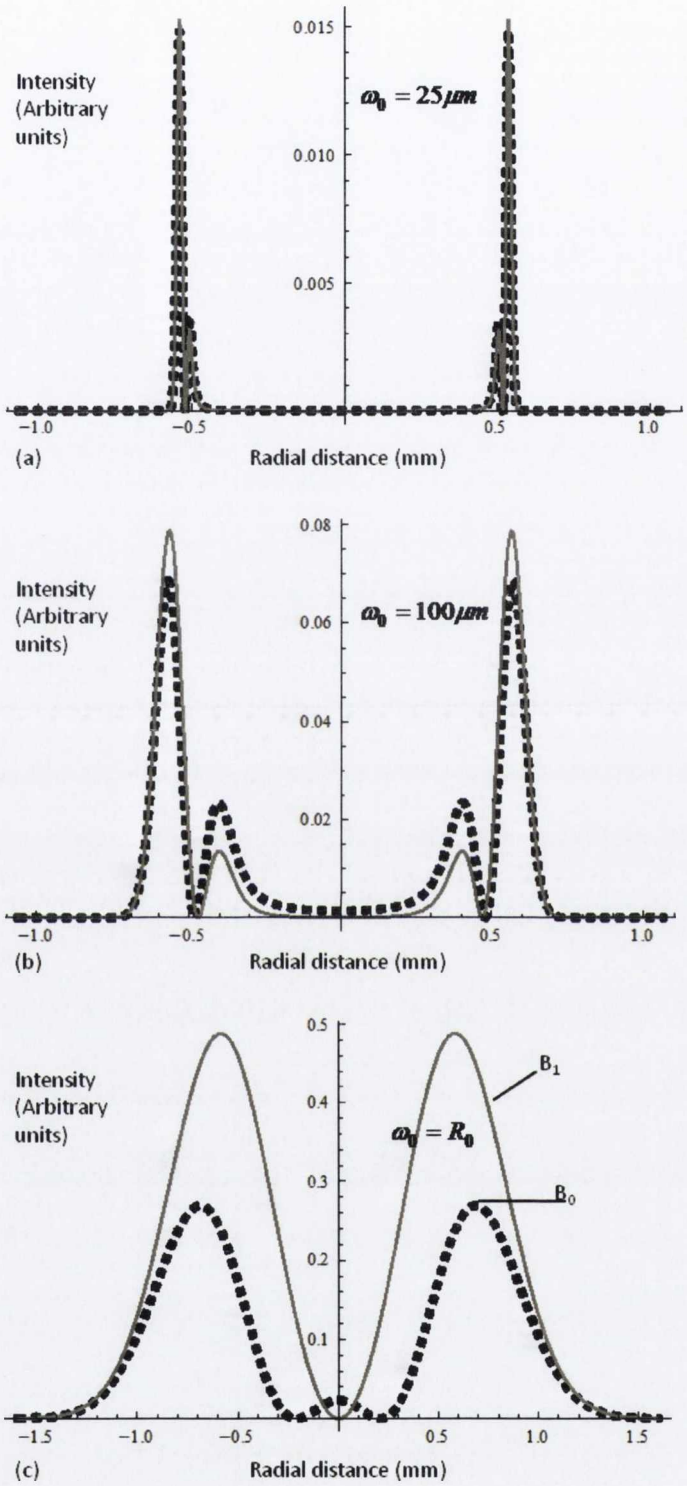

Figure 2.1.3: Linear intensity plots of the focal image plane profile of the B_0 (dashed line) and B_1 (continuous line) components for several values of ω_0. The values of the incident waist are (a) 25 μm, (b) 100 μm and (c) 0.53 mm = R_0. The dashed line represents B_0 and the continuous grey line represents B_1.

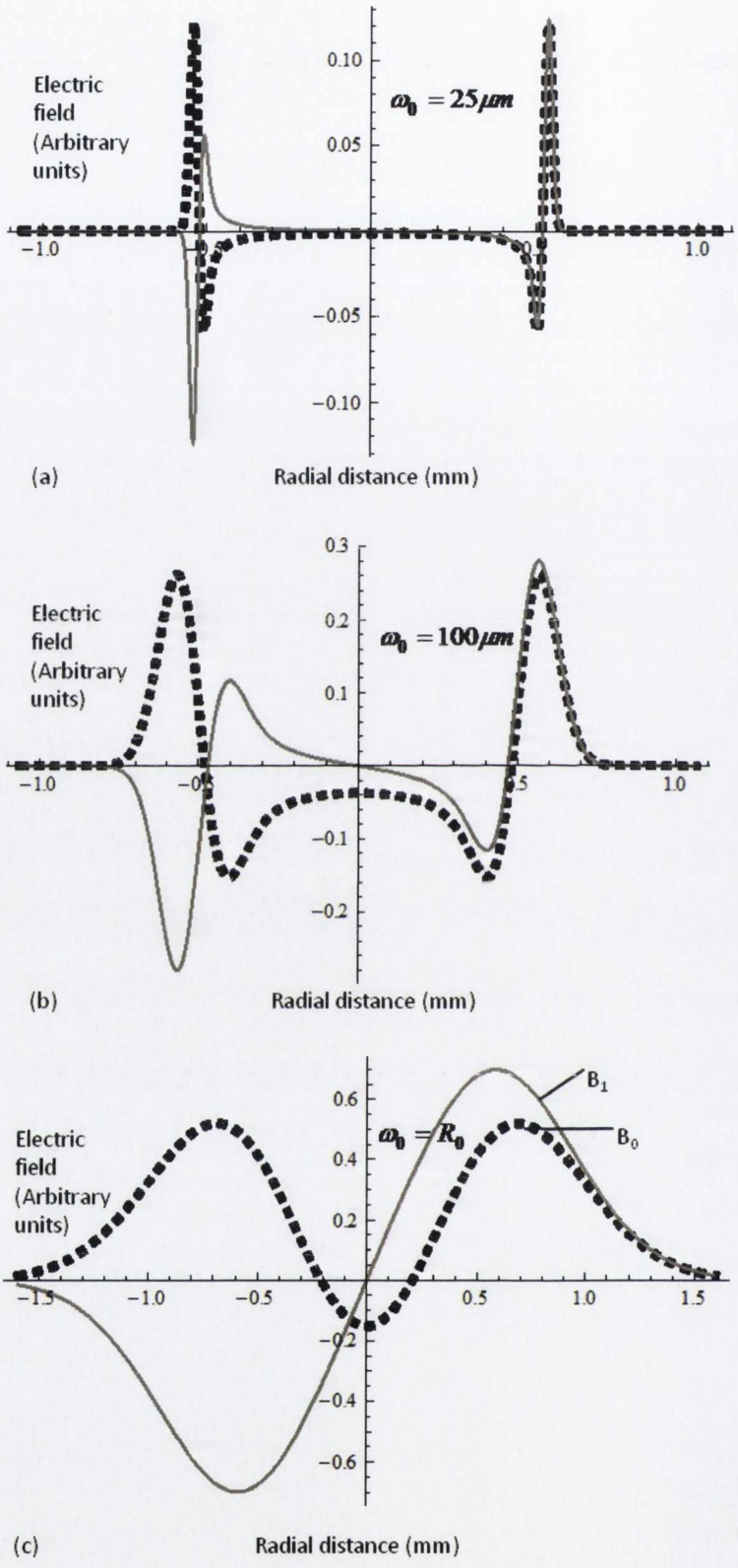

Figure 2.1.4: Linear electric field plots of the focal image plane profile of the B_0 (continuous line) and B_1 (dashed line) components corresponding to the intensity plots in Figure 2.1.3.

It can be seen that the intensity profiles of the B_0 and B_1 components are almost identical for values of the incident waist that are small compared to R_0. This fact may be used to explain the interesting polarization profile associated with conical refraction. As is well known, at any point on the focal image plane the polarization is linear but it rotates from tangential at the point on the ring corresponding to the straight-through position, to radial at the diametrically opposed point. In fact for all diametrically opposed positions the polarizations are orthogonal. This feature can be readily understood by considering the superposition of the B_0 and B_1 field components in the focal image plane. In Figure 2.1.5 we present a schematic representation of the addition of these fields. The first two rows in that figure show the orientation of the field vector at four successive times differing by quarter of an optical cycle for the B_0 (top) and B_1 (middle) fields. The bottom row shows the coherent addition of these two fields. At any time during the optical cycle the electric field of the B_0 component has the same direction at any point on the ring, while for the B_1 component the field rotates by 2π on moving round the ring. Adding the two sets of polarization vectors leads to the familiar half turn of linear polarization together with a π phase shift on making a full circuit of the optic axis.

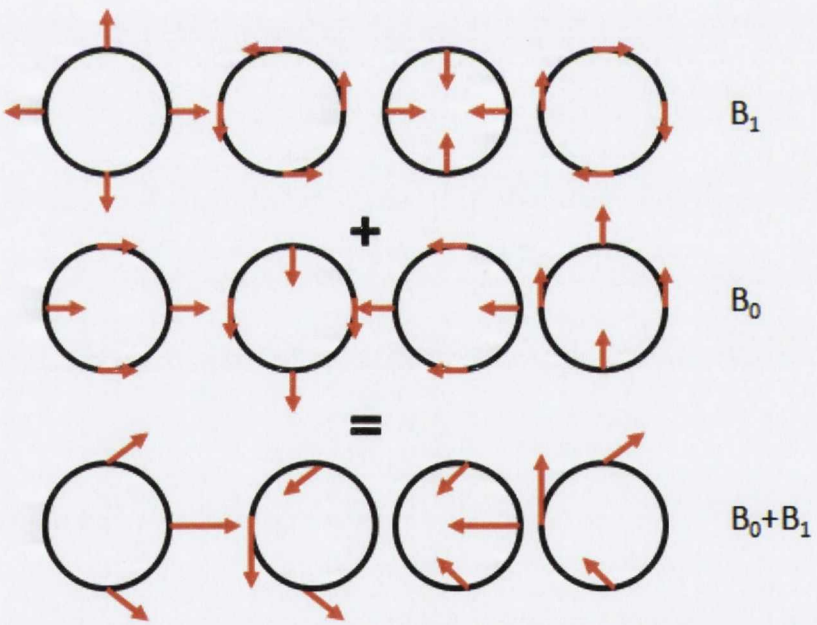

Figure 2.1.5: The different phase properties of the fields described by B_0 and B_1. The figure shows, over one optical cycle, how the field vectors of the B_1 component (top) combine with the field vectors of the B_0 field (middle) to give the half turn of polarization associated with conical refraction (bottom).

It is worth noting that for values of ω_0 close to R_0 the B_1 beam resembles a Laguerre Gaussian LG_{01} beam. In Figure 2.1.6 we compare the B_1 electric field profile with that of an LG_{01} beam. It turns out that there is quite close correspondence of the two beams when we set the waist of

the LG_{01} beam to be ~ 1.5 times the waist of the Gaussian that was transformed into the B_1 beam.

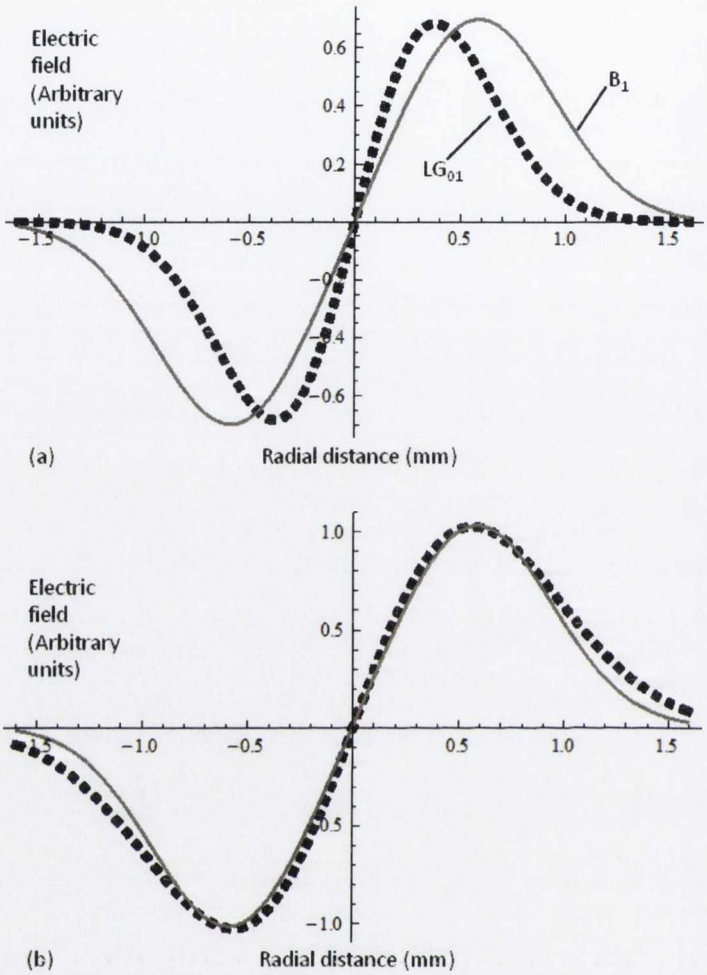

Figure 2.1.6: (a) A comparison of the B_1 electric field for the case of $\omega_0 = R_0$=0.53 mm, with the electric field profile of a Laguerre Gaussian beam with Gaussian waist of R_0. In part (b) the waist of the Laguerre Gaussian was set to be 1.5 R_0 which leads to closer correspondence of the two beams.

Another feature of how the conically diffracted Gaussian depends on incident beam waist is the effect of the incident beam waist on the distribution of optical power between the B_0 and B_1 components (see Figure 2.1.3). This ratio approaches equality in the case of a small incident waist (relative to the geometrical ring radius. i.e. large ρ_0) and is plotted in Figure 2.1.7 as a function of the waist of the incident Gaussian ω_0.

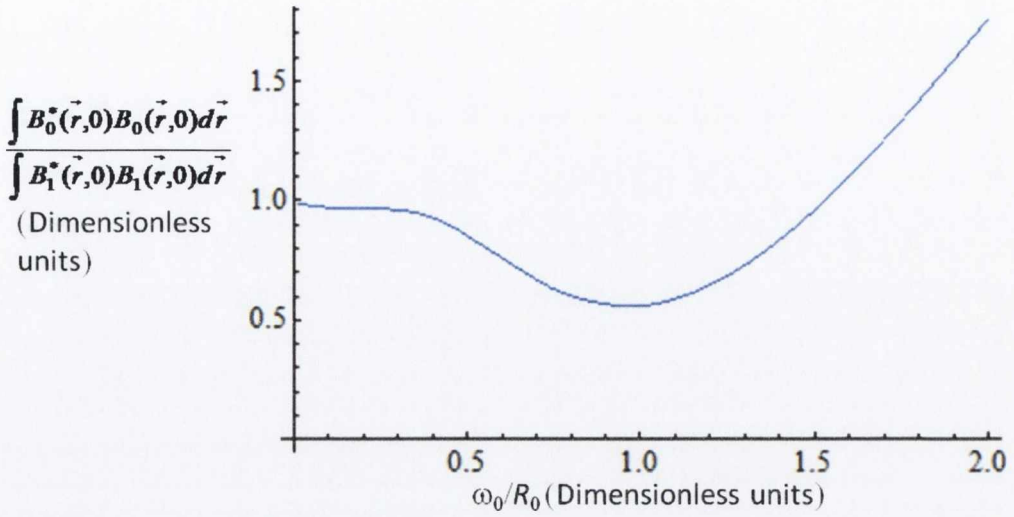

Figure 2.1.7: The ratio of optical power in B_0 to B_1 as the incident waist is varied. As the ratio ω_0/R_0 approaches zero, the power ratio approaches unity. This is the case of "high quality" conical diffraction that most closely approximates Geometrical optics in the focal image plane.

The ratio of the power ratio between these components has the following interesting consequence. Since the vortex carrying beam B_1 has $1\hbar$ OAM per photon while B_0 has zero OAM per photon, varying the waist of a circularly polarized Gaussian incident on a biaxial will vary the fractional OAM per photon in the conically diffracted beam (An account of how we might observe the OAM of the B_1 beam is given in Appendix A). The dependence of OAM per photon on the ratio of incident Gaussian waist to geometrical ring radius is derived in (Berry, Jeffrey, & Mansuripur, 2005). It is also possible to tune the OAM of the conically diffracted beam by varying the incident polarization between circular and linear since there is no optical vortex in the conically diffracted beam for the case of a linearly polarized incident Gaussian. This latter process has been experimentally demonstrated in (O'Dwyer, Phelan, Rakovich, Eastham, Lunney, & Donegan, 2010).

The waist of the incident beam also determines the diffraction of the FIP profile. In general the ring shaped beam will diverge as it propagates away from the FIP with the waves that are focused to form the ring profile both diverging away from and converging towards the centre of the ring, see Figure (2.1.8). A tightly focused incident beam will be conically diffracted into a highly divergent sharp double ring profile. As the incident beam waist is increased the ring profile becomes less sharp and less divergent. The evolution of the conically diffracted Gaussian is depicted in Figure 2.1.8 for three different values of incident beam waist. In the focal image plane the separation of the rings is $\sim 1.6\omega_0$. Beyond the Rayleigh range, the angle of divergence between the rings is $\sim 4/k_0\omega_0$, the same as the divergence angle of the Gaussian outside the Rayleigh range.

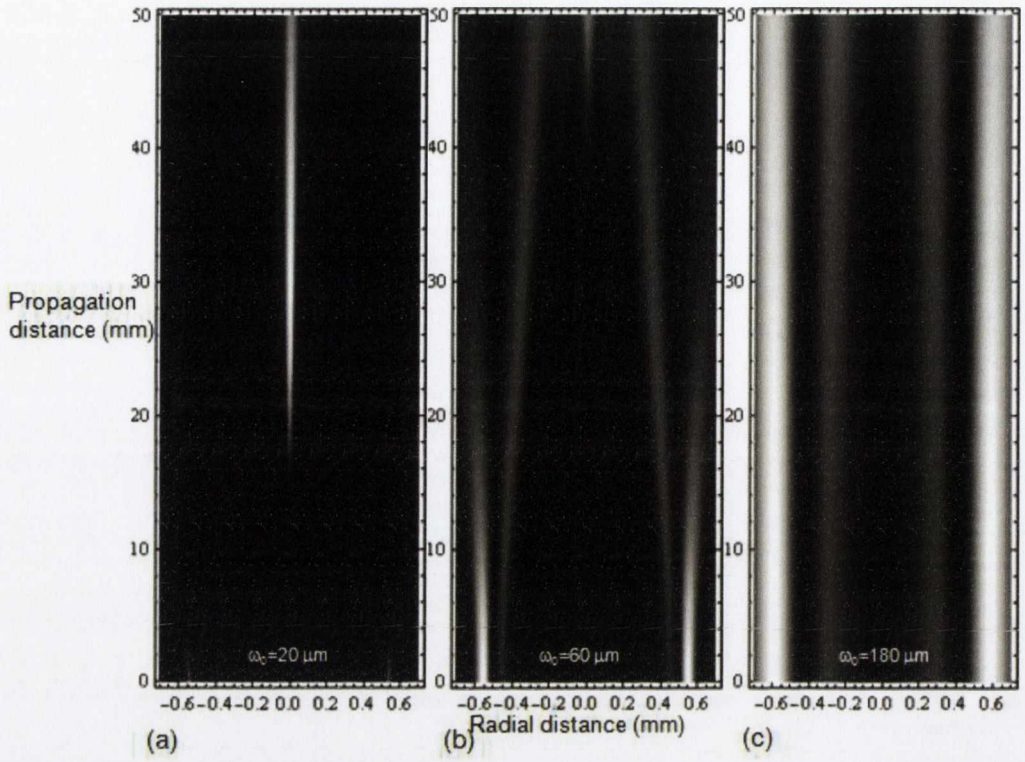

Figure 2.1.8: The intensity in the {*r*, *z*} plane of the CDG as it propagates from the FIP (0) to a distance of 50 mm from the FIP. The waists used to generate the plots were (a) 20 μm, (b) 60 μm and (c) 180 μm. The effect of the incident waist on the diffraction of the FIP profile can be seen. In each plot we have R_0 = 0.53 mm

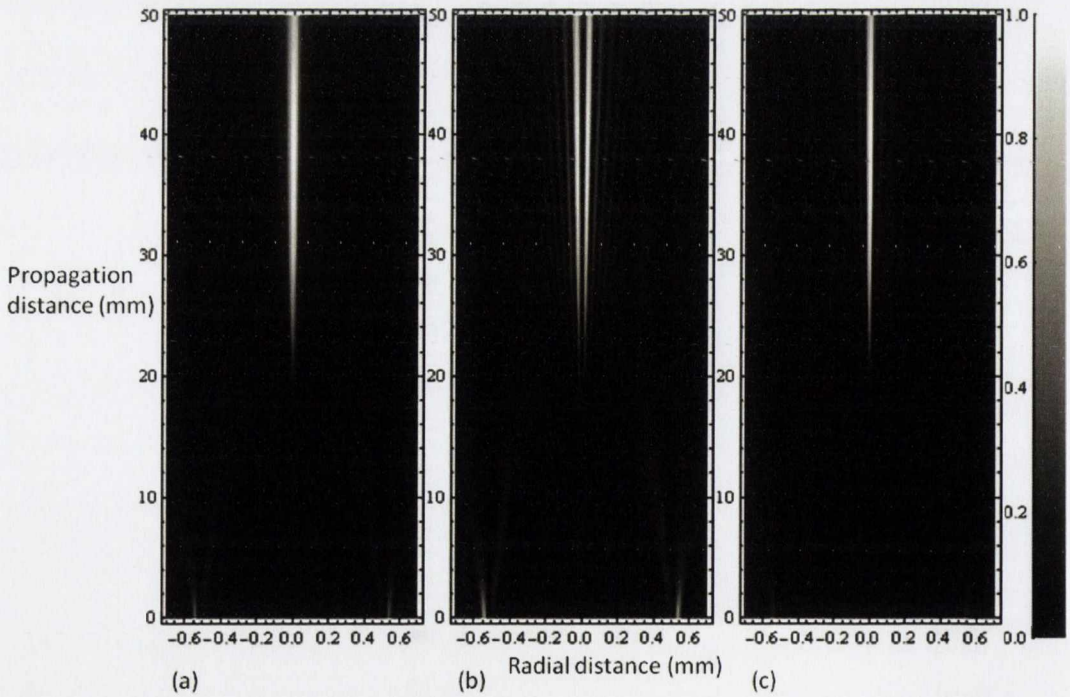

Figure 2.1.9: The intensity profile in the {r, z} plane over a distance of 50 mm. (a) The full conically diffracted Gaussian. (b) The B_1 beam. (c) The B_0 beam. The waist used for this calculation was 25 μm and the R_0 was 0.53 mm.

The far field profiles of each of the two orthogonally polarized components of the conically diffracted Gaussian are more interesting than the far field profile of the composite beam. It is well known that the Fourier transform of an azimuthally uniform thin ring is a zeroth order Bessel function and the Fourier transform of a thin ring with an azimuthal phase factor will involve a Bessel function, the order of which depends on the phase factor. It is no surprise then that in the case of $\omega_0 \ll R_0$ (i.e. a thin double ring near field profile) the B_0 beam diffracts into a far field profile that is very well approximated by a zeroth order Bessel function and the B_1 field diffracts into a far field profile that is equally well approximated by a first order Bessel function (Berry, 2004). The evolution of each of the component beams as well as the composite beam is plotted in Figure 2.1.9 for the case of an incident beam waist of 25 μm and crystal with geometric ring radius of 0.53 mm. The main features of the far field profiles of the B_0 and B_1 components are evident from Figure 2.1.9 but plots of the transverse intensity profiles of both beams and the composite beam are given in Figure 2.1.10.

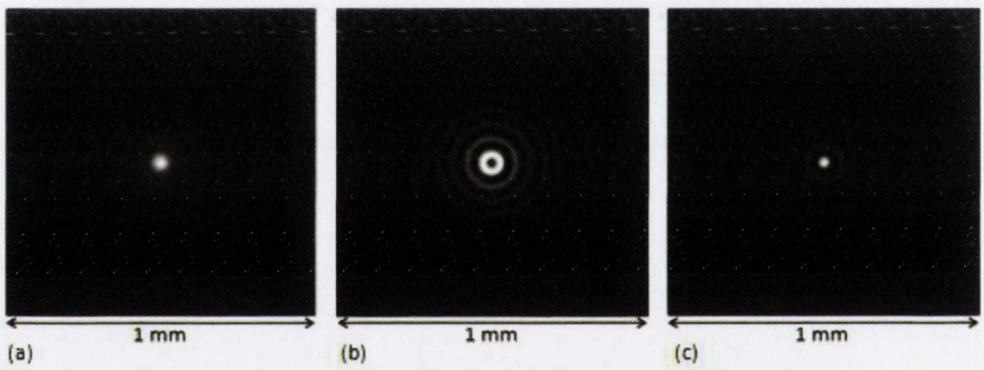

Figure 2.1.10: Far field intensity profiles of (a) the full conically diffracted beam; (b) B_1 and (c) B_0. In this simulation the incident waist $\omega_0 = 25\ \mu m$ and geometric ring radius $R_0 = 0.53\ mm$. The beam had propagated 50 mm from the FIP.

Two other types of commonly sought after laboratory beams that can be generated with a very simple optical arrangement involving conical diffraction of a Gaussian are the Hermite Gaussian and Hermite Bessel beams. The only difference in the optical setup used to generate these beams from the setup used to generate the beams previously described is that the incident beam is linearly, rather than circularly, polarized. It is easy to see that placing a biaxial crystal between crossed polarizers will lead to a beam whose ring profile is modulated with two intensity zeros on opposite sides of its centre. One of the intensity zeros is due to the fact that we had linearly polarized incident light and thus conical diffraction produced a crescent rather than a ring. The second intensity zero results from the action of the second linear polarizer. If, for definiteness, we take the light incident on the crystal to be horizontally polarized with polarization vector {1, 0} then a linear polarizer placed after the crystal that transmits only

vertically polarized light will transmit light with electric field proportional to $B_1 \sin\varphi$. In general, a beam polarized at an angle α to the positive x axis that is conically diffracted and then propagated through a polarizer that transmits light polarized at α+90° is transformed into

$$\vec{E}(r,\varphi,Z) = \mathrm{B}_1(r,Z)\sin(2\alpha-\varphi)\begin{pmatrix}\sin\alpha\\-\cos\alpha\end{pmatrix} \qquad 2.1.3$$

In figure 2.1.11 the far field intensity distribution due to the electric field in equation 2.1.3 is plotted for two values of α and two values of the incident waist. The beam has a profile resembling that of a Hermite Gaussian with $\omega_0 \approx R_0$ that of a Hermite-Bessel beam for $\omega_0 << R_0$ and.

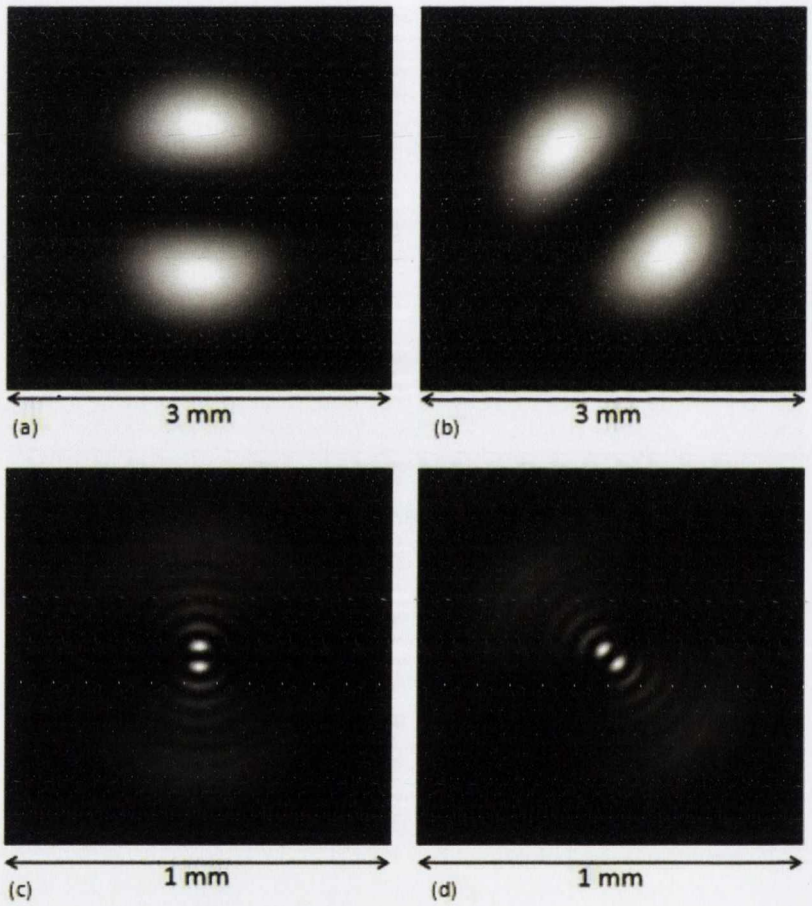

Figure 2.1.11: Intensity profiles generated from equation 2.1.3. (a): $\omega_0 = R_0$=0.53 mm, $\alpha = 0°$ (b) $\omega_0 = R_0$, $\alpha = 22.5°$ (c) ω_0 = 40 μm, $\alpha = 0°$ (d) ω_0 = 40 μm, $\alpha = 22.5°$. Each simulation was performed at 50 mm from the FIP. Note that the diffraction over 50 mm of the beams with $\omega=R_0$ is negligible.

2.2. Theory versus experiment

The first optical arrangement used to examine the various beams which can be produced by conical refraction is shown in Figure 2.2.1. The sharpest rings are obtained when a second lens is used to image the plane at Z=0 since this allows us to form the FIP inside the crystal. The Gaussian beam output of a 10 mW 632 nm He-Ne laser was left–circularly polarized using a linear polarizer and a $\lambda/4$ plate. The beam was focused with a 10x microscope objective to form a beam waist radius $\omega_0 = 14$ μm at the $1/e^2$ point. The biaxial crystal used was a 3 cm thick slab of $KGd(WO_4)_2$ obtained from *CROptics* [www.croptics.eu] with principal refractive indices n_1=2.013, n_2=2.045, n_3=2.086, measured by Pujol et al (Pujol, et al., 1999) at 632 nm. The crystal was cut with one of the optic axes perpendicular to the slab faces. In the first setup the incident beam waist was positioned near the input face of the crystal. The output beam was imaged at 1:1 magnification using a 10 cm focal length lens on to a Firewire CCD camera (Thorlabs DC310). Different planes were recorded by moving the imaging lens and CCD camera together.

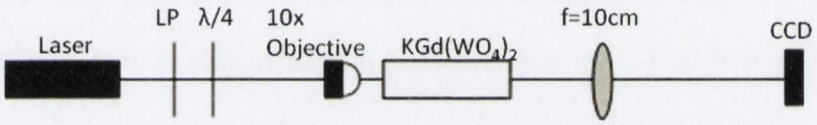

Figure 2.2.1: Circularly polarized light is focused into the crystal with a x10 objective to achieve a narrow waist (10μm). The focal image plane, which for this setup occurs somewhere near the crystals entrance face (due to the short focal length of the objective), is imaged onto the CCD with a 10cm focal length lens.

The focal image plane intensity profile is shown in Figure 2.2.2. Since the beam waist is near the input face of a 3 cm thick crystal this plane is located at 1.53 cm inside that face. The radius of the dark ring in the focal image plane is found to be 0.53 mm, in close agreement with the expected value of R_0 for A = 0.0177 rad. The separation of the rings is 19 μm, which is close to the expected value of 16 μm.

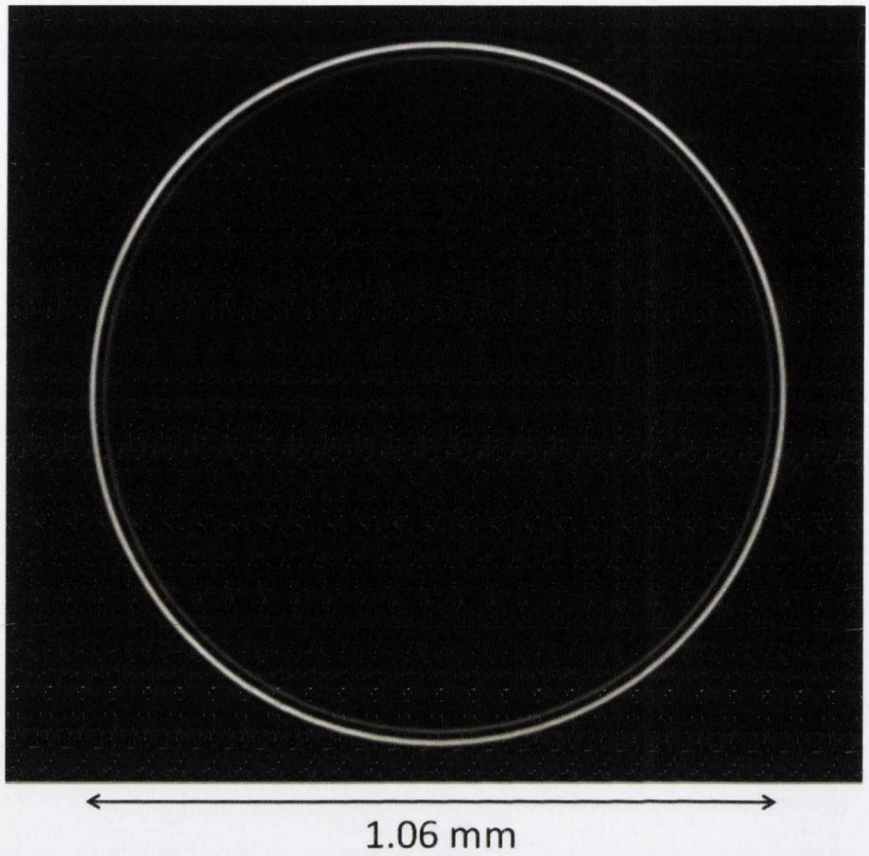

Figure 2.2.2: CCD image of the focal image plane taken using the experimental arrangement shown in Figure 2.2.1.

Conical diffraction can also be realized using the optical arrangement shown in Figure 2.2.3. Here a longer focal length lens is used to form a real focal image plane beyond the crystal. The beam waist of the focused laser beam was 25 μm. The radius of the dark ring in the transverse plane, which is determined by the length of the crystal, will be the same as before, but the width of the rings, which is dependent on the beam waist at focus, is now larger than before. Figure 2.2.4 shows a comparison of the calculated and measured radial intensity distributions in the focal image plane. There is good agreement, showing that the paraxial theory provides a good description of the phenomenon.

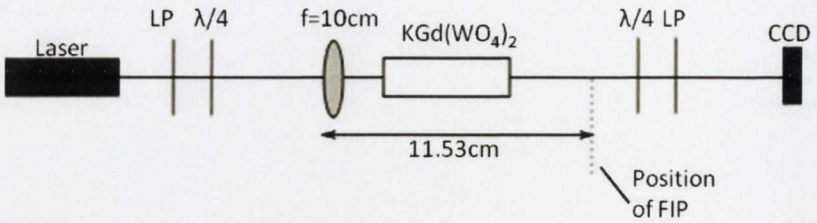

Figure 2.2.3: An alternative optical arrangement used to analyze conical diffraction. In this arrangement the FIP is formed beyond the crystal so an imaging lens is not required

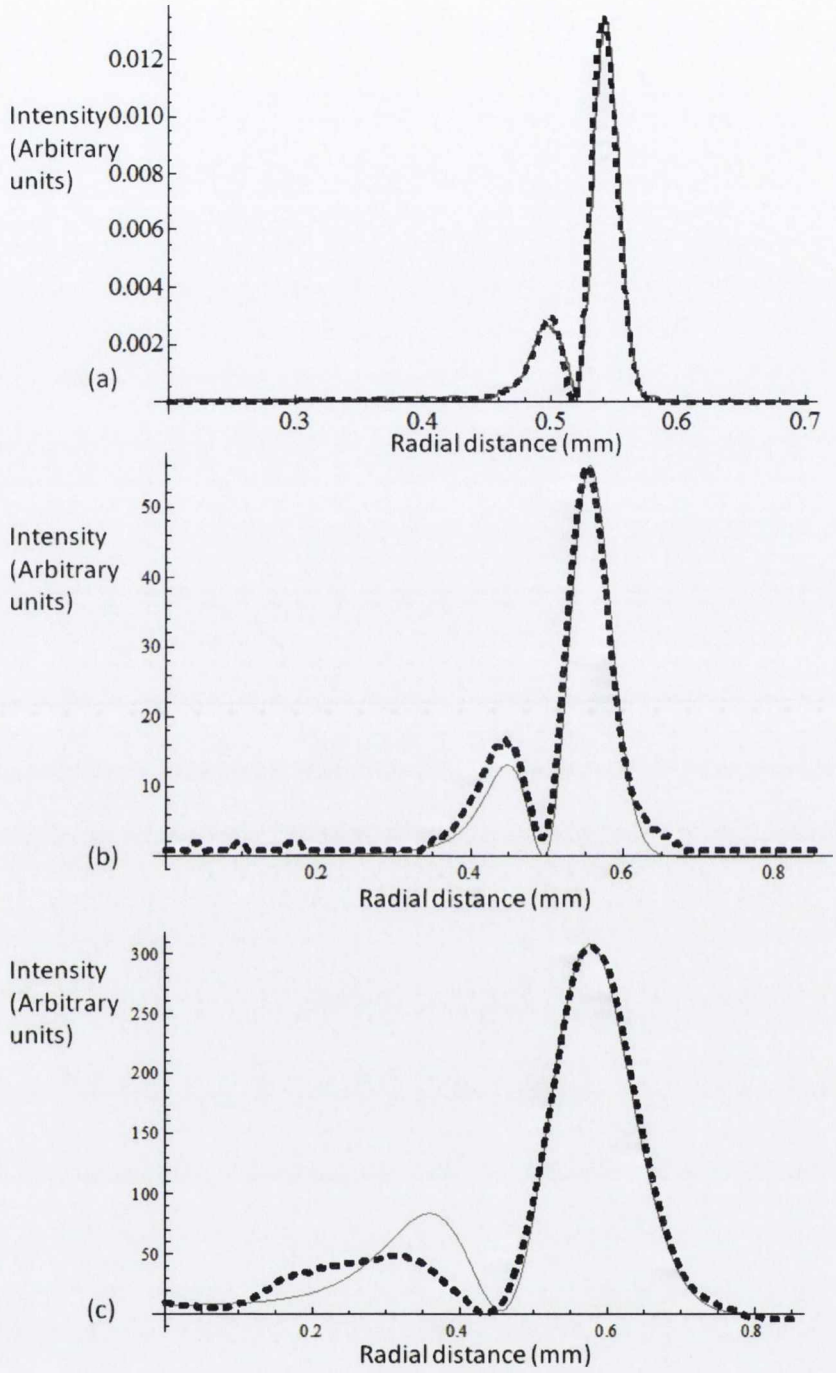

Figure 2.2.4: A comparison of experiment (dashed line) with theory in the focal image plane. The waists of the incident Gaussians were: (a) 25 μm, (b) 66 μm and (c) 132 μm. The agreement with theory is best for the smallest waist.

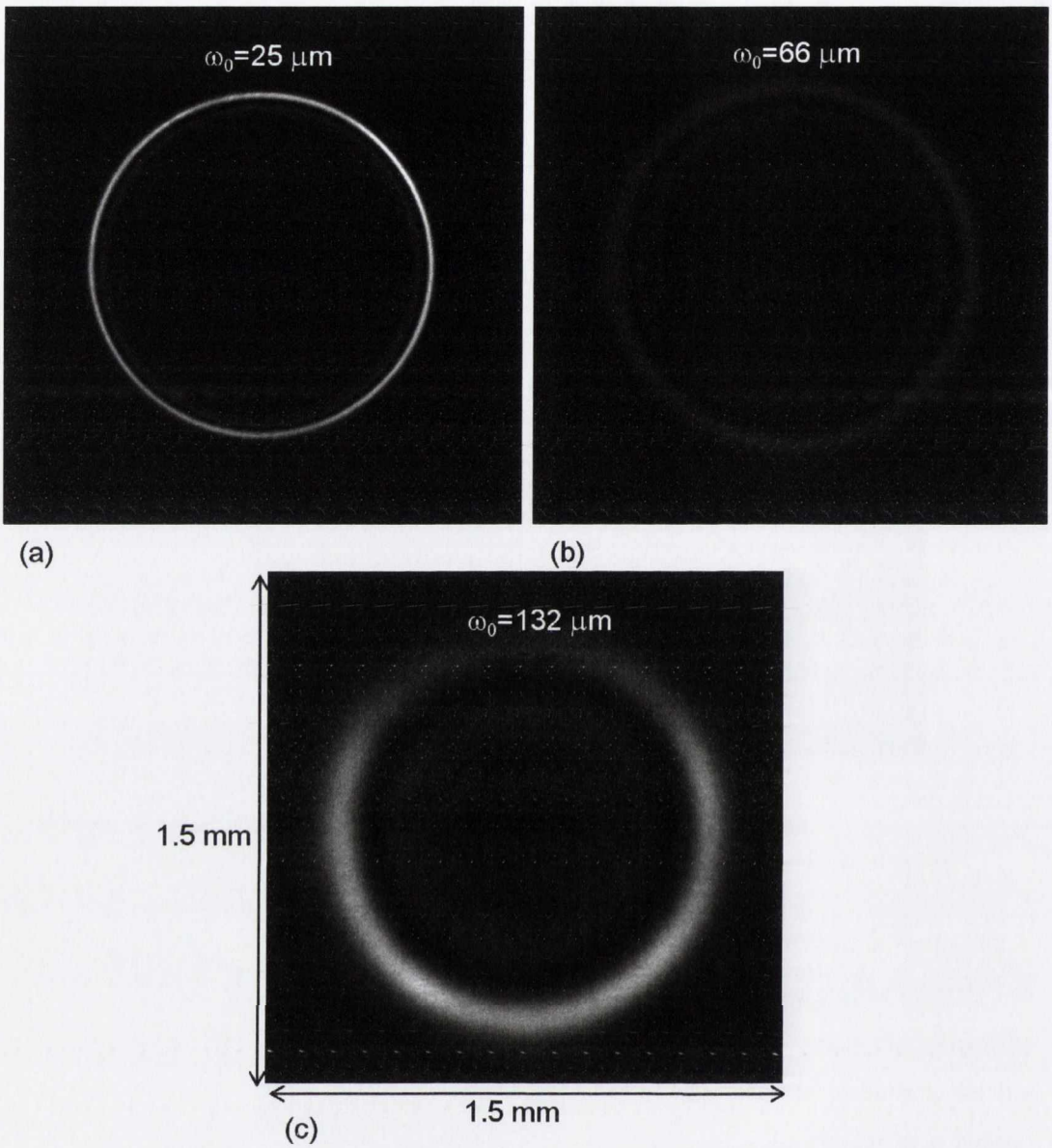

Figure 2.2.5: Parts (a), (b), and (c) show CCD images of the focal image plane profiles compared with experiment in parts (a), (b) and (c) of Figure 2.2.4.

Figures 2.2.6(a) and (b) show the far-field intensity distributions of the B_0 and B_1 beams recorded with the CCD camera placed at 10.75 cm (Z=22) from the focal image plane. The measured radial intensity distributions are compared with theory in Figure 2.2.7 (a) and (b), where the agreement of the experiment is seen to be very close. These profiles were obtained using the method outlined in Figure 2.2.3 with the incident beam having a waist of 25 μm.

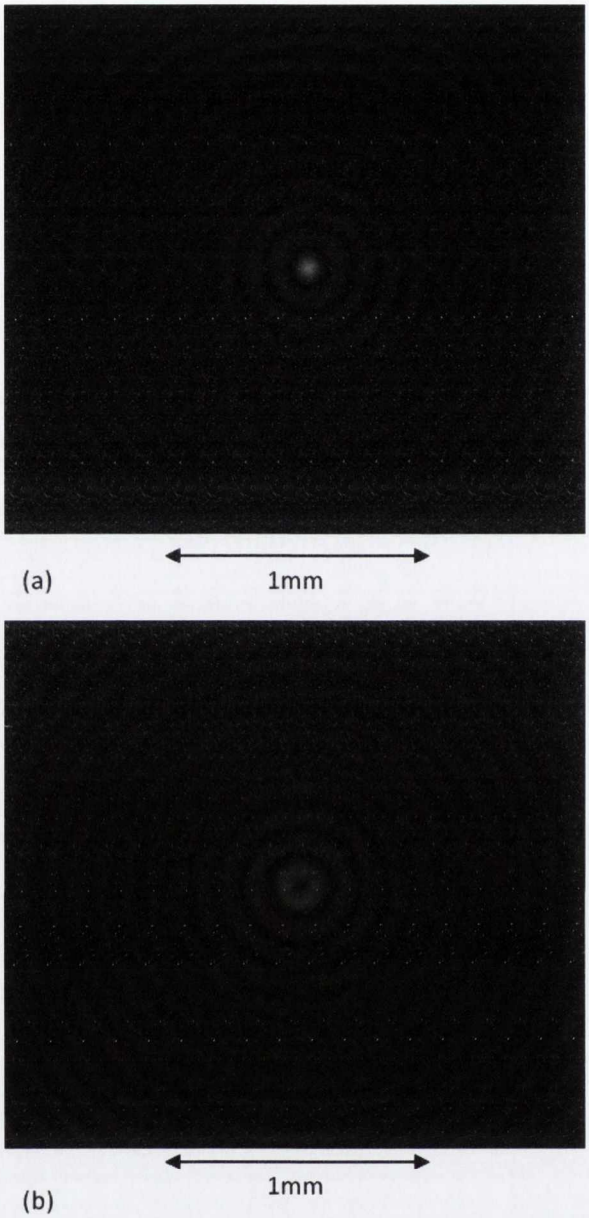

Figure 2.2.6: CCD pictures of the far field intensity distributions of the diverging Bessel beams; B_0 in (a); B_1 in (b). These images were taken with the experimental arrangement shown in figure 2.2.3.

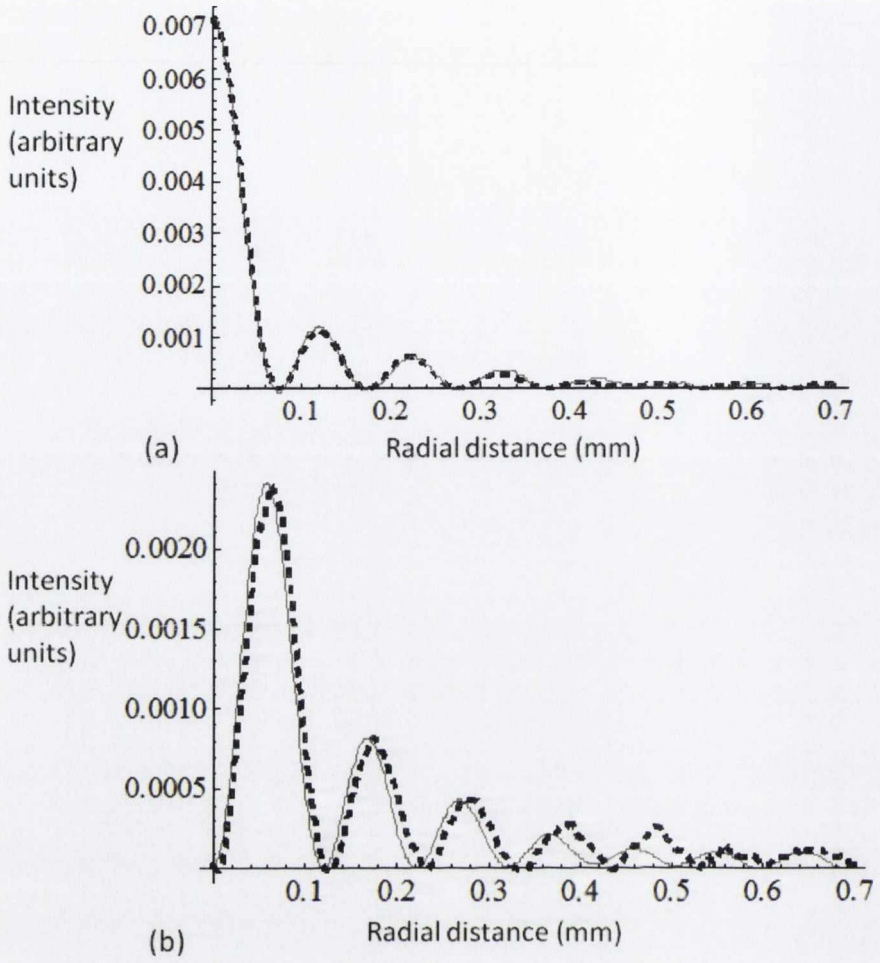

Figure 2.2.7: (a) A comparison of the radial intensity distribution of the B_0 beam at 10.75 cm from FIP with theory (continuous line); (b) same data for B_1. Both sets of experimental data were taken from the CCD images in Figure 2.2.6.

The transformation of a Gaussian with a waist comparable to the geometric ring radius of 0.53 mm was carried out using a setup similar to that in Figure 2.2.3 but with the focusing lens removed. The intention was to generate an LG type beam by selecting the B_1 component after propagation through the crystal. Figure 2.2.8 shows a comparison of the linear intensity profile of this beam with theory. The comparison is reasonably accurate with the deviations from theory probably due to the finite size of the entrance face of the crystal (4 mm x 3 mm). A CCD image of this beam is shown in Figure 2.2.9. The waist of the incident Gaussian was 0.7 mm or ~ 1.3 R_0.

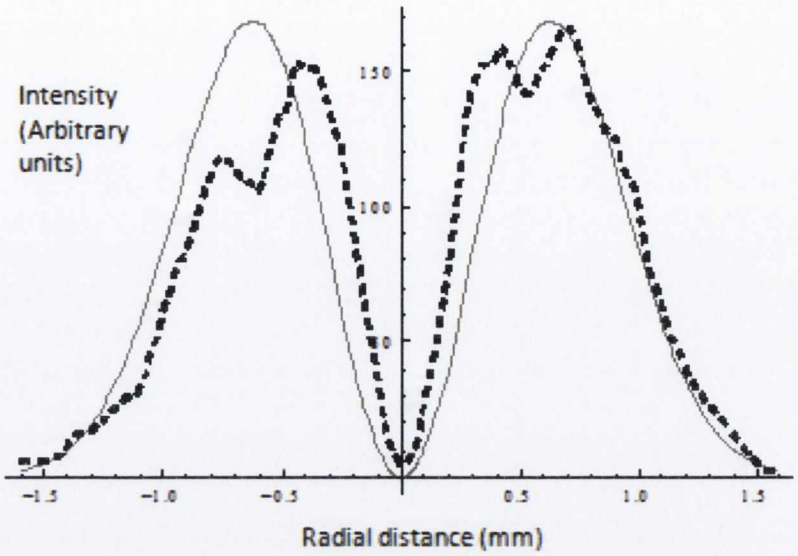

Figure 2.2.8: The measured B_1 profile (dashed) versus theory for a large incident waist. The waist of the incident Gaussian was measured to be 1.3 R_0.

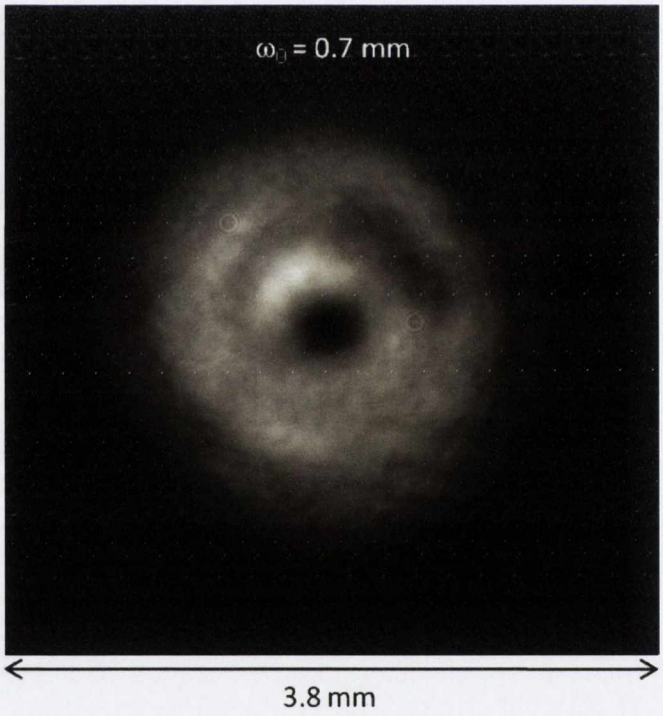

Figure 2.2.9: A CCD image of the B_1 beam that was generated by conical diffraction of a Gaussian with a waist of 1.3 R_0.

Finally the Hermite- Bessel like beams mentioned in the last section and described by equation 2.1.3 were generated using the experimental setup in Figure 2.2.10. The profiles display the expected $\sin\varphi$ modulation of the B_1 profile.

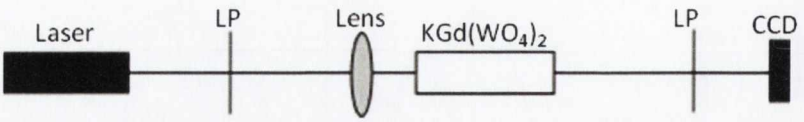

Figure 2.2.10: The experimental setup used to generate Hermite Bessel like beams via conical diffraction.

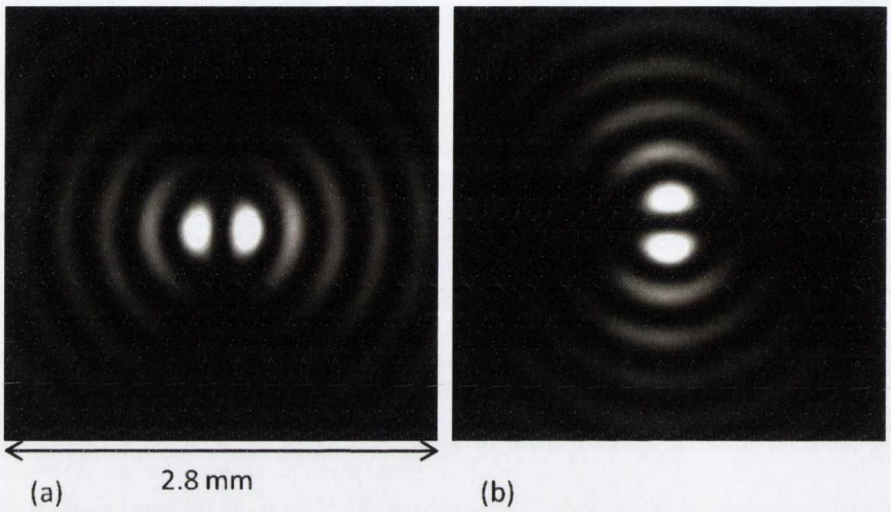

Figure 2.2.11: Beams generated by propagating a Gaussian through a crystal sandwiched between crossed polarizers. The incident polarization used to generate the beam in part (a) the left is vertical and the polarization of the beam itself is, according to equation 2.1.3, horizontal. The orientations of the polarizers on both sides of the crystal were rotated by 90° for part (b).

2.3. Formation of non-diverging beam

Bessel beams are a class of beams with a number of remarkable properties (Durnin, 1987). The defining feature of an ideal Bessel beam is that all of its wave vectors lie on a cone. If we write the wave vector of the Bessel beam as $\vec{k} = \{k_x, k_y, k_z\}$ with magnitude, $k_0 = \sqrt{k_x^2 + k_y^2 + k_z^2}$, then for each wave on the cone the magnitude of the radial component of its wave-vector, $k_r = \sqrt{k_x^2 + k_y^2}$, has the same value. The cone angle is given by $\theta = \tan^{-1}\left({}^{k_r}/_{k_z}\right)$ (see Figure 2.3.1). The simplest beam with this property has electric field amplitude proportional to:

$$J_0(rk_r)e^{ik_z z}. \qquad 2.3.1$$

The intensity profile associated with this beam has no z dependence and will consist of concentric rings of light with periodicity defined by the Bessel function. This is why beams of this form are referred to as non-diverging or non-diffracting. Another way to explain why beams composed of wave vectors on a cone do not appear to diffract is to note that as the

beam propagates a distance z each plane wave will undergo the same phase difference $k_z z$ since is the same for all of the plane waves. It follows from equation 2.3.1 that the full width at half maximum of the central spot is approximately equal to $1/k_r$.

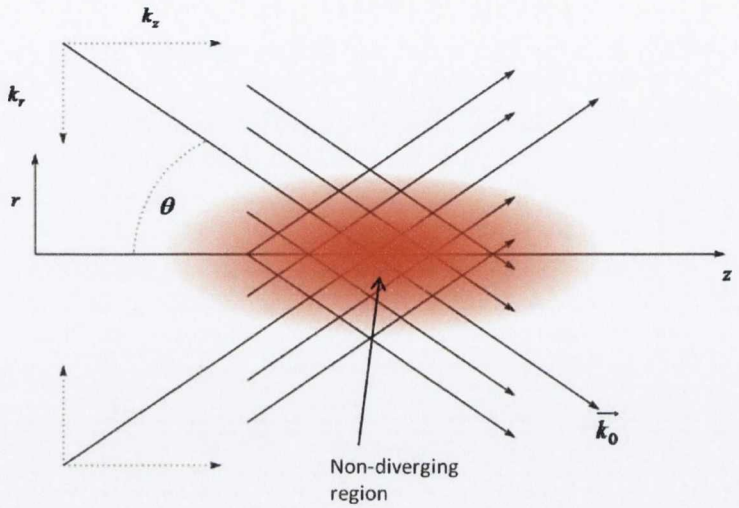

Figure 2.3.1: The wave vectors that form a non-diverging beam. It is obvious from the diagram that in the region along the z axis where the wave vectors intersect an interference pattern will be formed that remains constant over the extent of this region.

The beam described by equation 2.3.1 carries infinite power and, as such, cannot be realized in the laboratory. However, beams that are approximately non-diverging over a certain region of space have been generated. One method, proposed by Durnin is to place a converging lens with focal length f at a distance f from a uniformly illuminated ring shaped aperture (Figure 2.3.2) (Durnin, Miceli, & Eberly, 1987).

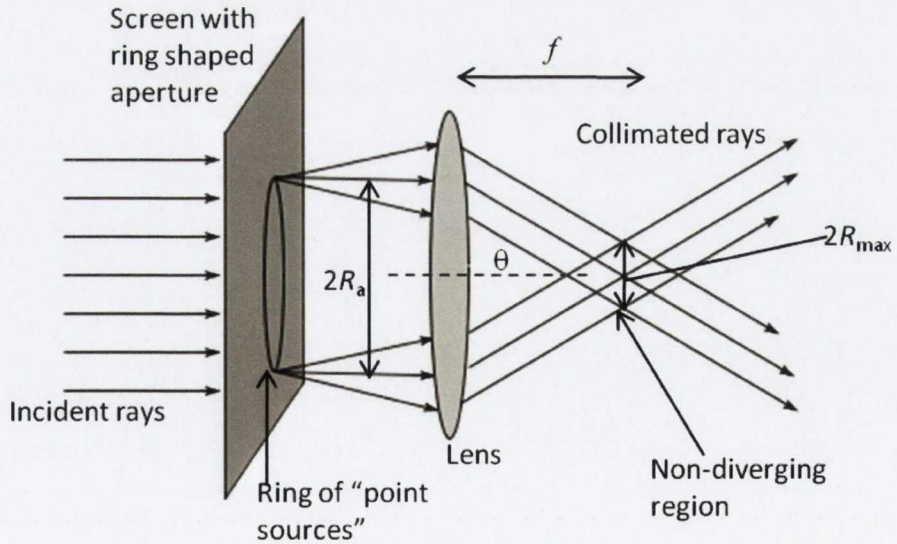

Figure 2.3.2: The optical setup used by Durnin to generate a non-diverging zeroth order Bessel beam. The ring shaped aperture on the screen is approximately a ring of point sources which are collimated into a cone of rays by the lens. f is the focal length of the lens.

The ring shaped aperture can be viewed as an array of point sources located on a ring. Geometrical optics tells us that the light emitted from these sources will be collimated by the lens and since they are located on a ring centred on the optical axis the light will emerge from the lens as a converging cone. This pseudo-non-diverging beam will, of course, not be infinite in extent but will only exist in the region where the rays overlap (Figure 2.3.2). The angle of the cone of rays formed by the setup in Figure 2.3.2 is

$$\theta = \tan^{-1}\left({}^{R_a}/_{f}\right) = \tan^{-1}\left({}^{k_r}/_{k_z}\right) \qquad 2.3.2$$

The longitudinal extent of this overlap region is given by

$$Z_{max} = {}^{R_{max}}/_{\tan\theta}, \qquad 2.3.3$$

where R_{max} is the maximum transverse radius of the Bessel beam.

There is another useful method for approximating Z_{max} that illustrates the advantages of a Bessel beam over a Gaussian with a similar spot size. Say we form a zeroth order Bessel beam with central spot parameter $r_s = {}^{1}/_{k_r}$. For small cone angles we can make the approximation that $\tan\theta = \sin\theta = {}^{k_r}/_{k}$. Combining this approximation with equation 2.3.3 leads to:

$$Z_{max} = {}^{kR_{max}}/_{k_r} = kR_{max}r_s. \qquad 2.3.4$$

If we have an intensity profile consisting of n rings at the position where most rings are visible (the position of R_{max} in Figure 2.3.3), it follows from the properties of Bessel functions that the radius of the beam at that point is approximately

$$R_{max} = {}^{\pi n}/_{k_r} = \pi n r_s. \qquad 2.3.5$$

The distance over which a Gaussian beam with a minimum waist of r_s will remain relatively constant is twice the Rayleigh range, or kr_s^2. Combining equations 2.3.4 and 2.3.5 and using this definition of the Rayleigh range leads to:

$$Z_{max} = 2\pi n Z_r, \qquad 2.3.6$$

where $Z_r = \frac{1}{2}kr_s^2$.

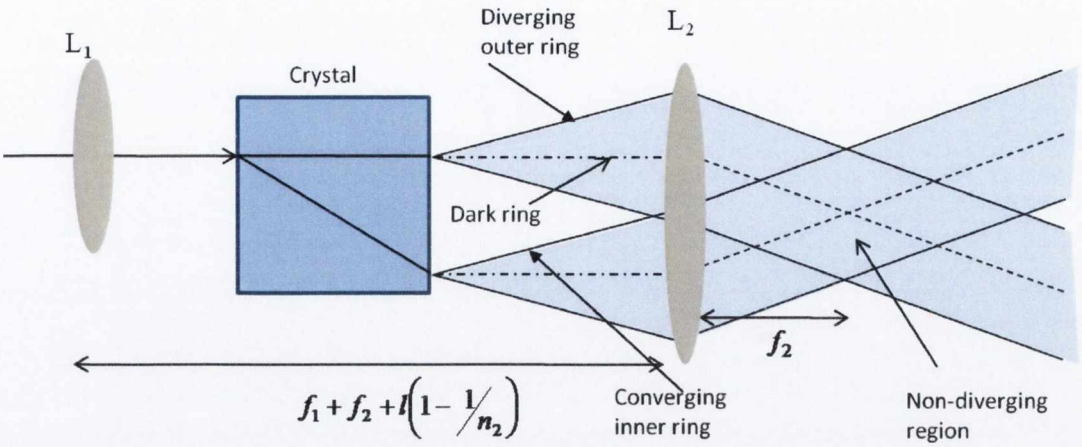

Figure 2.3.3: The optical setup for generating non-diverging beams via conical diffraction. Durnin's ring aperture is replaced by the focal image plane. The ring thickness at L_2 is determined by the waist of the beam incident on the crystal.

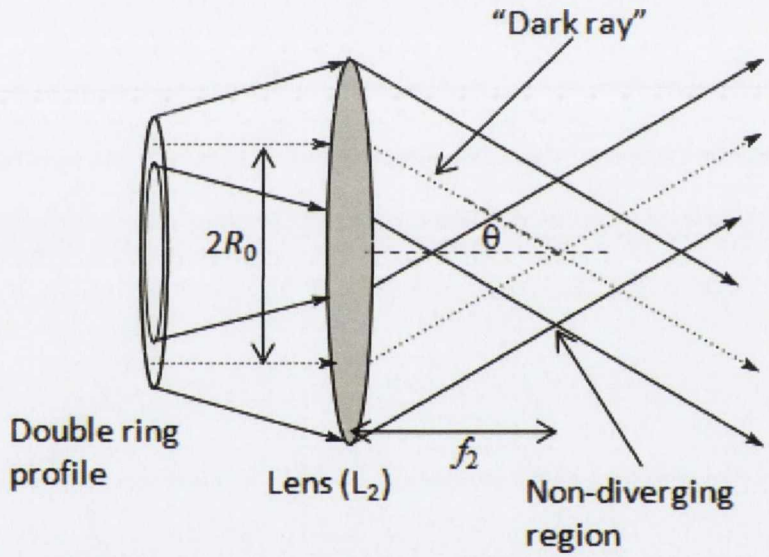

Figure 2.3.4: A closer look at the formation of the non diverging profile in the region near the focal plane of the focusing lens (L_2 in Figure 2.3.3). From the figure it is clear that the argument of the Bessel functions that determine the transverse profile of the non diffracting regions will be the same as in the Durnin method (Figure 2.3.1). The fact that the lens focuses the "dark ray" onto the axis leads us to expect an intensity minimum in the centre of the non-diverging region.

The set up for forming non-diverging Bessel beams via conical diffraction is shown in Figure 2.3.3. We have replaced Durnin's ring shaped aperture with our focal image plane profile. There are two major differences between the Bessel beams formed by conical diffraction and those formed by Durnin's method (or with an axicon). The first is that the Bessel beams formed by conical diffraction have a double peaked on-axis intensity profile. This feature is due to the fact that we are focusing a double rather than a single ring onto the axis. The second difference is that the conical diffraction Bessel beam is a separable superposition of zeroth and first order Bessel beams.

The geometrical optics of Figure 2.3.4 suggests that the transverse profile of the conical diffraction non-diverging beams will have the following form:

$$I_{Non-Div} \propto J_0^2(k_r r) + J_1^2(k_r r) \qquad 2.3.7$$

This is just the far field profile of the conically diffracted beam with the diameters of the Bessel function rings determined by R_0, the particular lens chosen and the wavelength of the light.

It can be seen from equations 2.3.1 – 2.3.3 that the main features of the conical diffraction Bessel beams as well as the Durnin Bessel beams are described by simple formulae. Table 2.3.1 gives a comparison of the main features of conical diffraction Bessel beams formed with a Gaussian with waist ω_0, a crystal with geometric ring radius R_0 and a lens with focal length f and lens aperture w_l with those of the Bessel beams generated with an axicon with cone angle α, refractive index ν and half width w_A, Durnin's ring aperture method for an aperture of radius R_a and combined with a lens with focal length f and lens aperture w_l.

Table 2-1

	Axicon	Conical Diffraction	Durnin
Semi-angle of ray cone θ	$\sin^{-1}(n\sin(\alpha)) - \alpha$	$\tan^{-1}\left({}^{R_0}/_{f}\right)$	$\tan^{-1}\left({}^{R_a}/_{f}\right)$
Radius of 0th order spot	$2.405/k_0\sin\theta$	$2.405/k_0\sin\theta$	$2.405/k_0\sin\theta$
Length of non-diverging region	${}^{w_A}/_{\tan(\theta)}$	${}^{w_l f}/_{R_a}$	${}^{w_l f}/_{R_a}$

From the table we can see that there are three parameters that determine the characteristics of the conical diffraction Bessel beams, namely the waist ω_0 of the incident Gaussian (which determines the thickness of the ring profile in the FIP as well as the thickness of the rings after propagating a distance f), the geometric ring radius R_0 and the focal length f of the lens used. For a given crystal the properties of the non-diverging Bessel beams formed by conical diffraction are controlled by two lenses, L_1 and L_2 in Figure 2.3.3.

Experiment

An experimental set up that was used to generate non-diverging Bessel beams is shown in Figure 2.3.5. This particular experiment was carried out at St. Andrews University with the aid of the optical trapping group (see acknowledgements). The light source used was a frequency doubled Nd:YAG laser that emitted green light with a wavelength of 532 nm. The beam was focused into the same 3 cm biaxial crystal mentioned earlier. The ring plane was formed at the back focal plane of a 20x objective which formed the non-diverging beam in a region surrounding its front focal plane.

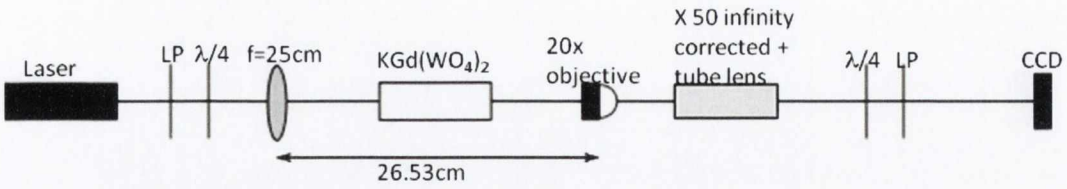

Figure 2.3.5: The optical arrangement used to observe the zeroth and first order non-diverging Bessel beams.

Images were taken of both the zeroth and first order beams at intervals of 5 μm. The on axis intensity in the non-diverging region (the on axis intensity is, by necessity, that of the B_0 component) is plotted in Figure 2.3.6. The length of the region is approximately 1mm.

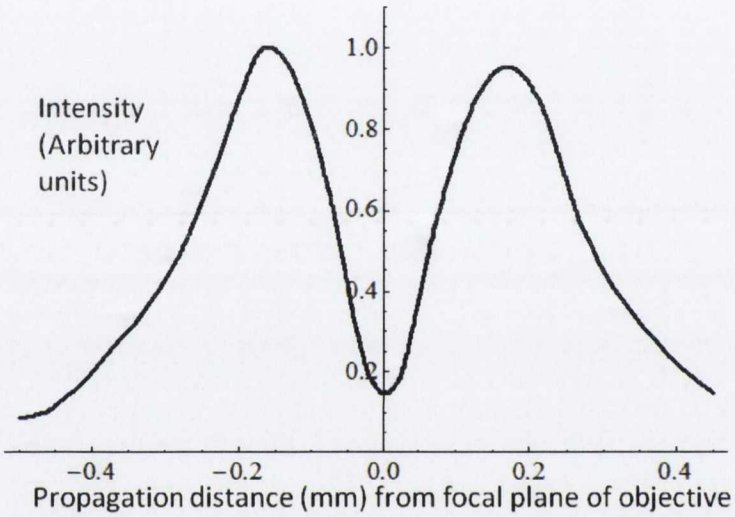

Figure 2.3.6: The on axis intensity profile of the non diverging beam. The double peak is a direct result of the double ring profile of the focal image plane.

Images of the intensity profiles of the non diverging beams are shown in Figure 2.3.7. The FWHM of the non diverging zero order spot is roughly 4 μm. The distance from the centre of the zeroth order profile to the first intensity minimum is also about 4 μm. The formula for the radius of the zeroth order central spot (Table 2.1) predicts a spot of 2.9 μm.

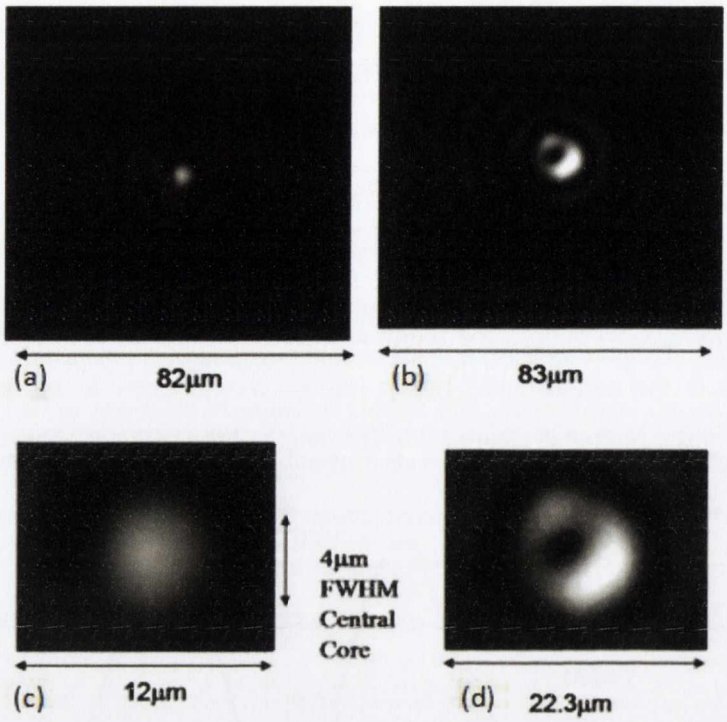

Figure 2.3.7: Images of the non-diverging profiles formed using the experimental setup shown in Figure 2.3.5. (a) the zeroth order beam; (b) the first order beam; (c) a close up image of the zeroth order beam showing the central spot and the first minimum; (d) a close up image of the first order beam.

The experimental setup shown in Figure 2.3.8 was used to compare the predictions of equation 2.3.3 with experiment.

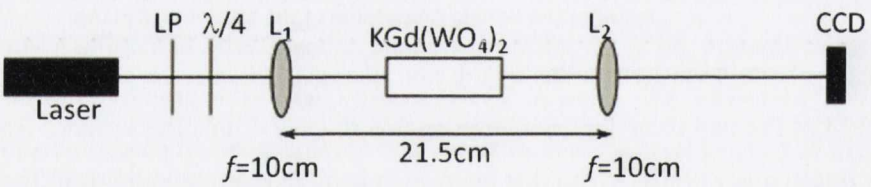

Figure 2.3.8: The experimental setup used to convert the conically diffracted Gaussian into a non diverging beam

Figure 2.3.9 shows the ring profile formed at the back focal plane of the L_2 in Figure 2.3.8 and the non-diverging profile. The two component (B_0 and B_1) beams were not separated.

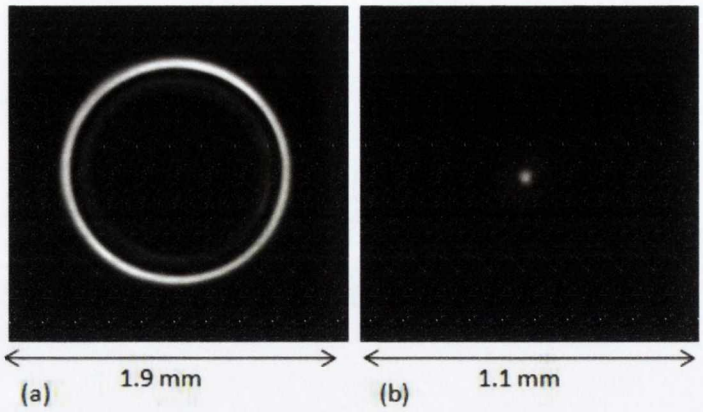

Figure 2.3.9: The ring beam that was formed at the back focal plane of the second lens in Figure 2.3.8. (b) the profile of the beam at a distance of 5.7 mm from the front focal plane of L_2 on the side of the focal plane nearest L_2 (rather than the side nearest the CCD.)

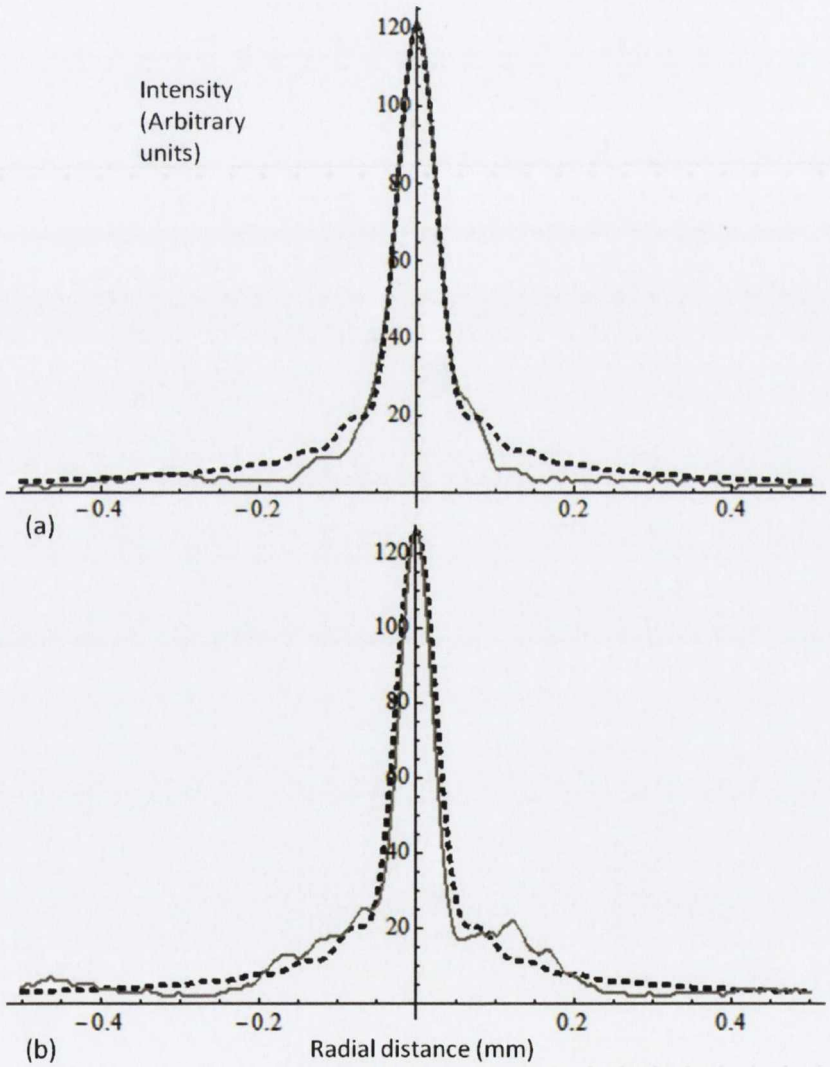

Figure 2.3.10: (a)A comparison of the non-diverging profile formed at a distance of 7 mm from the focal plane of the lens (L_2) in Figure 2.3.8 (continuous line) with theory (dashed line generated form equation 2.3.7); (b) A comparison of the same beam with theory at 5.5 mm from the focal plane of L_2

Chapter 3. Cascade conical diffraction

This chapter deals with conical diffraction of a Gaussian beam by a series, or cascade, of biaxial crystals with the optic axes of all crystals in the cascade being aligned along the propagation direction of the incident beam. An intuitive picture of cascade conical refraction is developed in section 3.1 followed by the extension of paraxial theory, in section 3.2, to cases involving more than one crystal in combination with various wave plates. In section 3.3 the qualitative and quantitative predictions made in section 3.2 are compared with experiment.

Although the initial motivation for the research on cascade conical refraction/ diffraction presented here was curiosity, there has been interest shown in cascade conical diffraction by other groups for a number of reasons. Berry has recently produced a paraxial optics theory for a cascade of N biaxial crystals by writing a Hamiltonian for the entire system (Berry, 2010). Prior to that King et al had investigated the transformation of Bessel beams by cascade conical diffraction both theoretically and experimentally (King, Hogervorst, Kazak, Khilo, & Ryzhevich, 2001). The motivation for Berry's work was the research of Abdolvand et al into using a biaxial crystal with gain as part of a laser resonator, the reflected beam passing back and forth through the crystal being akin to a light beam passing through a series of crystals, one after the other (Abdolvand, Wilcox, Kalkandjiev, & Rafailov, 2010). Peet has used cascade conical diffraction with two biaxial crystals to shape a Gaussian beam including conversion into second order Laguerre-Gaussian (Peet, 2010(b)). It is also possible to use cascade conical diffraction to modify the orbital angular momentum of a paraxial light beam. The OAM beams that can be generated by a cascade of two biaxial crystals have been investigated by our group and the main results will be mentioned in section 3.2 but the OAM properties of the cascade conically diffracted beams will not be studied in detail in this thesis.

3.1. Cascade conical refraction

In this section we look at conical refraction of a ray of light incident on a series (cascade) of more than one crystal with the optic axes of the crystals aligned. In what follows we will try to intuit what will happen in the general case of conical refraction by more than one crystal, before developing paraxial cascade conical diffraction theory for two crystals in section 3.2 and comparing it with experiment in section 3.3. In what follows, when we discuss scenarios involving more than one crystal, we will assume that each crystal has the same principal refractive indices and cone angle. This implies that the geometric ring radius associated with each crystal is proportional to its length. It should also be remembered that ray and wave directions are the same in free space and different in a biaxial crystal. When dealing with conical refraction, we are concerned with the refracted ray directions that correspond to an incident wave direction.

In order to figure out what will happen in the case of cascade conical refraction, we will use as a starting point the picture developed in section 1.3 of the cone of refracted rays as the envelope of double refracted rays corresponding to the set of the incident waves that make an angle θ with the optic axis (i.e. a set of incident wave-vectors with the tips of the vectors forming a small circle centred on the optic axis (Figure 3.1.1)) in the limit of θ going to zero (Figure 3.1.2).

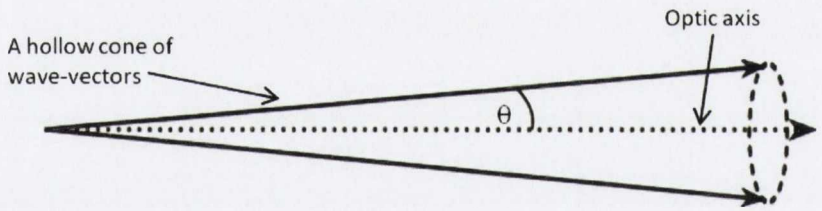

Figure 3.1.1: A cone of rays, all of which are oriented at an angle θ to the optic axis (dashed line).

We will also make use of the fact that the conically refracted cylinder of rays that emerges from the crystal is linearly polarized at every point on its ring profile with the polarization direction rotating by π in a circuit of the ring, the polarization is tangential at the straight through position and rotates in the same sense as the that of the circuit of the ring.

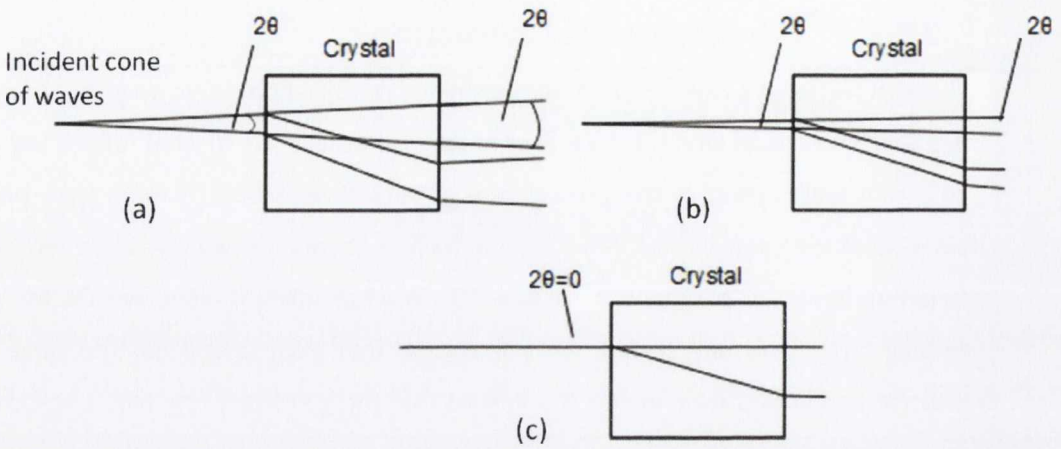

Figure 3.1.2: (a) All of the waves incident at angle θ to the optic axis are double refracted. (b) As θ goes to zero the envelope of double refracted rays forms the cone of refraction. (c) The transition to conical refraction is complete with θ = 0.

We can consider the transformation of this beam (the cylinder of rays after conical refraction) by a second crystal, one ray at a time. First we consider the two crystals to be aligned and the same length.

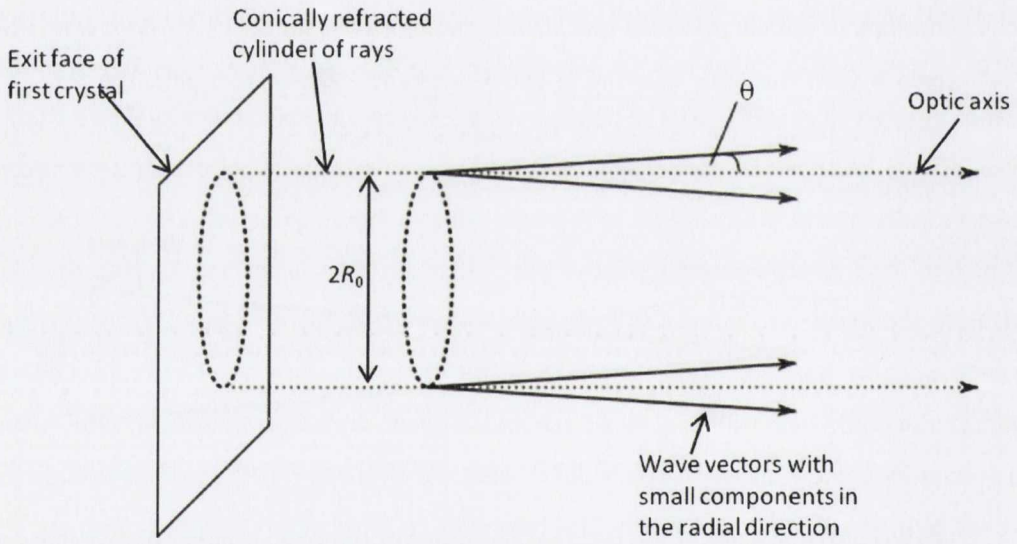

Figure 3.1.3: The cylinder of conically refracted rays viewed as a diverging and converging cone of wave vevtors with each wave vector off making an angle θ with the optic axis. As θ goes to zero the diverging and converging cones merge into the cylinder of conical refraction.

Each wave will be directed slightly off axis and will hence be double refracted to give rays propagating to points on the crystals exit face very close to points on a ring of radius R_0. This leads to the situation depicted in Figure 3.1.4 where we can see that the beam that emerges from the crystal has the form of a diverging ring of rays surrounding a diverging cone of rays in the centre of the ring.

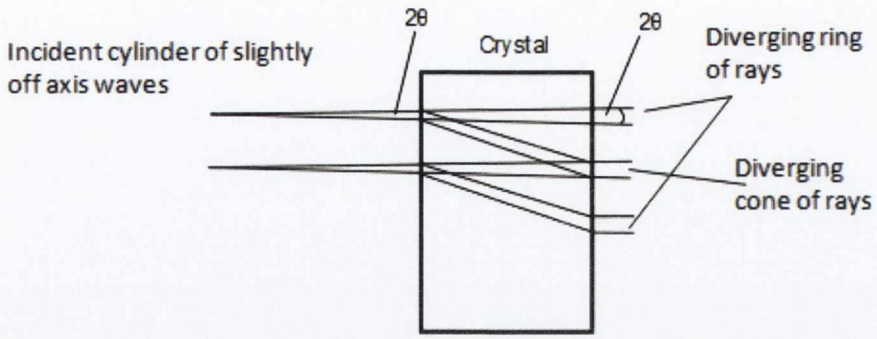

Figure 3.1.4: A slightly diverging cylinder of rays incident on a biaxial crystal. Each ray (wave) on the incident cylinder has a small component in the radial direction with the radius drawn from the centre of the cylinder.

If we specify that the second crystal has a different geometric ring radius from the first crystal then the emerging beam has the form of two concentric diverging rings with radii equal to the sum and difference of the radii of the two individual crystals, the difference of the radii going to zero in the case of crystals of equal length.

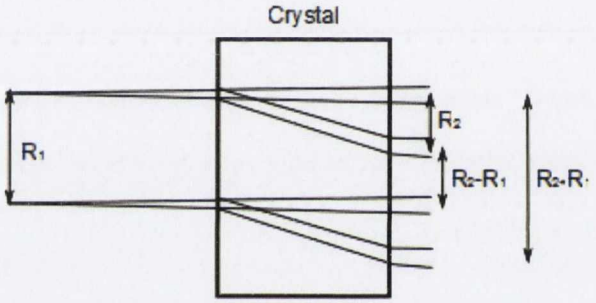

Figure 3.1.5: A cylinder of rays, all of which are at an angle of θ to the optic axis, with radius R_1 is transformed by a crystal with geometric ring radius R_2 into a two concentric cylinders with radii of $R_2 + R_1$ and $R_2 - R_1$.

However, the rays entering the second crystal are linearly polarized so double refraction will not necessarily occur and each incident ray will be sent to a position on the characteristic ring of conical refraction that is determined by its off axis direction. In the incident cylinder each ray is directed slightly off axis in the radial direction with the radius being drawn from the centre of the cylinder. Thus in the case of the second crystal being aligned with the first one each ray on the cylinder will be directed off axis such that the incident rays will be double refracted into rays in the second crystal with polarization vectors parallel and perpendicular to those of the incident ray. Thus double refraction will not occur as the ray in the crystal with polarization perpendicular to that of the incident ray will not propagate and we have the situation depicted in Figure 3.1.6 with the incident cylinder being transformed into a cylinder of twice its radius.

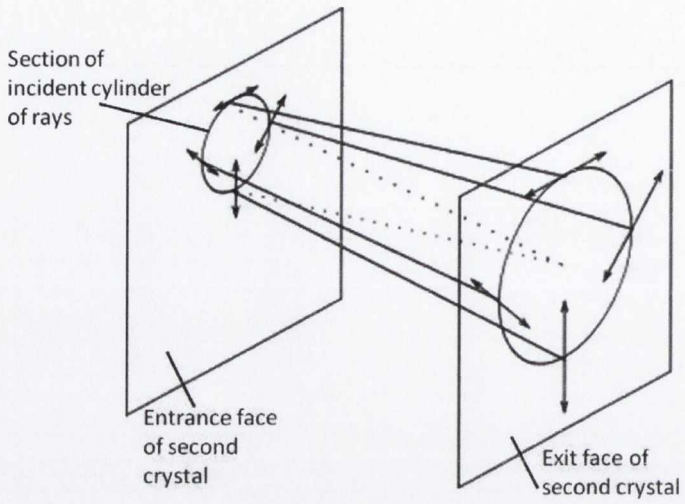

Figure 3.1.6: The entrance and exit faces of the second crystal in the case of two successive conical refractions of an incident ray. Double refraction does not occur for each ray on the incident cylinder since each incident ray is polarized orthogonally to one of the double refracted rays corresponding to its direction. The dashed lines show the directions along which the double refracted rays that do not propagate would travel.

Next we consider a relative rotation of the second crystal about the optic axis. In this case we are still dealing with a double ring of rays incident on the second crystal with each ray directed slightly off axis. However this time double refraction will occur for each ray. It is easy to see this if we just consider one ray at a time, for example the straight through ray. The straight through ray is polarized tangentially to the cylinder of conical refraction. For concreteness we will consider the straight through ray to be polarized along the horizontal (x) axis and the transverse displacement of the incident ray by the first crystal to have magnitude R_1 along the negative y axis. Rotating the 2nd crystal by angle α will rotate the offset direction of the cone of refraction by the same angle, thus the tangential polarization component will not be horizontal for the second crystal but will be rotated by α.

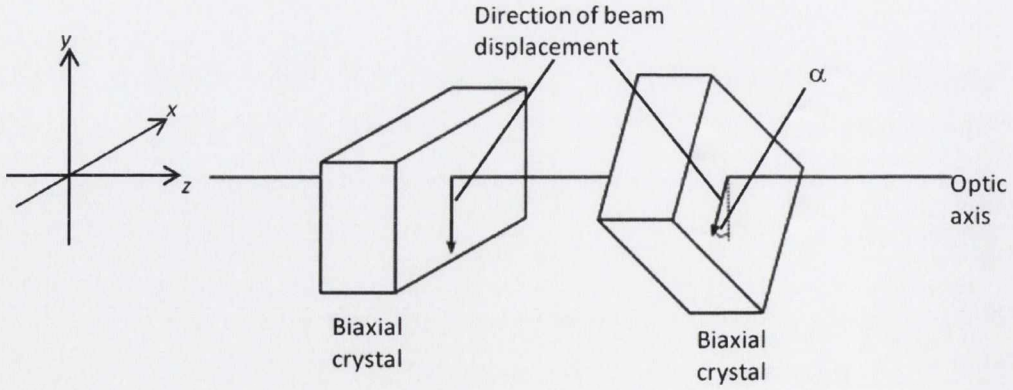

Figure 3.1.7: Two biaxial crystals in cascade with the second rotated by the angle α relative to the first. The direction of transverse displacement induced by conical refraction is also rotated by α.

Thus the horizontally polarized ray will be double refracted into rays with polarization vectors at angles of α and $\frac{1}{2}\pi+\alpha$ to the horizontal direction with the power divided between these two refracted rays. These rays will be refracted to positions separated by $2R_2$. This process is illustrated in figure 3.1.8

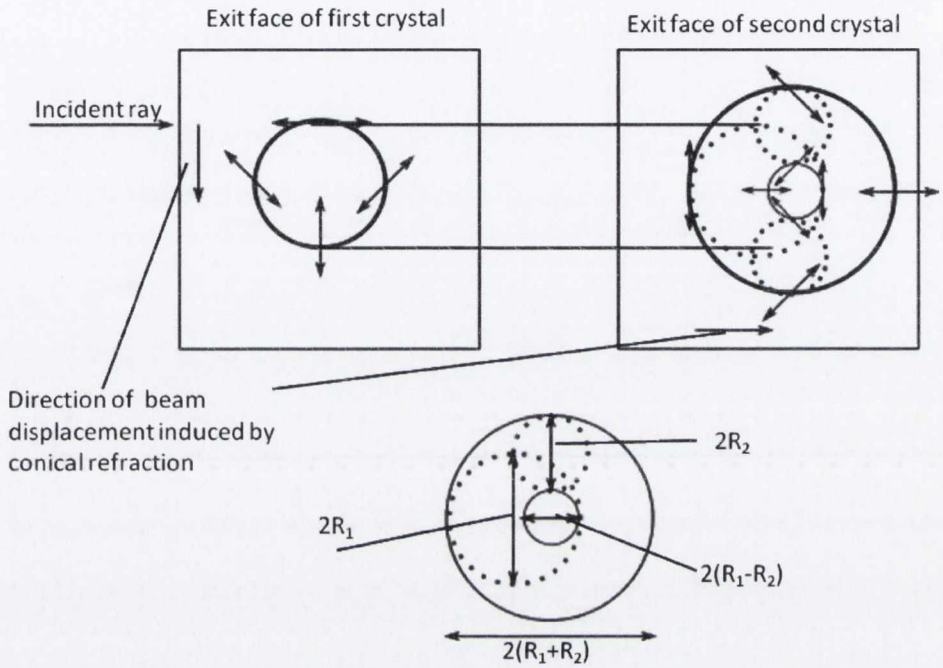

Figure 3.1.8: A schematic showing the process of cascade conical refraction with a relative rotation of 90°. The ring profile generated by the first crystal is represented on the second crystal as a dashed circle of radius R_1. In the diagram points on that circle generate further circles with radii R_2. The net effect is to generate a pair of rings with radii of $R_2+ R_1$ and $R_2- R_1$.

Referring to Figure 3.1.8 we can see that we can see that our cascade of two consecutive crystals will in general transform an incident set of slightly off axis rays into two concentric ring profiles, each one of which both converges towards the optic axis and diverges from it and in the limit of our incident ray being exactly along the optic axis we will have two parallel concentric cylinders of light emerging from the cascade with radii given by the sum and difference of the geometric ring radii of the two crystals in the cascade. The relative intensity in the inner and outer rings is solely dependent on α with all the power being in the outer ring for $\alpha = 0$ and all of the power in the inner ring for $\alpha = \pi$. In a cascade of two crystals with a relative rotation and with the second crystal having a smaller geometric ring radius than the first one, the polarization profile of the inner cylinder is rotated by 180° about the optic axis relative to the polarization profile of the outer ring. To understand why this is, it is best to refer to Figure 3.1.9 where process is represented schematically. On both parts of the diagram we look at two cases of double refraction in the second crystal for rays at two diametrically opposite points on

the cylinder incident on the second crystal. In the case of the second crystal having a smaller geometric ring radius than the first one (part (a)) each point on the incident cylinder is double refracted into mutually orthogonally polarized rays, one being refracted to a certain azimuthal position on the large ring emerging from the cascade (large black circle) and the other being refracted to the same azimuthal position on the inner ring. Thus if we draw a radial line from the centre emerging beam it will pass through a point that is polarized in a given direction on the inner ring and in a direction orthogonal to that in the outer ring. If the second crystal has a geometric ring radius greater than that of the first one (part (b)) then each ray is double refracted into orthogonally polarized rays, one propagates to a given point on the outer ring and the other to a point diametrically opposite the corresponding point on the inner ring.

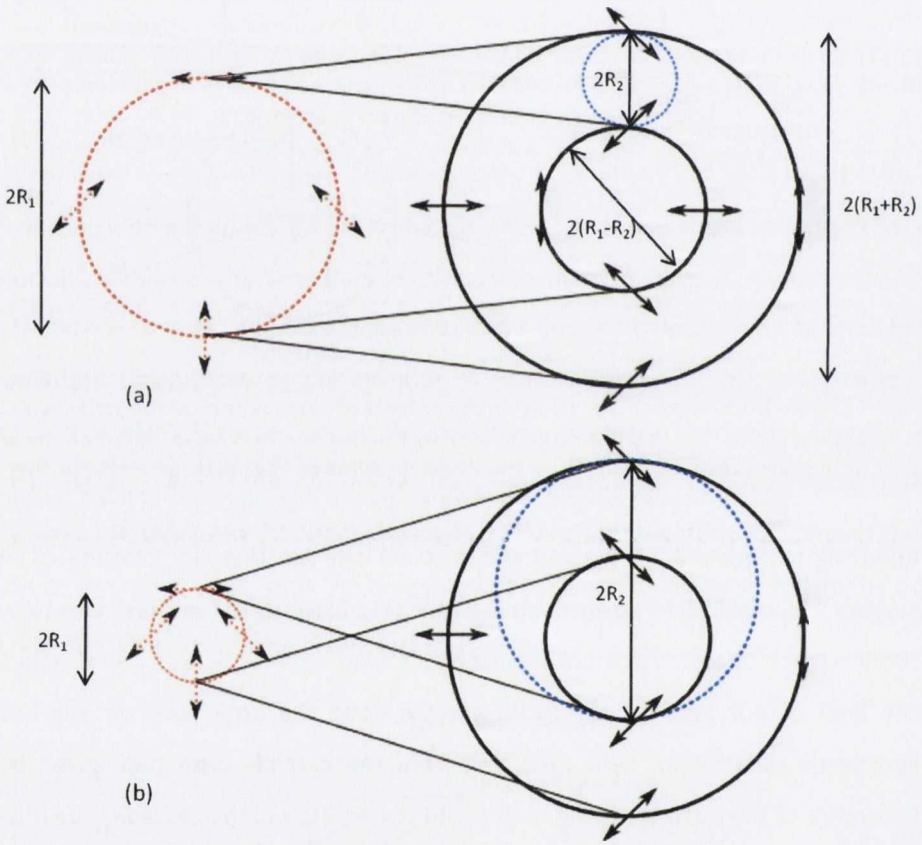

Figure 3.1.9: A schematic to illustrate why the polarization of the cascade conically refracted rays depend on the order of the crystals. In both figures the black concentric rings represent the ring profiles after cascade conical refraction by a crystal with geometric ring radius R_1 followed by a crystal with geometric ring radius R_2. In part (a), $R_1 > R_2$. In part (b) $R_1 < R_2$. In both cases there is a relative rotation of 90° between the crystals.

If we have linearly polarized incident light on the cascade depicted in Figure 3.1.9 we will have two concentric crescent beams. The crescents will have intensity maxima at the same azimuthal position in the case of the second crystal having a larger geometric ring radius than the first and at diametrically opposite points in the case of the second crystal having a smaller

geometric ring radius than the first.

The situation just described obviously generalizes to more than two crystals since each ring will just be refracted into a pair of rings with radii depending only on the radius of the incident ring and the geometric radius of the crystal through which it is propagating. Hence a cascade of N consecutive crystals will produce a beam consisting of 2^{N-1} concentric rings with radii given by the sum and differences of all of the radii in the cascade.

In the next section we will develop paraxial cascade conical diffraction. Intuitively we expect this to resemble the transition from conical refraction to conical diffraction i.e. the ring profile is replaced by a double ring with the outer ring diverging and the inner ring converging. In cascade conical diffraction we might expect each concentric ring profile to be replaced by the diffracting double ring.

3.2. Cascade conical diffraction

In this section we extend the paraxial conical diffraction theory that was developed in section 1.4 to the cascade arrangement introduced in the previous section (3.1). We will see that the integral expressions obtained confirm the intuitive picture presented in the previous section as well as providing precise predictions.

It was shown in section 1.4 that a paraxial beam of light with transverse electric field profile given by $\vec{E}(\vec{r},0)$, with Fourier transform $\vec{a}(\vec{P})$, is transformed by propagation along the optic axis of a biaxial crystal with geometric ring radius R_0 into

$$\vec{E}(\vec{r},Z) = \frac{k}{2\pi}\iint dP e^{-ik\vec{P}\cdot\vec{r}} e^{-\frac{1}{2}ikP^2 z}\,[\cos(kPR_0)\,\boldsymbol{I} - i\sin(kPR_0)\,\boldsymbol{M}(\varphi_P)]\vec{a}(\vec{P}), \qquad 3.2.1.$$

where

$$\boldsymbol{I} = \begin{pmatrix} 1 & 0 \\ 0 & 1 \end{pmatrix} \;\&\; \boldsymbol{M}(\varphi) = \begin{pmatrix} \cos\varphi & \sin\varphi \\ \sin\varphi & -\cos\varphi \end{pmatrix}. \qquad 3.2.2.$$

If we presume that the incident beam is circularly symmetric and uniformly polarized then the above equation reduces, on integration over φ_P, to

$$\vec{E}(\vec{r},z) = (\mathrm{B}_0\boldsymbol{I} + \mathrm{B}_1\boldsymbol{M}(\varphi))\begin{pmatrix} e_x \\ e_y \end{pmatrix}. \qquad 3.2.3.$$

From the above equations we can infer that under conical diffraction the Fourier transform of the incident beam $\vec{a}(\vec{P})$ is transformed into

$$e^{-\frac{1}{2}ikP^2Z}\left[\cos(kPR_0)\,\boldsymbol{I} - i\sin(kPR_0)\boldsymbol{M}(\varphi_p)\right]\vec{a}(\vec{P}). \qquad 3.2.4.$$

Now if we set this to be the incident beam, we can generate the Fourier transform of the beam after propagation through successive biaxial crystals by matrix multiplication. This procedure can obviously be repeated as many times as we require and is the basic method underlying the derivations of the integral expressions that we obtain in this chapter.

In what follows we will re-define the effective propagation distance Z to take into account the propagation through more than one crystal. This is easily done by adding another crystal to the Hamiltonian introduced in Section 1.4. Recall that that Hamiltonian split into two parts with one describing propagation in the crystal and the other describing propagation in free space.

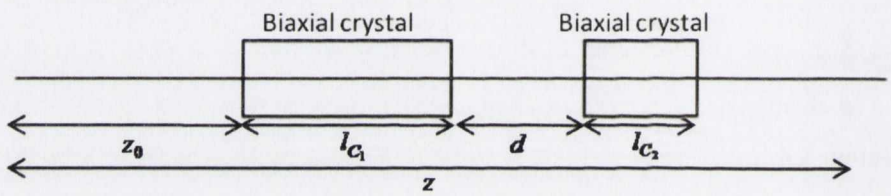

Figure 3.2.1: A cascade of two biaxial crystals. Propagation through the two (or more) crystals can be implemented with a generalization of the Hamiltonian used in Chapter 1. The incident beam propagates from a distance of z_0 behind the first crystal to a position z located beyond the final crystal in the cascade.

The Hamiltonian for a series of crystals with a series of distances between then can be written as

$$\begin{aligned}\boldsymbol{H} = \boldsymbol{H}_f U(z_0 - z) + \boldsymbol{H}_{C_1} U(z - z_0)U(l_{C_1} + z_0 - z) + \boldsymbol{H}_f U(z \\ - (l_{C_1} + z_0))U(l_{C_1} + z_0 + d - z) + \boldsymbol{H}_{C_2} U(z \\ - (l_{C_1} + z_0 + d))U(l_{C_1} + z_0 + d + l_{C_2} - z) \\ + \boldsymbol{H}_f U(z - (l_{C_1} + z_0 + d + l_{C_2})) + \cdots\end{aligned} \qquad 3.2.5.$$

where $\boldsymbol{H}_f$ is the Hamiltonian for free space propagation and $\boldsymbol{H}_{C_i}$ is the Hamiltonian for the i^{th} crystal which has length l_i. Integrating this expression with respect to propagation distance z to a point beyond the 2nd crystal (we will consider just two crystals here, the argument easily generalizes) leads to

$$\int_0^z \boldsymbol{H}(z`)dz` = \boldsymbol{H}_f\left(z - (l_{C_1} + l_{C_2})\right) + \boldsymbol{H}_C(l_{C_1} + l_{C_2}). \qquad 3.2.6.$$

Comparing equation 3.2.6 with the theory for one crystal (Section 1.4) it is clear that for more than one crystal we must re-define the effective propagation distance Z which measures distance from the FIP, as

$$Z = l_{tot} + n_2(z - l_{tot}) \qquad 3.2.7.$$

where l_{tot} is the sum of the lengths of all the crystals in the cascade. Now we will look at some specific cases of cascade conical diffraction for the case of two biaxial crystals with various combinations of wave plates between the crystals that manipulate the polarization state of the conically diffracted beam before it is conically diffracted in the second crystal.

A: Crystals aligned

The simplest case of cascade conical diffraction is where all the crystals have their optic axes aligned in the same direction (nominally the z axis) and the transverse displacement of the cone generated by each crystal is in the same direction. The result, easily obtained by repeated matrix multiplication which we omit here, is that a series of crystals with characteristic ring radii R_i will transform an incident Gaussian into a ring-shaped profile with geometric ring radius $\sum_i R_i$. This is what we had expected from the picture developed in the last chapter and is also to be expected since the series of perfectly aligned crystals is equivalent to a single crystal of the combined length of the series.

This trivial case can be made more interesting if we consider the possibility of placing wave plates between the crystals. As noted earlier the process of conical diffraction is dependent on the polarization of the incident beam and if we manipulate the polarization of the conically diffracted beam before propagating it through a second crystal, we no longer have the simple case of the ring profile being merely transformed into a bigger ring profile.

An interesting example of manipulating the polarization of the conically diffracted beam in the context of cascade conical diffraction is that of selecting the B_1 beam using a circular analyzer, then circularly polarizing it and sending it through a second crystal (Figure 3.2.2).

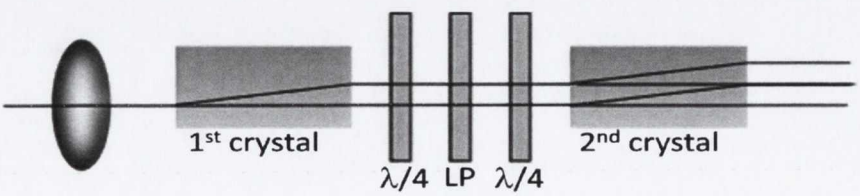

Figure 3.2.2: A cascade of two biaxial crystals with the combination of wave-plates used to select either of B_0 or B_1 and circularly polarize it before it propagates through the second crystal.

If we have a left-circularly polarized incident beam with Fourier transform $a(P)$, the conically diffracted beam is given by

$$\begin{aligned}\vec{E}(r,\varphi,Z) &= \mathrm{B}_0\begin{pmatrix}1\\ i\end{pmatrix} + \mathrm{B}_1\begin{pmatrix}\cos\varphi & \sin\varphi\\ \sin\varphi & -\cos\varphi\end{pmatrix}\begin{pmatrix}1\\ i\end{pmatrix}\\ &= \mathrm{B}_0\begin{pmatrix}1\\ i\end{pmatrix} + \mathrm{B}_1 e^{i\varphi}\begin{pmatrix}1\\ -i\end{pmatrix}.\end{aligned} \qquad 3.2.8.$$

If we select B_1 with a right-circular analyzer and then left-circularly polarize it, we are left with a field given by

$$\vec{E}(r,\varphi,Z) = \mathrm{B}_1 e^{i\varphi}\begin{pmatrix}1\\ i\end{pmatrix} = \mathrm{B}_1\begin{pmatrix}\cos\varphi & \sin\varphi\\ -\sin\varphi & \cos\varphi\end{pmatrix}\begin{pmatrix}1\\ i\end{pmatrix}, \qquad 3.2.9.$$

which has the Fourier transform

$$e^{-\frac{1}{2}ikP^2Z}\left[-i\sin(kPR_0)\begin{pmatrix}\cos\varphi_P & \sin\varphi_P\\ -\sin\varphi_P & \cos\varphi_P\end{pmatrix}a(P)\right]\begin{pmatrix}1\\ i\end{pmatrix}. \qquad 3.2.10.$$

Using equation 3.2.4, it can be seen that the FT of the beam that emerges from the 2nd crystal is

$$\begin{aligned}e^{-ikP^2\mathrm{Z}}&\left[\cos(kPR_0)\,\boldsymbol{I} - i\sin(kPR_0)\begin{pmatrix}\cos\varphi_P & \sin\varphi_P\\ \sin\varphi_P & -\cos\varphi_P\end{pmatrix}\right]\\ &\times\left[-i\sin(kPR_0)\begin{pmatrix}\cos\varphi_P & \sin\varphi_P\\ -\sin\varphi_P & \cos\varphi_P\end{pmatrix}\right]\\ &\times a(P)\begin{pmatrix}1\\ i\end{pmatrix},\end{aligned} \qquad 3.2.11.$$

where the effective propagation distance is defined for the case of two crystals with equal lengths as $\mathrm{Z} = 2l + (z - 2l)n_2$. Expression 3.2.11 simplifies to:

$$\begin{aligned}e^{-ikP^2\mathrm{Z}}\,a(P)&[-i\cos(kPR_0)\sin(kPR_0)e^{i\varphi}\begin{pmatrix}1\\ i\end{pmatrix}\\ &-\sin^2(kPR_0)e^{2i\varphi_P}\begin{pmatrix}1\\ -i\end{pmatrix},\end{aligned} \qquad 3.2.12.$$

which leads to a field given by

$$\vec{E}(r,\varphi,\mathrm{Z}) = \mathrm{B}_{12}e^{i\varphi}\begin{pmatrix}1\\ i\end{pmatrix} + \mathrm{B}_{22}e^{2i\varphi}\begin{pmatrix}1\\ -i\end{pmatrix}, \qquad 3.2.13.$$

with

$$\mathrm{B}_{12}(r,\mathrm{Z}) = \frac{k}{2}\int_0^\infty P\sin(2kPR_0)a(P)e^{-ikP^2\mathrm{Z}}J_1(kPr)\,dP, \qquad 3.2.14.$$

$$B_{22}(r,Z) = k\int_0^\infty P\sin^2(kPR_0)a(P)e^{-ikP^2Z}J_2(kPr)dP. \qquad 3.2.15.$$

In the notation B_{i2}, the *i* subscript refers to the order of the Bessel function in the integral and the 2 subscript refers to the fact that the beam has been conically diffracted twice. If, instead of selecting B_1 and left-circularly polarizing it, we select B_1 and right-circularly polarize it, then the final field is given by

$$\vec{E}(r,\varphi,Z) = B_{12}e^{i\varphi}\begin{pmatrix}1\\-i\end{pmatrix} + B_{02}\begin{pmatrix}1\\i\end{pmatrix}, \qquad 3.2.16.$$

with

$$B_{02}(r,Z) = -k\int_0^\infty P\sin^2(kPR_0)a(P)e^{ikP^2Z}J_0(kPr)dP. \qquad 3.2.17.$$

Comparing equations 3.2.13 and 3.2.16 we can see that, depending on the sense in which the selected B_1 field is circularly polarized, we can decide whether the beam that emerges from the 2nd crystal will be a superposition of 0th and 1st order vortex beams or 1st and 2nd order vortex beams. The separate vortex beams in the superposition will be orthogonally polarized and thus the process of selecting one of the components for propagation through the next crystal in the cascade can obviously be repeated.

The focal image plane profiles of the B_{02}, B_{12} and B_{22} components are shown in Figure 3.2.3.

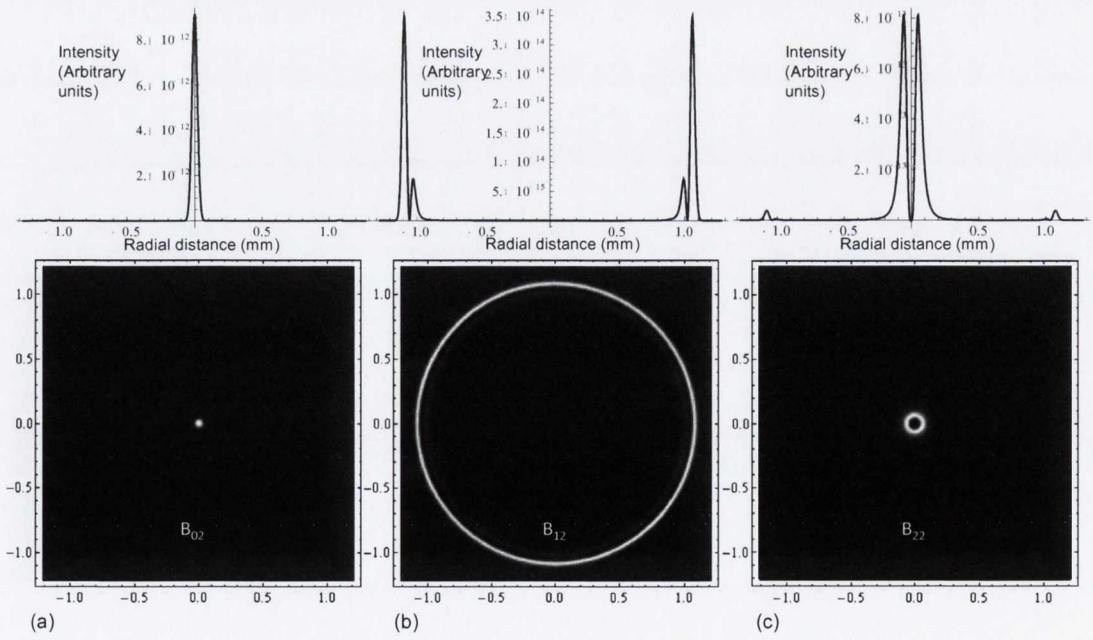

Figure 3.2.3: Focal image plane profiles of the (a) B_{02}; (b) B_{12} and (c) B_{22} components that occur when the B_1 beam is conically diffracted. The conically diffracted (circularly polarized) B_1 beam is either a superposition of B_{02} and B_{12} or a superposition of B_{12} and B_{22}.

In general, a circularly polarized incident beam, after emerging from an *N* crystal cascade will be a superposition of terms of the form

$$a_{in}(P)e^{im\varphi_P}\vec{e}_{\pm}, \qquad 3.2.18.$$

where m can be any integer between zero and *N*, $a_{in}(P)$ is the Fourier transform of the radial profile of the beam incident on the first crystal and $\vec{e}_+/\vec{e}_-$are the polarization vectors for left/right circular polarization. The real space profiles of the beams given by expression 3.2.18 are given by:

$$e^{im\varphi}k\int_0^\infty Pa_{in}(P)J_m(kPr)e^{-\frac{1}{2}ikP^2Z_N}\,dP\vec{e}_{\pm}. \qquad 3.2.19.$$

where Z_N is the effective propagation distance for an *N* crystal cascade. Equation 3.2.4 tells us that conical diffraction will transform expression 3.2.18 into:

$$e^{-\frac{1}{2}ikP^2Z_{N+1}}a_{in}(P)\,[\cos(kPR_0)\,e^{im\varphi_P}\vec{e}_{\pm} - i\sin(kPR_0)\,e^{i(m\pm1)\varphi_P}\vec{e}_{\mp}, \qquad 3.2.20.$$

corresponding to the real space profile

$$k\int_0^\infty Pa_{in}(P)e^{-\frac{1}{2}ikP^2Z_N}[\cos(kPR_0)\,J_m(kPr)e^{im\varphi}\,\vec{e}_{\pm} - i\sin(kPR_0)J_{m+1}(kPr)e^{i(m\pm1)\varphi_P}\vec{e}_{\mp}]dP. \qquad 3.2.21.$$

Placing a half wave plate between the crystals has the interesting effect of interchanging the circular polarizations of the B_0 and B_1 components, before propagation through the second crystal. The result is a beam that is a superposition of three integral components with two of these having the same polarizations and the other being orthogonally polarized. The equation describing this beam is derived in much the same way as in the previous derivation. The result is

$$\vec{E}(r,\varphi,Z) = B_{02}\begin{pmatrix}1\\ i\end{pmatrix} - 2B_{12}\cos\varphi\begin{pmatrix}1\\ -i\end{pmatrix} + B_{22}e^{2\varphi}\begin{pmatrix}1\\ i\end{pmatrix} \qquad 3.2.22.$$

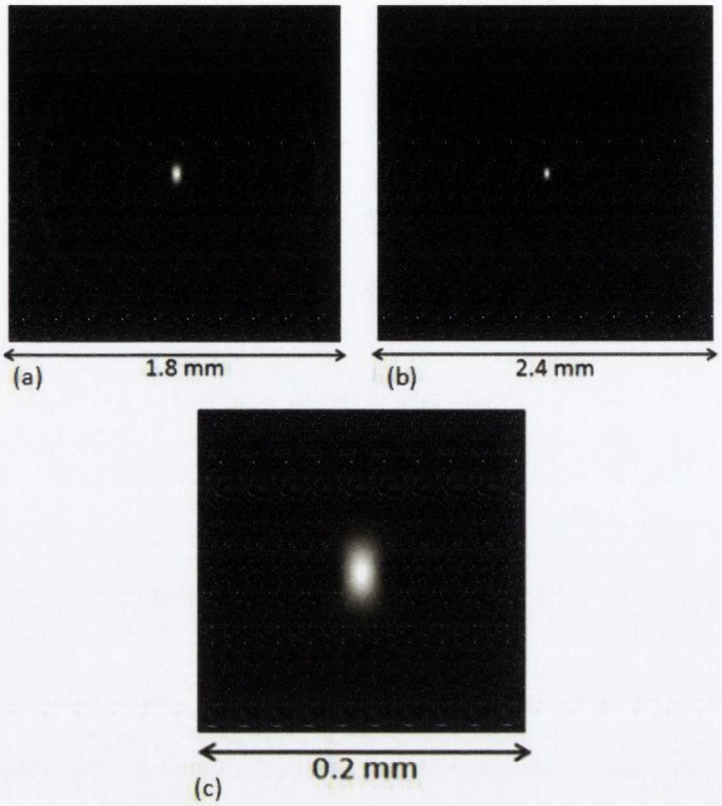

Figure 3.2.4: The focal image plane intensity profile of a Gaussian after propagation through a cascade of two biaxial crystals separated by a half wave plate. (a) A Gaussian with a 25 μm waist is transformed into this profile. (c) Profile obtained for a Gaussian with a 50 μm. (c) A close up of the central spot from part (a). For parts (a) and (c) $R_0 = 0.37$ mm. For part (b) $R_0 = 0.53$ mm

The FIP intensity profile predicted by equation 3.2.2 is shown in Figure 3.2.4. It consists of a ring profile that is modulated by two intensity minima at diametrically opposite points centred on an intensity spot that has a similar angular modulation. A line connecting the angular intensity minima of the central spot would be orthogonal to a line connecting the angular intensity minima of the ring profile. The reason for this can be seen in the effect of the half wave plate on the polarization profile of the conically diffracted beam. It will rotate the polarization at two diametrically opposite points, say the points located at azimuthal positions of 0° and 180°, by 90° while leaving the polarizations at azimuthal positions of 90° and 270° unchanged.

B: A relative rotation of one of the crystals.

Now we will consider cascade conical diffraction with a relative rotation of one of the crystals about their common optic axis (z axis).

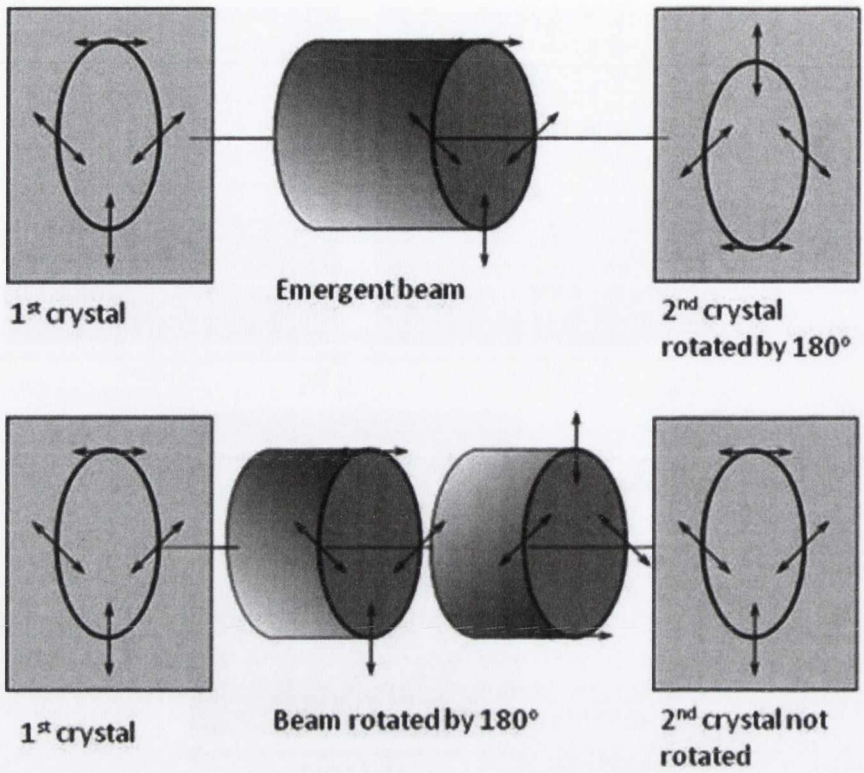

Figure 3.2.5: An illustration of the mathematical trick of rotating the beam incident on the second biaxial crystal rather than the crystal. The situations are physically equivalent so long as we remember that the beam that emerges from the second crystal must be rotated by the same angle in the opposite sense as the first rotation. The polarization distribution on each crystal face identifies the orientation of that crystal.

When considering the propagation of a conically diffracted paraxial beam through a 2nd biaxial crystal which is rotated by an angle α about the optic axis, it is (mathematically) easier to rotate the incident beam in the opposite sense by the same angle (see Figure 3.2.5). To do this we first rotate the beam relative to the co-ordinate system by α

$$\vec{E}(\vec{r}, Z) = \vec{E}(r, \varphi, Z) \rightarrow \vec{E}(r, \varphi - \alpha, Z) \qquad 3.2.23.$$

Next we rotate the polarization vectors by applying the rotation matrix

$$\boldsymbol{R}(\alpha) = \begin{pmatrix} \cos(\alpha) & -\sin(\alpha) \\ \sin(\alpha) & \cos(\alpha) \end{pmatrix} \qquad 3.2.24.$$

$$\vec{E}(\vec{r}, Z) = \vec{E}(r, \varphi, Z) \rightarrow \boldsymbol{R}(\alpha)\vec{E}(r, \varphi - \alpha, Z). \qquad 3.2.25.$$

This leads to

$$\vec{E}(\vec{r}, Z) = (\mathrm{B}_0\boldsymbol{R}(\alpha) + \mathrm{B}_1\boldsymbol{M}(\varphi)) \begin{pmatrix} e_x \\ e_y \end{pmatrix}. \qquad 3.2.26.$$

(Both of these steps could also be taken experimentally by rotating the beam's image with a pair of Dove prisms (see page 87) and then rotating the polarization vectors with the appropriate combination of half wave plates. In fact, rotating the beam rather than the second crystal negates the effect on the transverse displacement of the centre of the beam that conical diffraction by a rotating second crystal would have (Figure A1 in the appendix shows displacement in the transverse plane).)

The Fourier transform of the conically diffracted field after being rotated by angle α is given by

$$e^{-\frac{1}{2}ikP^2Z}\left[\cos(kPR_1)\,\boldsymbol{R}(\alpha) - i\sin(kPR_1)\boldsymbol{M}(\varphi)\right]a(P)\begin{pmatrix}e_x\\e_y\end{pmatrix} \qquad 3.2.27.$$

where we have presumed the beam incident on the first crystal is circularly symmetric and uniformly polarized. We have written the geometric ring radius associated with the first crystal as R_1. Now if this beam is propagated through a second biaxial crystal with geometric ring radius R_2 then the Fourier transform of the field after conical diffraction by the 2nd crystal is given by:

$$\begin{aligned} e^{-\frac{1}{2}ikP^2\mathrm{Z}}\left[\cos(kPR_2)\,\boldsymbol{I} - i\sin(kPR_2)\boldsymbol{M}(\varphi)\right] \times \left[\cos(kPR_1)\,\boldsymbol{R}(\alpha)\right. \\ \left. - i\sin(kPR_1)\boldsymbol{M}(\varphi)\right]a(P)\begin{pmatrix}e_x\\e_y\end{pmatrix}, \end{aligned} \qquad 3.2.28.$$

where $\mathrm{Z} = l_1 + l_2 + n_2(z - (l_1 + l_2))$. Multiplying this out leads to

$$\begin{aligned} e^{-\frac{1}{2}ikP^2\mathrm{Z}}\left\{\left[\frac{1}{2}\left(\cos\left(kP(R_2 - R_1)\right) + \cos\left(kP(R_2 + R_1)\right)\right)\right]\boldsymbol{R}(\alpha)\right. \\ - \left[\frac{i}{2}\left(\sin\left(kP(R_2 + R_1)\right)\right.\right. \\ \left.\left. - \sin\left(kP(R_2 - R_1)\right)\right)\right]\boldsymbol{M}(\varphi_P) \\ - \left[\frac{i}{2}\left(\sin\left(kP(R_2 + R_1)\right)\right.\right. \\ \left.\left. + \sin\left(kP(R_2 - R_1)\right)\right)\right]\boldsymbol{M}(\varphi_P - \alpha) \\ + \left[\frac{1}{2}\left(\cos\left(kP(R_2 + R_1)\right)\right.\right. \\ \left.\left. - \cos\left(kP(R_2 - R_1)\right)\right)\right]\boldsymbol{I} \times a(P)\begin{pmatrix}e_x\\e_y\end{pmatrix}\Bigg\} \end{aligned} \qquad 3.2.29.$$

The final expression for the field in real space beyond the second crystal is obtained by taking the Fourier transform of 3.2.29 using

$$\int_0^{2\pi} d\theta e^{ikr\cos(\varphi-\theta)} = 2\pi J_0(kr) \qquad 3.2.30.$$

and

$$\int_0^{2\pi} d\theta e^{ikr\cos(\varphi-\theta)}\cos(\theta) = 2\pi J_1(kr)\cos(\varphi), \qquad 3.2.31.$$

and then performing the rotation described by equations 3.2.23 – 3.2.25 in the opposite sense.

In the simple but important case of cascade conical diffraction by two crystals of equal length we set $R_1 = R_2 \equiv R_0$ then the formula for the emergent field in direction space reduces to

$$\begin{aligned} e^{-\frac{1}{2}ikP^2Z}\Big\{&\left[\frac{1}{2}(1+\cos(2kPR_0))\right]\boldsymbol{I} - \left[\frac{i}{2}(\sin(2kPR_0))\right]\boldsymbol{M}(\varphi_P) \\ &- \left[\frac{i}{2}(\sin(2kPR_0))\right]\boldsymbol{M}(\varphi_P-\alpha) \\ &+ \left[\frac{1}{2}(-1+\cos(2kPR_0))\right]\boldsymbol{R}(-\alpha)\times a(P)\begin{pmatrix}e_x\\e_y\end{pmatrix}\Big\}. \end{aligned} \qquad 3.2.32.$$

In position space we can write this field as the sum of six components as follows :

$$\begin{aligned} \vec{E}(r,\varphi,Z) = \Big(&G(-\boldsymbol{R}(-\alpha)+\boldsymbol{I}) + B_{02}(\boldsymbol{R}(-\alpha)+\boldsymbol{I}) + \\ &B_{12}(\boldsymbol{M}(\varphi)+\boldsymbol{M}(\varphi-\alpha))\Big)\begin{pmatrix}e_x\\e_y\end{pmatrix}, \end{aligned} \qquad 3.2.33.$$

where

$$B_{02} \equiv {}^1/_2\, B_0(2R_0, Z) \qquad 3.2.34.$$

$$B_{12} \equiv {}^1/_2\, B_1(2R_0, Z) \qquad 3.2.35.$$

$$G = {}^k/_2 \int_0^\infty Pa(P)e^{-\frac{1}{2}ikP^2Z}J_0(kPr)dP. \qquad 3.2.36.$$

It is interesting to consider how the polarization vectors of the three components combine to form the focal image plane polarization pattern of the cascade conically diffracted beam. We expect the ring plane formed by a cascade of two crystals to have the polarization pattern associated with the orientation of the second crystal and this turns out to be the case. For left circular incident polarization (i.e. a left circularly polarized Gaussian is incident on the first crystal), we can re-write equation 3.2.33 as

$$\vec{E}(r,\varphi,\mathrm{Z}) = (\mathrm{G}+\mathrm{B}_{02})\begin{pmatrix}1\\ i\end{pmatrix} + e^{i\alpha}(-\mathrm{G}+\mathrm{B}_{02})\begin{pmatrix}1\\ i\end{pmatrix} + (\mathrm{B}_{12}e^{i\phi} + e^{i(\phi+\alpha)}\mathrm{B}_{12})\begin{pmatrix}1\\ -i\end{pmatrix} \qquad 3.2.37.$$

This describes a superposition of beams with opposite circular polarizations. The effect of the rotation matrix, $\boldsymbol{R}(-\alpha)$, is just a change of phase for circularly polarized light. The component with the same sense of circular polarization as the incident beam is a superposition of a beam with a B_0 profile and a beam with the profile of the incident beam, G. The component that is circularly polarized in the opposite sense as the incident beam has the familiar B_1 profile.

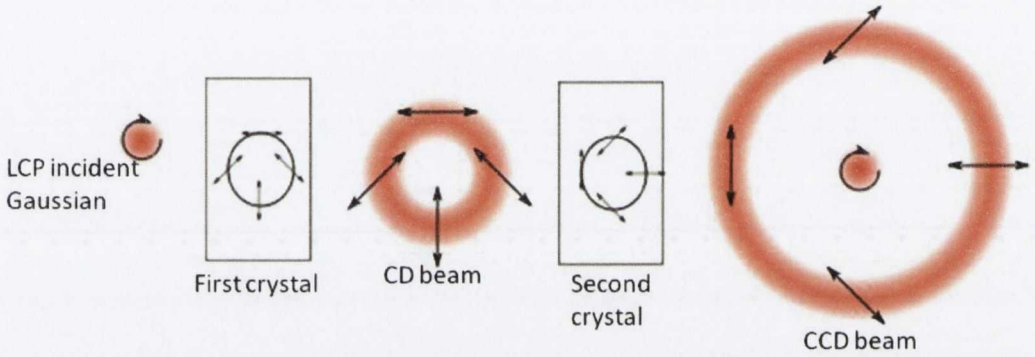

Figure 3.2.6: Schematic representation of the polarization of the cascade conically diffracted Gaussian in the FIP relative to the once conically diffracted Gaussian and the beam incident on the first crystal. The relative rotation is 90° in this diagram.

It is notable that the two terms describing the incident beam in equation 3.2.37 have opposite signs. This makes it immediately obvious that this term vanishes for α=0 and has maximum magnitude for the case of α=π. Also in the case of α=π the B_{02} & B_{12} terms vanish and we are left with the original beam. In the intermediate cases the intensity of the component with the profile of the incident beam grows (in the focal image plane where there is negligible interference between the rings and the central beam for well developed rings) according to

$$I_G(\alpha) = {}^1/_2\,(1-\cos\alpha)I_0, \qquad 3.2.38.$$

where I_0 is the maximum intensity of the incident Gaussian beam. Figure 3.2.7 shows the simulation of the intensity profiles of a Gaussian beam that has propagated through a cascade of two identical crystals for a range of values of α.

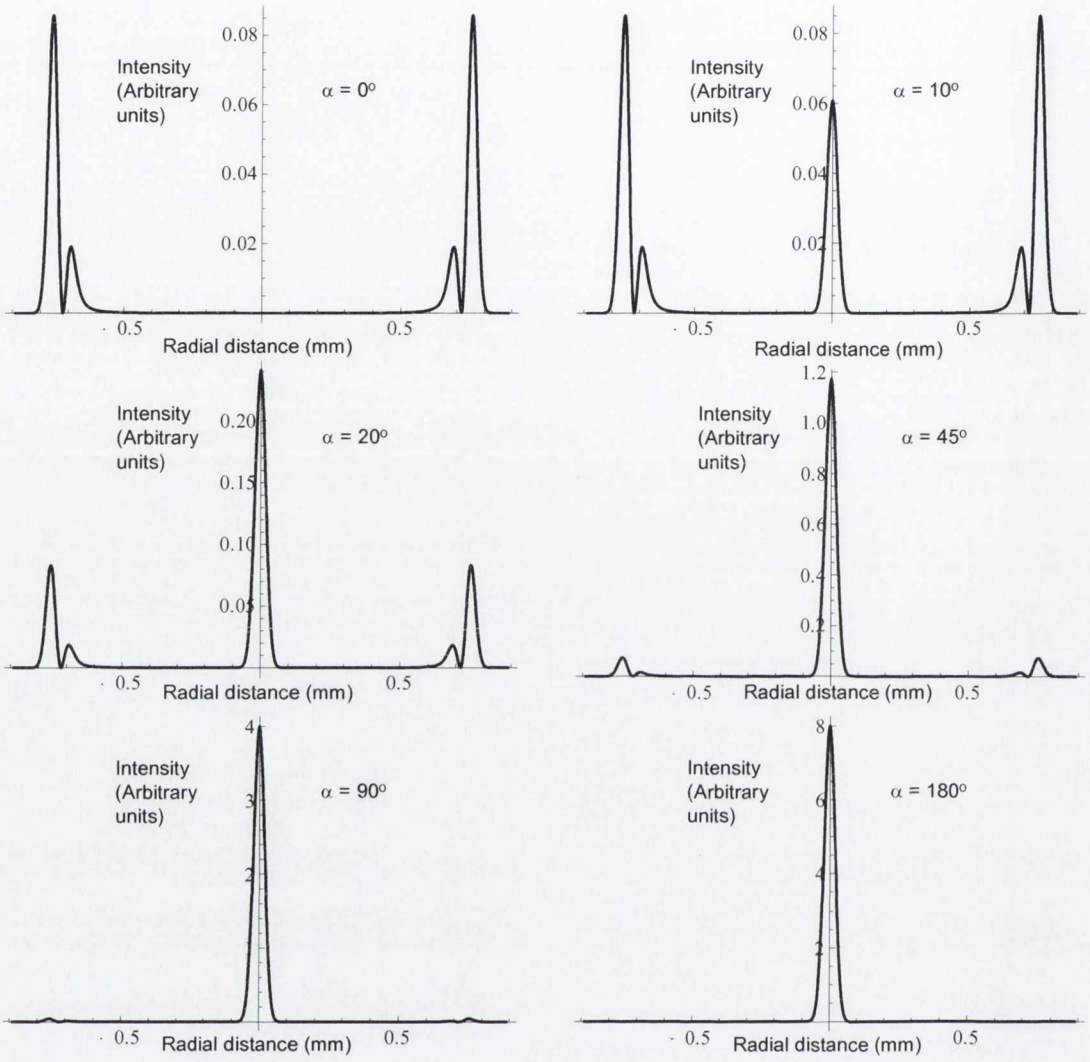

Figure 3.2.7: Radial intensity plots of the focal image plane profile of a Gaussian beam with 40 μm waist after propagation through a cascade of two identical biaxial crystals with R_0=0.37mm. The relative rotations (α) between the crystals are indicated in the plots.

The transfer of energy from the ring profile to the Gaussian profile has an interesting consequence. The conically diffracted beam contains orbital angular momentum of ½ħ per photon for the case of well defined rings (Berry, Jeffrey, & Mansuripur, 2005). If we gradually transform the ring profile into a Gaussian profile that is circularly polarized we are continuously transforming a beam with ½ħ OAM per photon into a beam with ħ SAM per photon.

The diffraction of the focal image plane profiles of the form shown in Figure 3.2.7 have some interesting features resulting from interference between the diverging Gaussian and converging inner ring. The intensity distribution in the {*r*, *z*} plane of a beam emerging from a cascade of two identical crystals with a relative rotation of 20° is shown in Figure 3.2.8. In this figure, the beam evolves from the FIP (*Z* = 0) to a distance of 20 cm from the FIP where the far

field profile has formed. The interference between the inner ring and Gaussian beams causes a series of intensity maxima and minima to occur along the propagation axis of the beam. The axial intensity profile of this beam is plotted in Figure 3.2.9, where it is compared with the axial profile of a beam emerging from the same cascade with $\alpha = 40^{\circ}$. The relative positions of these maxima and minima are determined by the phase difference between the ring and the spot which depend only on the diameter of the ring and the wavelength of the light.

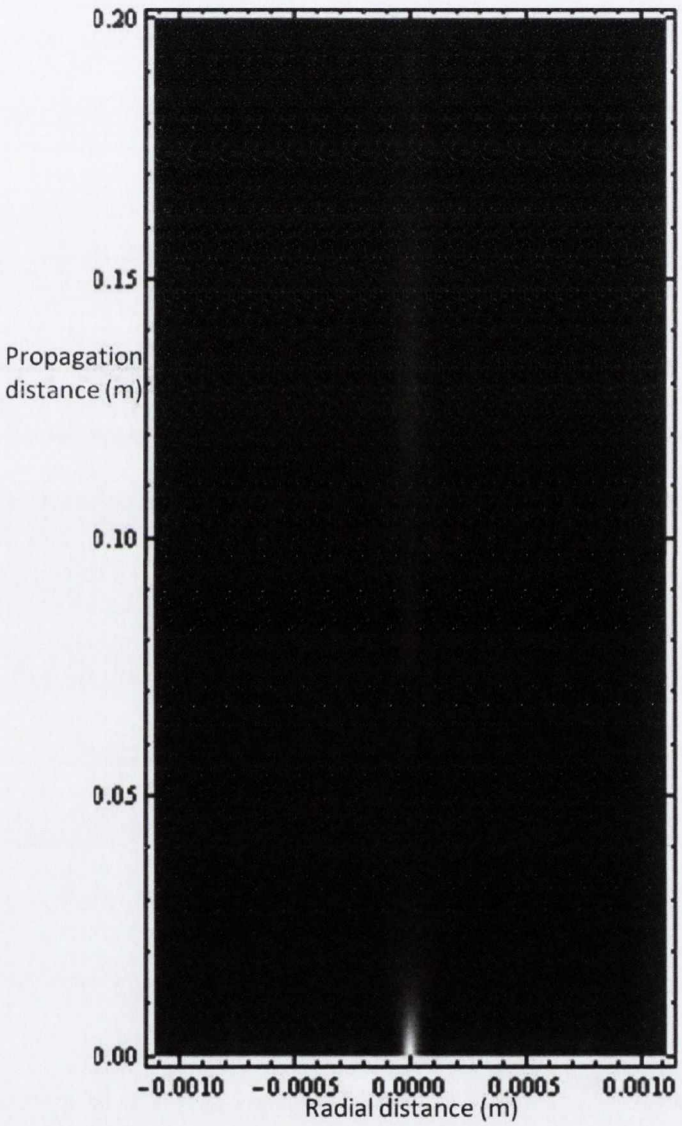

Figure 3.2.8: A simulation of the evolution of a Gaussian beam with a 50 μm waist after propagation through a cascade of two identical biaxial crystals with a relative rotation of 20°. The propagation distance is measured from the FIP.

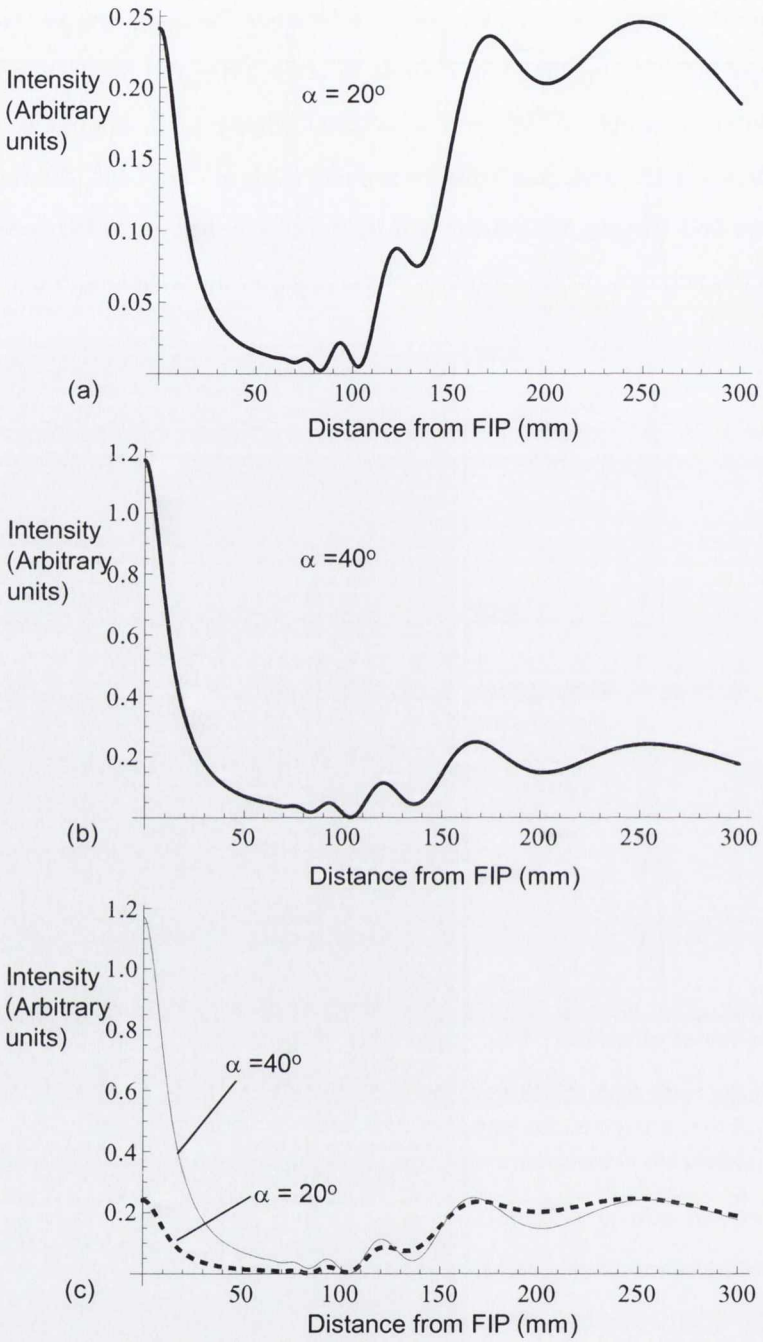

Figure 3.2.9: The on axis intensity profiles of a Gaussian with waist of 50μm after propagation through a cascade of two biaxial crystals with relative rotations of 20° (a) and 45° (b). (c) shows the data from (a) and (b) plotted on the same graph. The decay of the central Gaussian followed by interference between the Gaussian and converging ring can be seen for both values of α.

Examining equation 3.2.33 tells us that the cascade conically diffracted beam is a superposition of beams with orthogonal circular polarizations. The beam that is polarized orthogonally to the incident beam has the profile of a B_1 beam and the other component has B_0 profile centred on the profile of the incident beam (a Gaussian in our simulations (and experiments)). The

intensity distribution in the {r, z} plane of the components of the beam in Figure 3.2.8 are plotted in Figure 3.2.10.

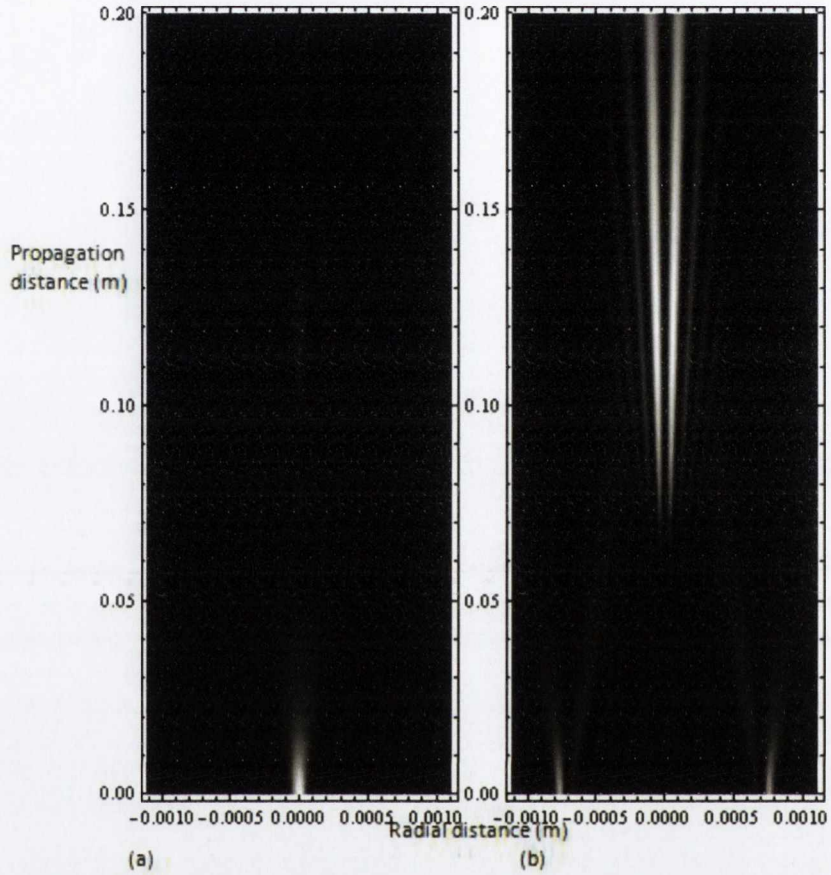

Figure 3.2.10: The evolution from the FIP to far field (20 cm from the FIP) of the two circularly polarized components of the beam in Figure 3.2.8 above. The component with the same circular polarization (a) as the incident component is a B_0 beam centred on a beam with the profile of the incident Gaussian while the profile of the other component (b) has the profile of a B_1 beam

If we increase the waist of the Gaussian incident on the first crystal we expect to see a broadening of both the rings as well as the central Gaussian of the emergent beam. Figures 3.2.11 and 3.2.12 confirm this. In Figure 3.2.12 we see alternating intensity maxima and minima on axis at specific propagation distances as we increase the incident beam waist. This is due to the fact that the central Gaussian is more strongly divergent and the inner ring is more strongly convergent for smaller beam waists and the on-axis interference pattern shown in Figure 3.2.9 is alternately squeezed and stretched for smaller and bigger waists respectively.

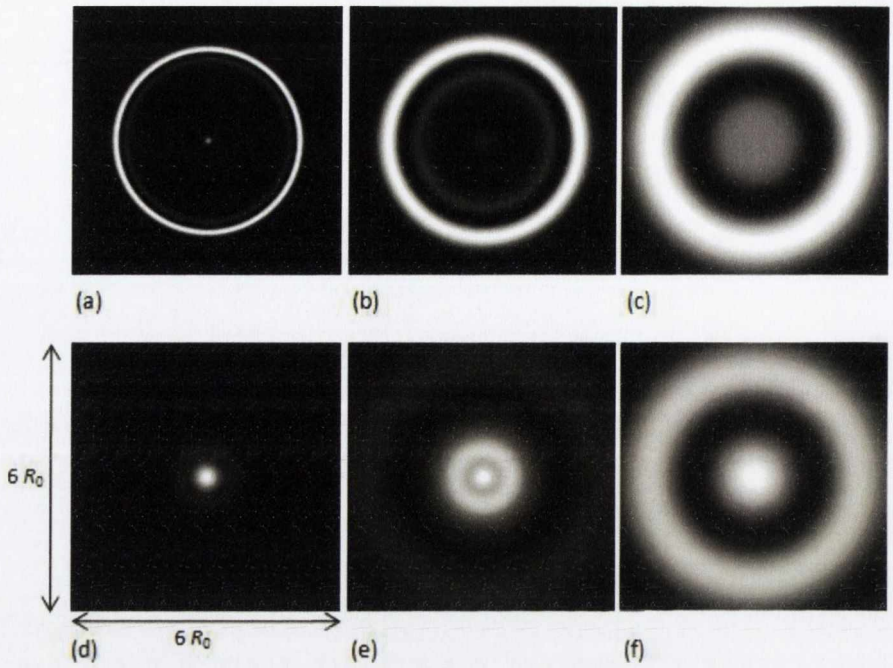

Figure 3.2.11: Simulations of the focal image plane profile for input Gaussian beams with waists of (a) 50 μm, (b) 150 μm and (c) 0.34 mm (=R_0) after propagation through a cascade of two identical biaxial crystals with geometrical ring radii of 0.34 mm with a relative rotation of 10°. Images (d), (e) and (f) show the far field profiles (Z = 0.4 or 19.5 cm from the FIP) of the FIP profiles in (a), (b) and (c) respectively.

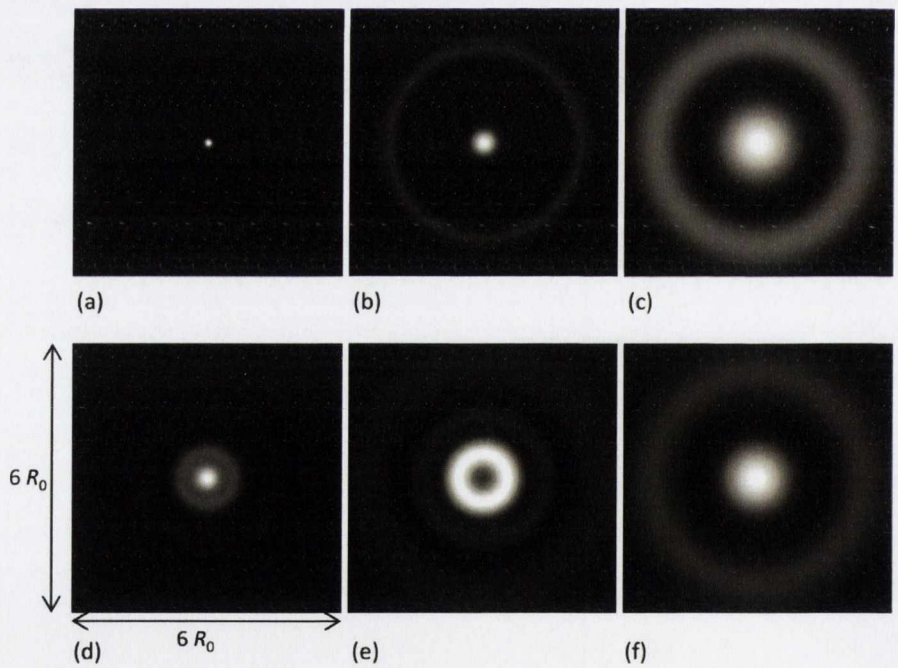

Figure 3.2.12: Simulations of the focal image plane profile for input Gaussian beams with waists of (a) 50 μm, (b) 150 μm and (c) 0.34 mm (=R_0) after propagation through a cascade of two identical biaxial crystals with geometrical ring radii of 0.34mm with a relative rotation of 45° between the crystals. Images (d), (e) and (f) show the far field profiles (Z = 0.4 or 19.5 cm from the FIP) of the FIP profiles in (a), (b) and (c) respectively.

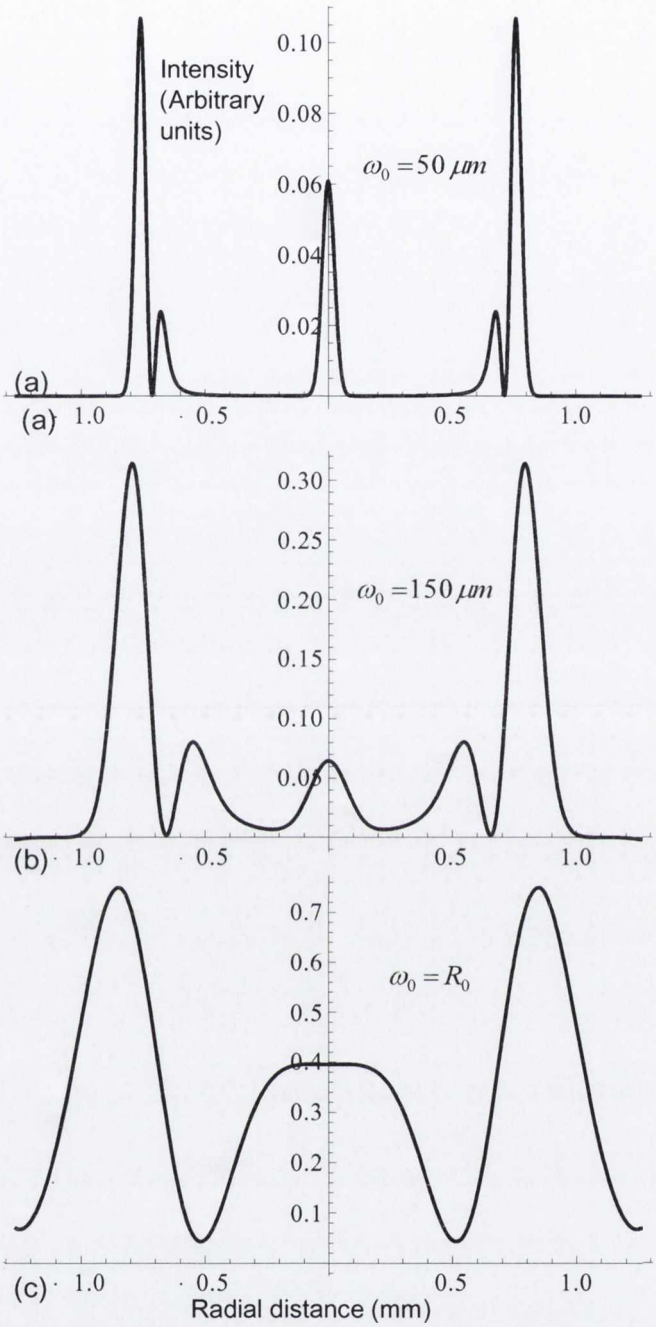

Figure 3.2.13: Linear intensity plots corresponding to the 2D FIP intensity plots of Figure 3.2.11.

If we do not make the assumption that our two crystals have equal geometric ring radii, the solution can be neatly expressed as

$$\vec{E}(\vec{r}, Z) = \Big([(-\mathrm{B}_0(R_1 - R_2) + \mathrm{B}_0(R_1 + R_2)]\boldsymbol{R}(-\alpha) + [(\mathrm{B}_0(R_1 - R_2) + \mathrm{B}_0(R_1 + R_2)](\boldsymbol{I}) + [\mathrm{B}_1(R_1 - R_2) + \mathrm{B}_1(R_1 + R_2)] \times \big(\boldsymbol{M}(\varphi) + \boldsymbol{M}(\varphi - \alpha)\big)\Big) \begin{pmatrix} e_x \\ e_y \end{pmatrix}. \qquad 3.2.39.$$

This equation obviously predicts a focal image plane profile of two sets of double rings with dark ring radii given by the sum and difference of the geometric ring radii associated with each of the two crystals in the cascade just like our intuitive picture of section 3.1 suggested. As in the case of the two crystals of equal length we see a transfer of power from the outer to the inner profile as the rotation between the crystals is increased from 0° to 180°. Figure 3.2.14 illustrates this. Figure 3.2.15 shows the variation of the focal image plane profile with beam waist. The result shows the expected uniform broadening of each ring profile.

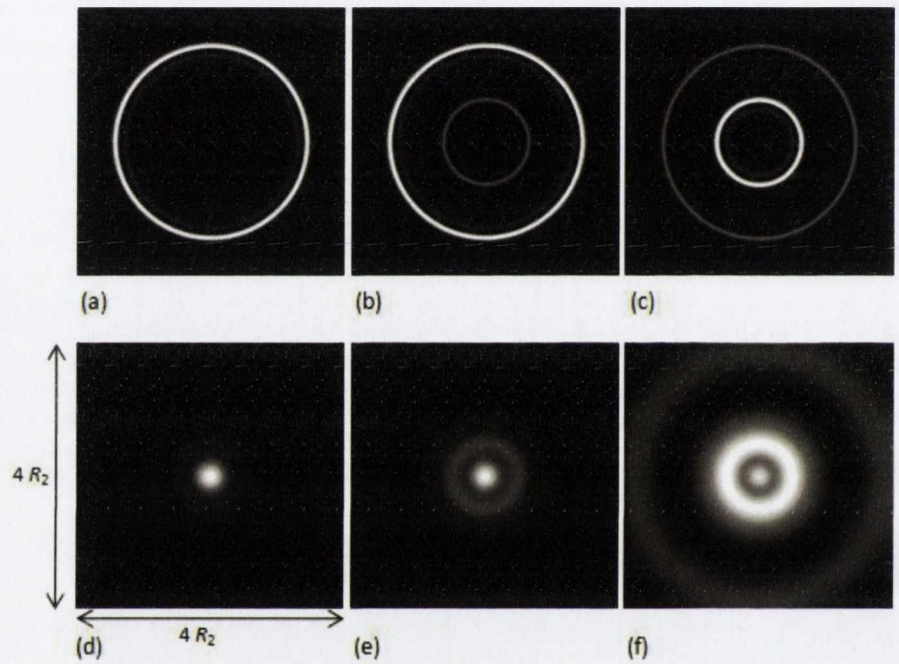

Figure 3.2.14 Focal image plane profiles for a cascade of two biaxial crystals with R_1 =0.3 mm and R_2 = 0.5 mm. The waist of the incident Gaussian was 40 μm. The angles of rotation between the crystals were (a) 0°, (b)45° and (c) 90°. Parts (d), (e) and (f) show the far field (Z = 0.4 or 19.5 cm from the FIP) profiles corresponding to the FIP profiles in parts (a), (b) and (c) respectively.

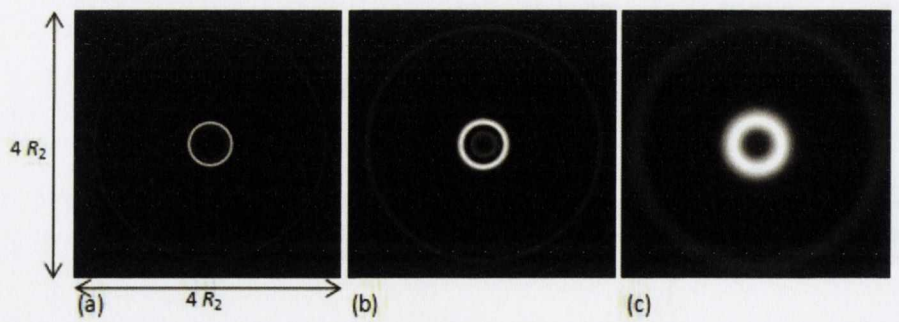

Figure 3.2.15: Focal image plane profiles for a cascade of two biaxial crystals with a relative rotation of 45°. The waist of the incident Gaussian for each simulation was (a) 20 μm, (b) 50 μm and (c) 150 μm. The geometric ring radii of the crystals were R_1=0.37 mm and R_2=0.53 mm.

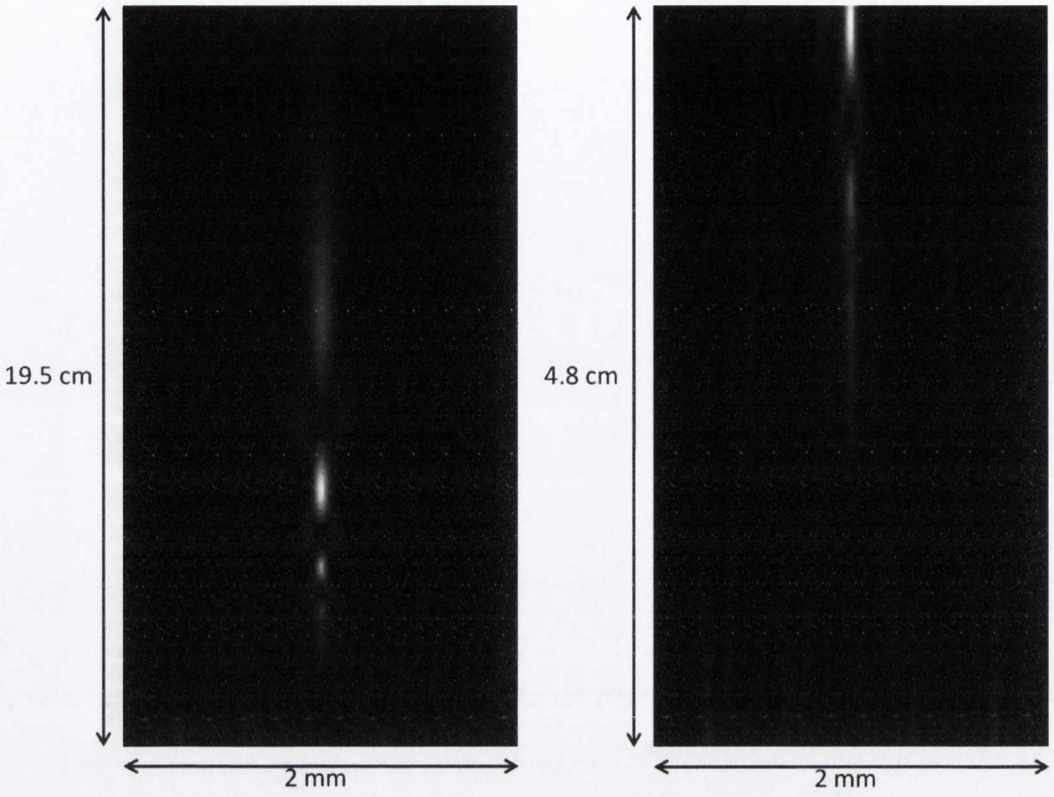

Figure 3.2.16: The evolution from the FIP to the far field of a Gaussian with a 40 μm waist after propagation through a cascade of two crystals with geometric ring radii of 0.3 and 0.5 mm. The relative rotation between the crystals was 60°.

Figure 3.2.16 shows the intensity of the cascade conically diffracted beam in the {*r*, *Z*} plane. The occurrence of axial intensity maxima and minima is notable and is due to the interference between waves arriving on axis from the outer double ring and those arriving from the inner ring.

Equation 3.2.39 also predicts an effect that we mentioned in the previous section regarding the order of the crystals in a two crystal cascade. The polarization of the focal image plane profile results from the superposition of the orthogonal polarization profiles of the B_0 and B_1 components. Looking at equation 3.2.39 we see that the sign of the term $B_1(R_2 - R_1)$ is positive if we take $R_2 > R_1$ and negative if $R_2 < R_1$since B_1 is an odd function of the geometric ring radius. The effect of this sign change on the polarization of the focal image plane profile is shown in Figure 3.2.17. Figure 3.2.18 shows the following consequence of this effect: Linearly polarized incident light will be transformed into concentric crescents with their maxima at the same angular position for $R_2<R_1$ and at diametrically opposite positions for $R_2>R_1$.

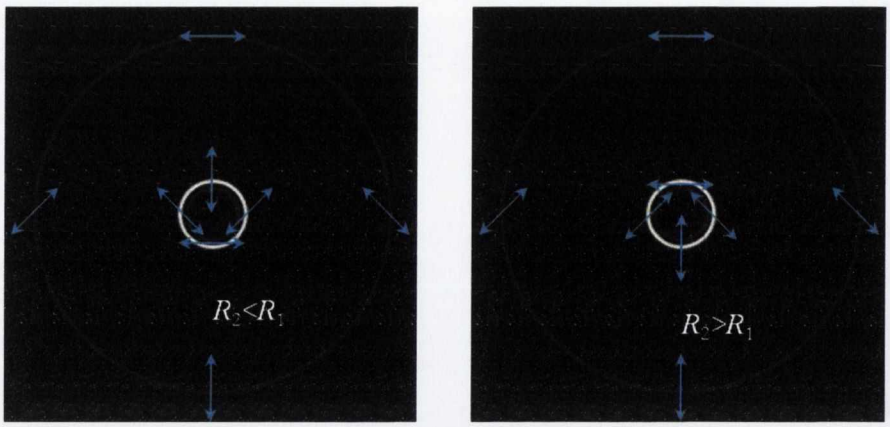

Figure 3.2.17: The Focal image plane polarization profile for a cascade of two biaxial crystals. The polarization of the inner ring is orthogonal to that of the outer ring for $R_2 < R_1$ and aligned with it when$R_2 > R_1$. If we have $R_2 = R_1$ then the polarization of the central spot is circular.

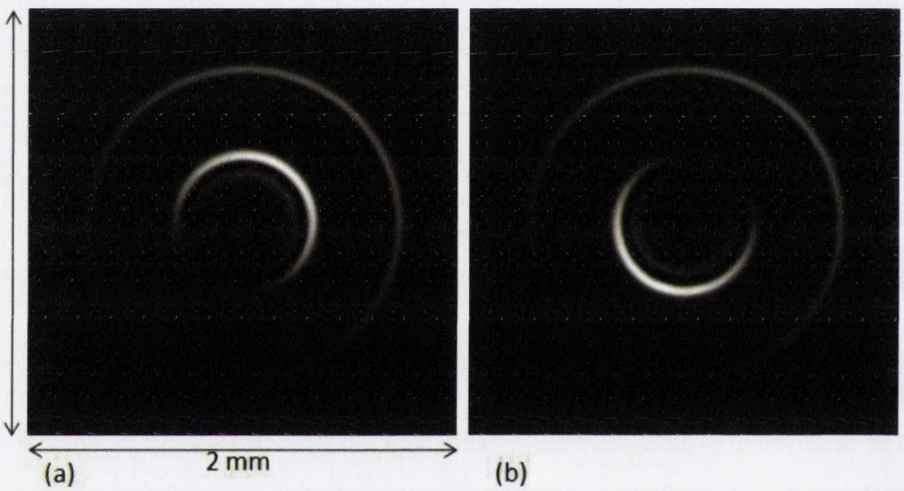

Figure 3.2.18: The focal image plane intensity profiles for the case of a 50 μm waist linearly polarized Gaussian after propagation through a cascade of two biaxial crystals with geometric ring radii of 0.5 mm and 0.2 mm. (a) The Gaussian propagates through the 0.5 mm radius crystal first. (b) The Gaussian propagates through the 0.2 mm radius crystal first.

3.3. Cascade conical diffraction: Theory versus experiment

In this section we compare some of the predictions of paraxial cascade conical diffraction theory developed in the previous section with experiment. Each experiment involved the transformation of an incident Gaussian beam by an optical system involving two biaxial crystals along with wave plates and lenses. In part (a) theory is compared with experiment for the case of two identical crystals with a relative rotation about their optic axis. In part (b) some of the predictions of cascade conical diffraction for the case of two biaxial crystals with different lengths are tested experimentally.

A: Identical crystals:

The experimental setup used to test the predictions of cascade conical diffraction for the case of two identical crystals is shown in Figure 3.3.1.

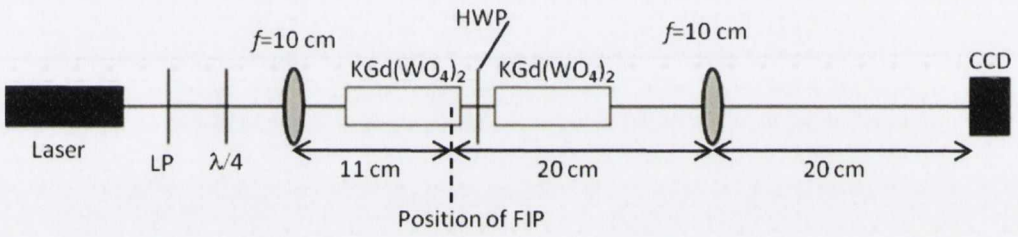

Figure 3.3.1: The experimental setup used to observe the FIP profiles. The half wave plate between the crystals was removed for the measurements

The biaxial crystals used were slabs of $KGd(WO_4)_2$ obtained from *CROptics* [www.croptics.eu] with dimensions of 4 x 3 x 21.1 mm and 4 x 3 x 20.9 mm respectively. The principal refractive indices of the crystals were n_1=2.013, n_2=2.045, n_3=2.086. This implies that the cone in the crystal has a spreading angle of A = 0.0177 rad and the geometrical ring radii for the crystals are respectively R_{01}=0.37 mm & R_{02}=0.374 mm respectively. In our comparison of experiment with theory we have neglected this small discrepancy. The laser used was a 10 mW He-Ne. The beam was focused to a 45 μm waist by a 10 cm focal length lens. The focal image plane, where the ring profile is at its sharpest, was imaged onto a CCD one to one with a 10 cm lens.

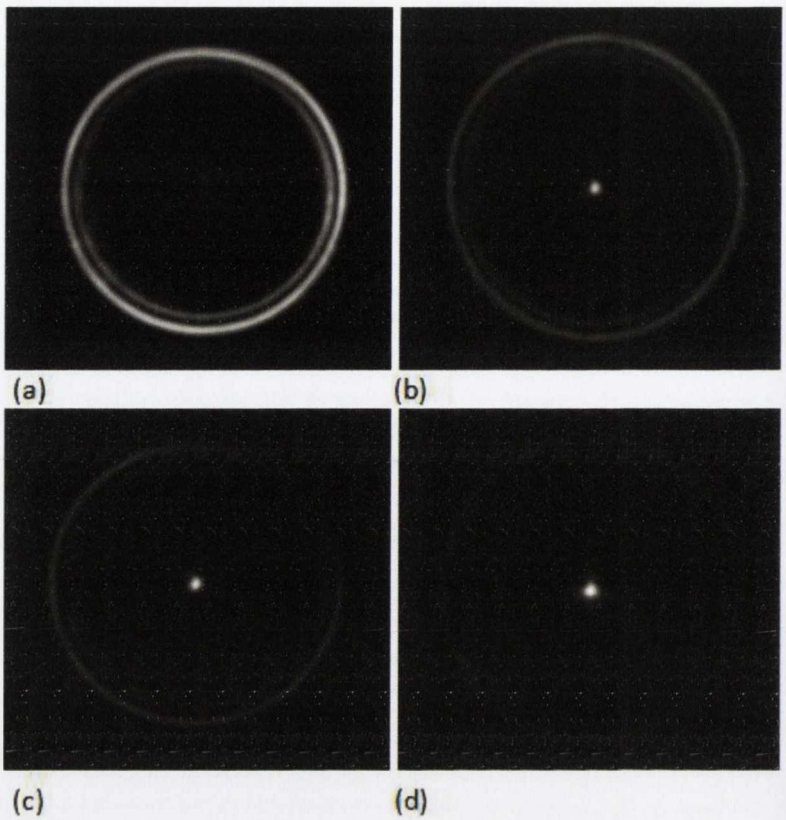

Figure 3.3.2: CCD images of the FIP obtained using the experimental setup in Figure 3.2.1. The relative rotations between the crystals were (a) $\alpha = 0^{\circ}$, (b) $\alpha = 15^{\circ}$, (c) $\alpha = 45^{\circ}$, and (d) $\alpha = 90^{\circ}$. The images show the expected growth in intensity of the central spot and weakening of the rings as α is increased.

Figure 3.3.2 shows CCD images of the FIP profile for a range of values of α. These images were taken using the setup shown in Figure 3.3.1 with the half wave plate removed. The transition from double ring beam to Gaussian can clearly be seen. (The images in Figure 3.3.1 are centred on the centre of the ring profile. However, the position of the centre of the ring profile itself is translated in a circular path as the second crystal is rotated. This translation of the beam is demonstrated in Figure B.1 in the Appendix B). Figures 3.3.3 shows comparisons of the theoretical radial intensity profile with the experimental data for the cases of $\alpha=45^{\circ}$and $\alpha=15^{\circ}$. The radial profiles were taken across azimuthally averaged versions of the images in Figure 3.3.2. The azimuthal averaging was done to an image by superimposing four versions of that image. The four versions were generated from the original by rotating it in steps of 90° about its centre (the centre of the ring profile). The smoothed ring images are attached in Appendix B (Figure B. 2).

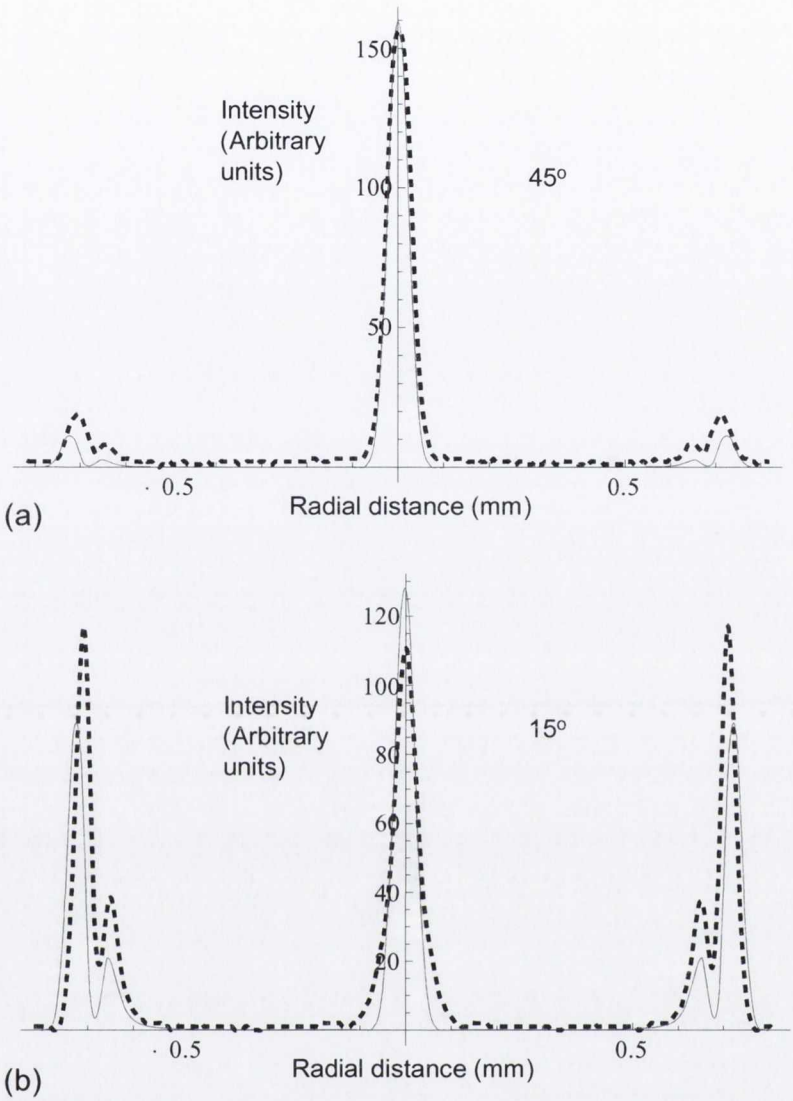

Figure 3.3.3: (a) Experiment (dashed line) versus theory for the case of α=45°. (b)Experiment versus theory with α=45°. The agreement is less accurate for small α since the peak intensity of the central spot grows rapidly relative to the peak intensity of the outer ring as α increases from 0°.

In the previous section it was predicted that the intensity spot on which the double ring profile is centred (Figure 3.2.7) should have a Gaussian intensity profile with the same minimum waist as the incident Gaussian and, furthermore, introducing a relative rotation of 180° between the crystals would transform the cascade conically diffracted beam back into the incident Gaussian (taking into account spreading due to propagation). Figure 3.3.4 (a) shows a comparison of the central spot profiles of the cascade conically diffracted beam for $\alpha = \pi$ with the profile of the incident Gaussian. Figure 3.3.4 (b) shows a comparison of the incident Gaussian with the cascade conically diffracted beam with $\alpha = \pi$.

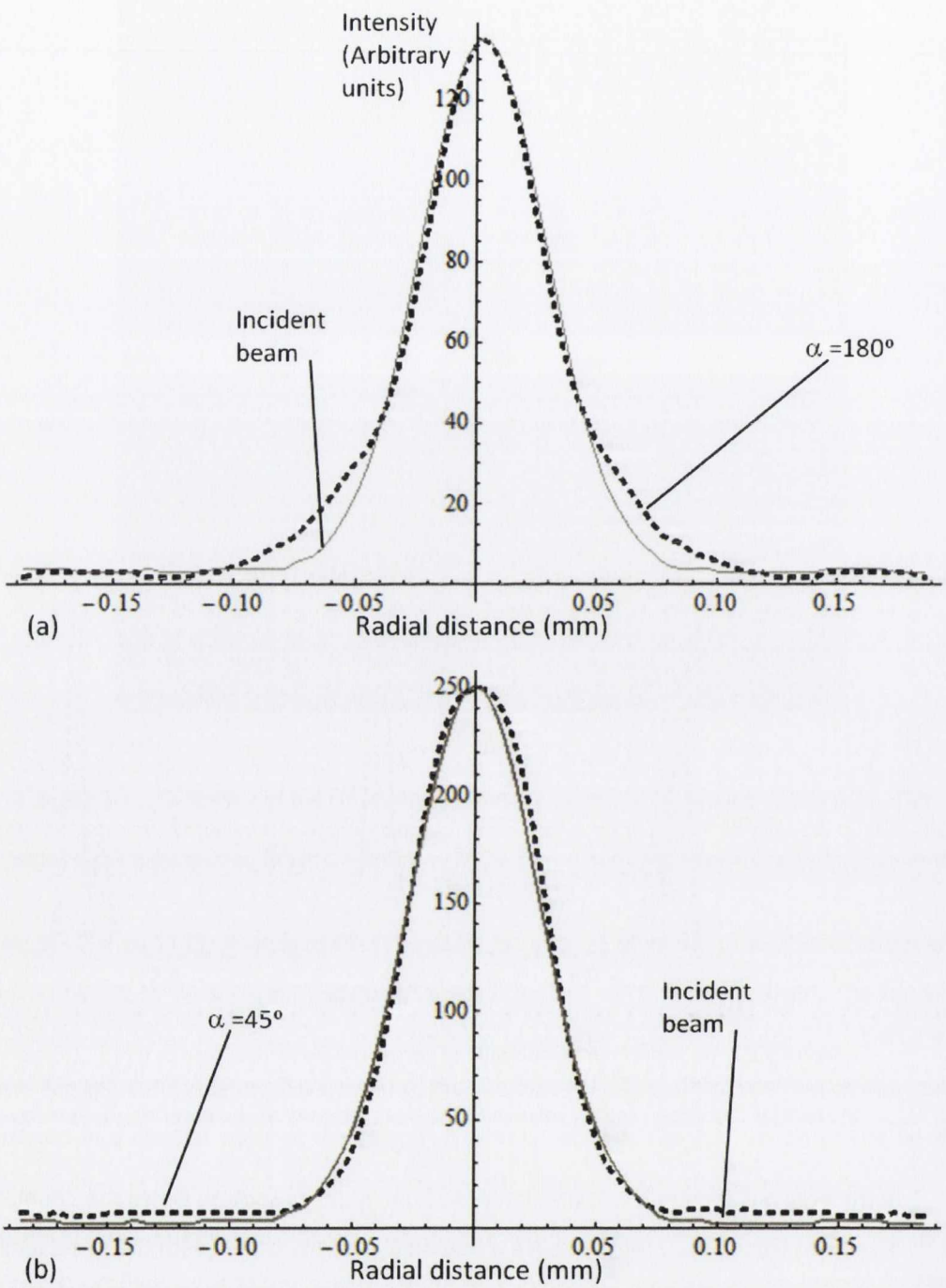

Figure 3.3.4: (a) The incident Gaussian (grey line) plotted alongside the central intensity spot of the cascade conically diffracted beam with $\alpha=180^{\circ}$ (dashed black line). (b) The same incident Gaussian (grey line) plotted alongside the central spot of the cascade beam generated with $\alpha = 45^{\circ}$ (dashed line).

It was predicted in the previous section (Figure 3.2.4) that placing a half wave plate between a cascade of two identical biaxial crystals would introduce an azimuthal modulation into the intensity profiles of both the double ring and central spot profiles. These can be clearly seen in Figure 3.3.5 which shows the FIP profiles for a cascade with a relative rotation of 180° between the crystals and with the fast axis of the half wave plate at two different angles.

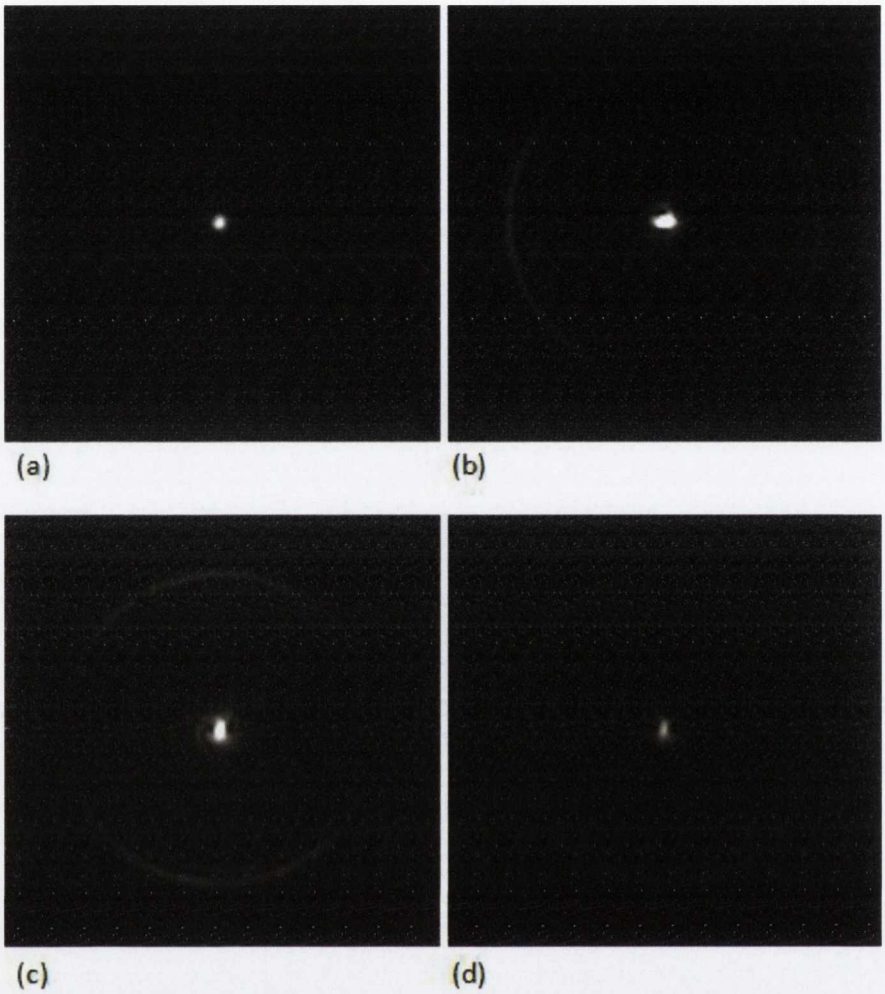

Figure 3.3.5: FIP profiles of the cascade CD beam with α=180°. (a) Without a wave plate between the crystals; (b) A half wave plate between the crystals with its fast axis aligned with the horizontal; (c) A half wave plate between the crystals with its fast axis at 45° to the horizontal; (d) The same image as (c) with the intensity lowered to make the central spot visible.

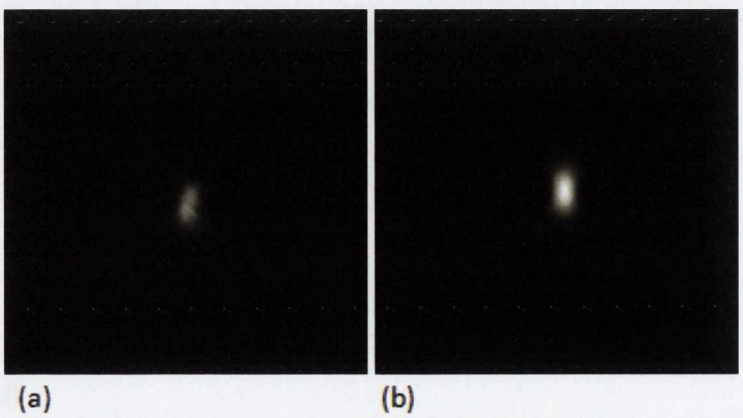

Figure 3.3.6: (a) A close up image of the central spot featured in Figure 3.2.5 (c). (b) The theoretical simulation of the same feature from the previous section. The close correspondence seems to confirm the explanation given in the previous section.

An alternative experimental setup without an imaging lens was used to examine the far-field intensity distributions of both components of the cascade conically diffracted beam. This optical arrangement is depicted in Figure 3.3.7.

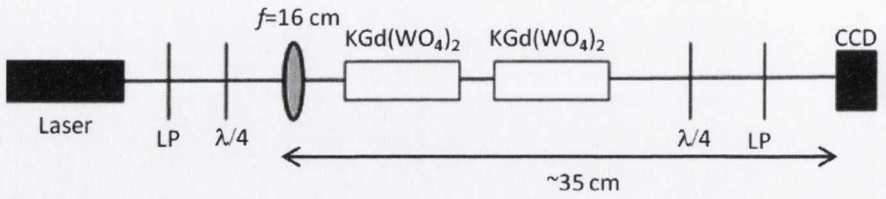

Figure 3.3.7: The optical arrangement used to record images of the far field intensity profiles. The circular analyser was used to separate the orthogonally polarized components.

In the previous section it was shown that, for the case of identical crystals, the emergent beam is a superposition of orthogonally circularly polarized component with one component having a B_1 profile and the other being a superposition of a B_0 beam with beam with the profile of the incident Gaussian (with the Z and R_0 parameters adjusted in each component to take account of the two crystals). Hence we expect the far field B_1 component to be a scaled version of its one crystal analogue and the other component to look like a modulated B_0 component that also has been scaled the same way. Figure 3.3.8 shows images of these components for the cases of one crystal (bottom row) and the case of two crystals with a relative rotation of 45° (top row). The images were taken at the same plane (indicated by the position of the CCD in Figure 3.3.7) at 17 cm from the position FIP with both crystals in place. The images in parts (a) and (b) of Figure 3.3.8 consist of systems of rings with ring thicknesses of approximately half of those in parts (c) and (d). The reason for this is that the diameter of the FIP ring profile that has converged to form the intensity profiles featured in parts (a) and (b) is twice that of the ring that has converged to form the intensity profiles in parts (c) and (d).

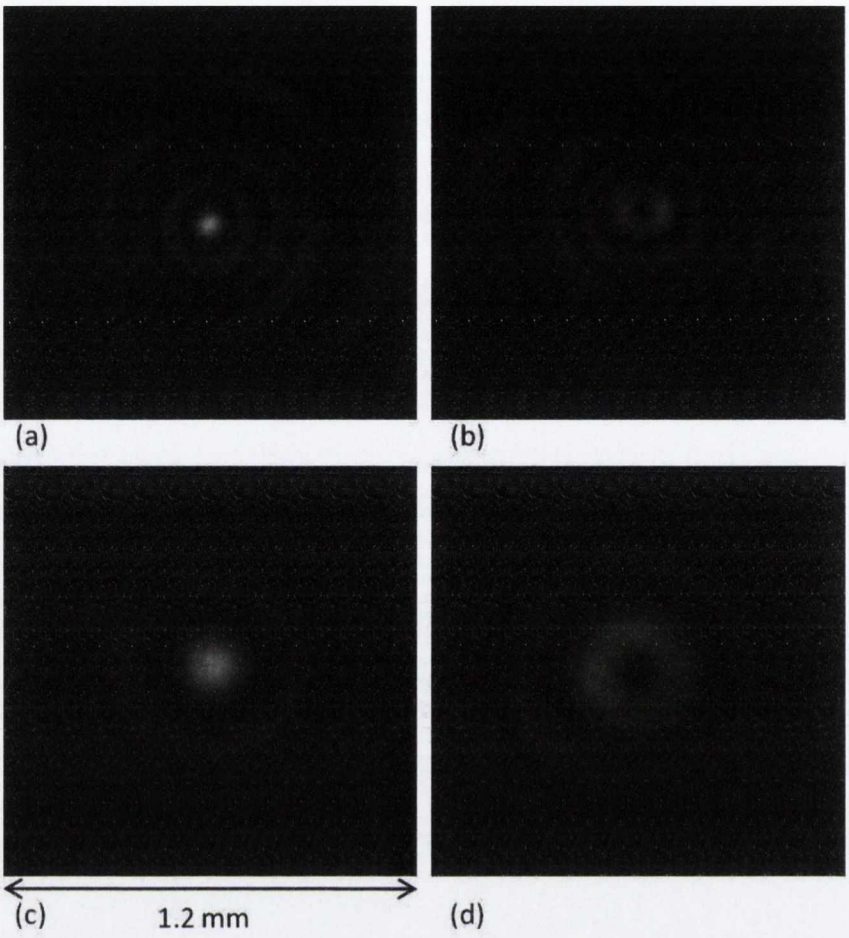

Figure 3.3.8: A comparison of the far field intensity profiles of the orthogonally polarized components of the cascade conically diffracted beam with those of the once conically diffracted beam. (a) The "B_{02} plus Gaussian" component of the cascade conically diffracted beam. (b) The B_{12} component of the cascade conically diffracted beam. (c) The B_0 component with the second crystal removed. (d) The B_1 component with the second crystal removed.

Figure 3.3.9 shows a comparison of the radial intensity distributions of the beams in Figure 3.3.8 (a) and (b) with theory. The radial intensity profiles used were smoothed versions of the profiles shown in Figure 3.3.8 (a) and (b). The images were smoothed by superimposing eight versions of the same image. The eight versions were generated by rotating the original image in steps of 45° about the point on the intensity distribution corresponding to the central propagation axis of the beam. The smoothed images are included in Appendix B (Figure B.4). It can be seen that the agreement of experiment with theory is better for the B_{12} than for the B_{02} component. This could be due to the fact that the evolution of the B_{02} involves interference between a beam with a B_0 like profile and a beam with the same shape as the incident Gaussian (see Figure 3.2.10).

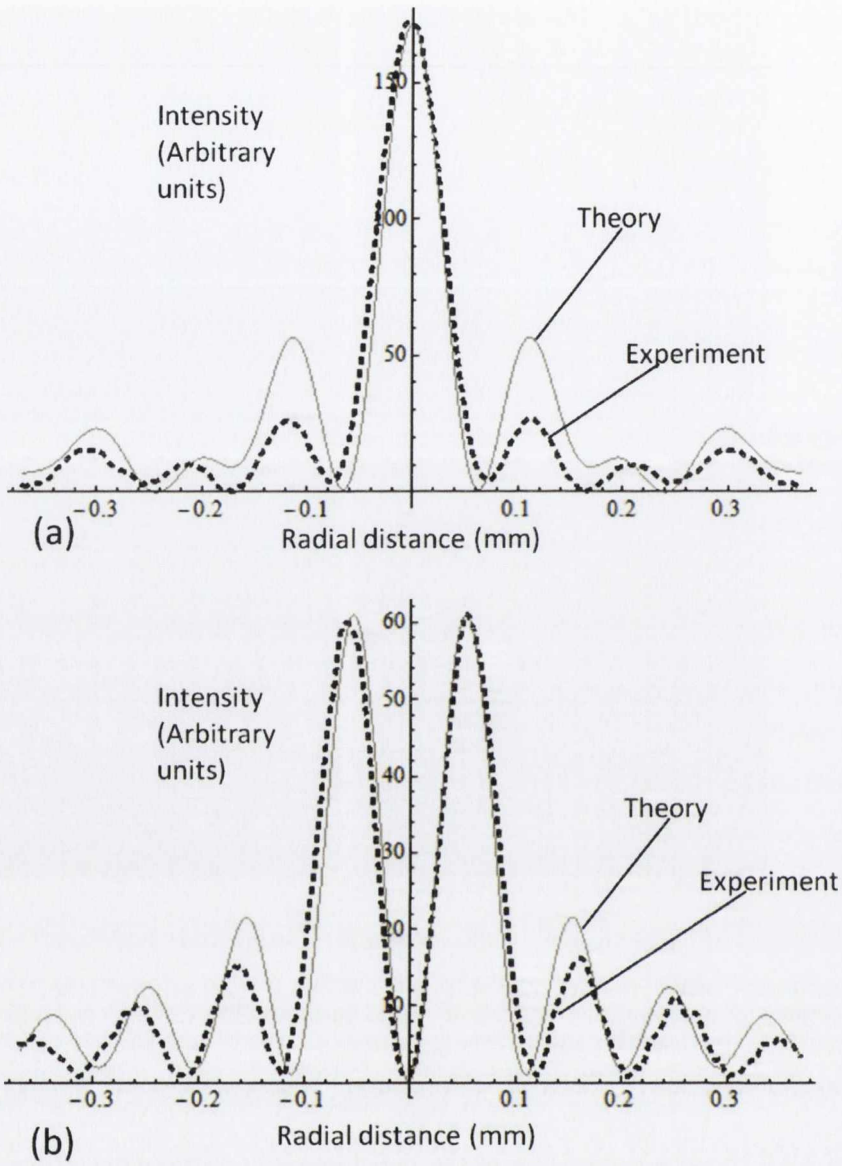

Figure 3.3.9: A comparison of the measured far field radial intensity distributions of the cascade conically diffracted Gaussian with theory. (a) The B_{02} plus Gaussian component. (b) The B_{12} component.

An interesting variation on the propagation of a Gaussian beam through a two crystal cascade with $\alpha = 180^{\circ}$ is to propagate a beam through the crystal and then reflect it back through the crystal in the opposite direction. This experiment was performed with the setup shown in Figure 3.3.10. The beam that was imaged at the CCD (with the quarter wave-plate removed in Figure 3.3.10) is shown in Figure 3.3.10. Though it displays an intensity profile that is dominated by an axial intensity spike, its Gaussian profile is difficult to observe due to a reflection from the crystal's entrance face. To ensure that conical diffraction did, in fact, occur twice, a quarter wave-plate was placed between the crystal and reflecting mirror. This converted the optical system into one that was analogous to a two crystal cascade with a half

wave-plate separating the crystals. Figure 3.3.11 (b) shows the intensity distribution recorded with the quarter wave-plate in position. It is the expected modulated ring profile centred on the position where the distorted Gaussian was located in the absence of the quarter wave-plate. This confirms the beam was conically diffracted as it propagated through the crystal along both directions.

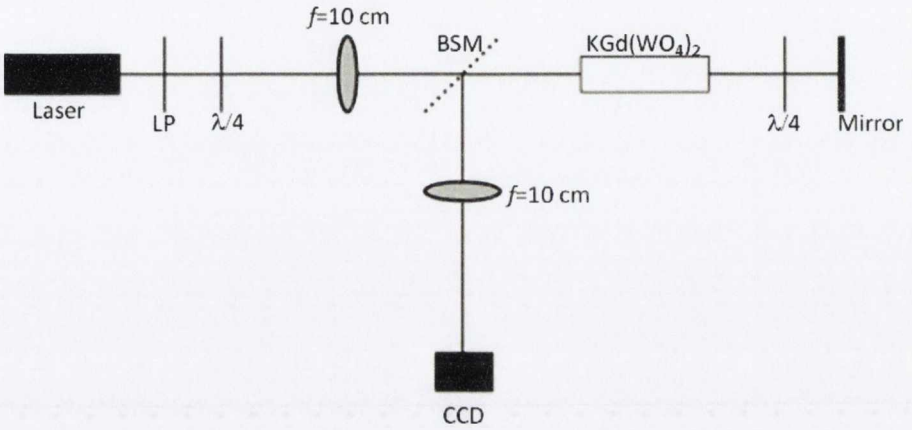

Figure 3.3.10: The experimental setup used to observe the beam that resulted from propagating a Gaussian along the optic axis of a biaxial crystal and then reflecting it back along the same direction. The quarter wave plate was inserted to further test the idea that propagation and reflection through the crystal is equivalent to propagation through a cascade of two identical crystals with a relative rotation of 180°.

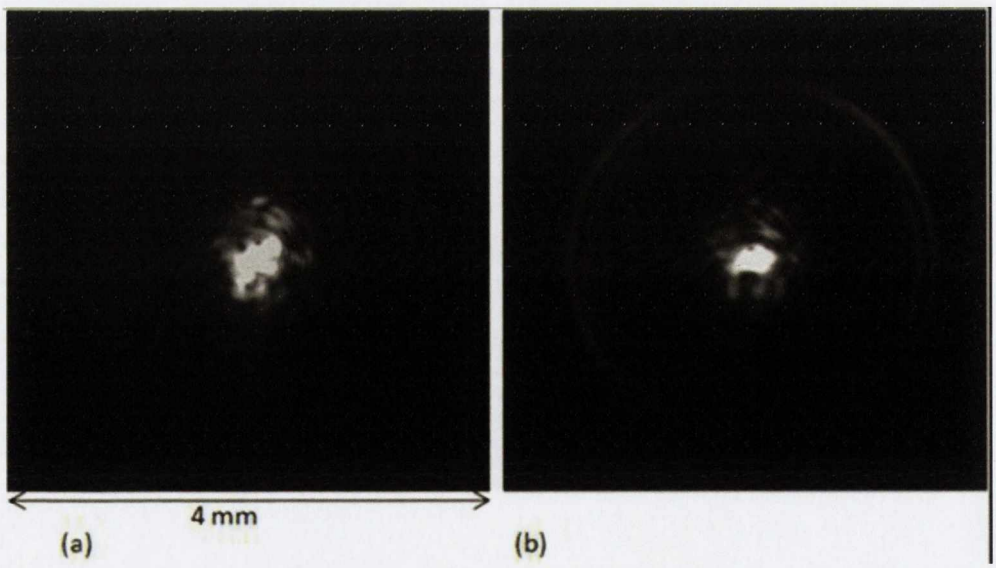

Figure 3.3.11: (a) The beam imaged at the CCD in Figure 3.3.10 with the quarter wave plate removed. The image is distorted due to a reflection from the entrance face of the crystal. (b) The beam imaged at the CCD in Figure 3.3.10 with the quarter wave plate inserted. This profile shows the characteristic features of the FIP profile of a cascade of two identical crystals with a half wave plate between them (Figure 3.3.5).

B: Unequal Crystals

In the previous section a number of interesting features were predicted for the case of conical diffraction by two crystals of unequal lengths. Several interesting features were observed in the laboratory using the basic setup shown in Figure 3.3.12. The crystals used had lengths of 30 mm and 20.9 mm. First we will note the appearance of a number of qualitative features of the focal image plane profile that were suggested in section 3.1 and derived from paraxial theory in section 3.2.

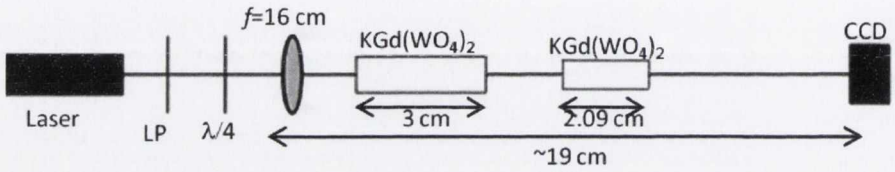

Figure 3.3.12: The optical arrangement used to observe the FIP profiles generated by the crystal arrangement shown in the diagram.

As expected, the circularly polarized incident Gaussian was transformed into a beam with a FIP profile consisting of double ring profiles with dark ring radii located at distances of $R_2 - R_1$ and $R_2 + R_1$ from the centre of the beam. This occurred regardless of whether the incident beam propagated through the smaller or larger crystal first. The polarization profile of the beam at the CCD did, however, change in the expected way (see Figure 3.2.13) when the order of the crystals was interchanged. Figure 3.3.13 (a) shows a CCD image of the FIP profile generated with the 3 cm crystal following the 2.09 cm one. Figure 3.3.13 (b) shows an image taken with the same arrangement but with a linear analyser transmitting vertically polarized light placed in front of the CCD. Figure 3.3.14 (a) and (b) shows images taken with the same optical arrangement as that used for Figure 3.3.13 but with the order of the crystals reversed (the relative rotation between the crystals for each image was 90°). The 180° rotation of the polarization profile of the inner double ring profile relative to that of the outer double ring profile for the case of the smaller crystal following the bigger one can be inferred from a comparison of Figure 3.3.13 (a) with Figure 3.3.14 (b).

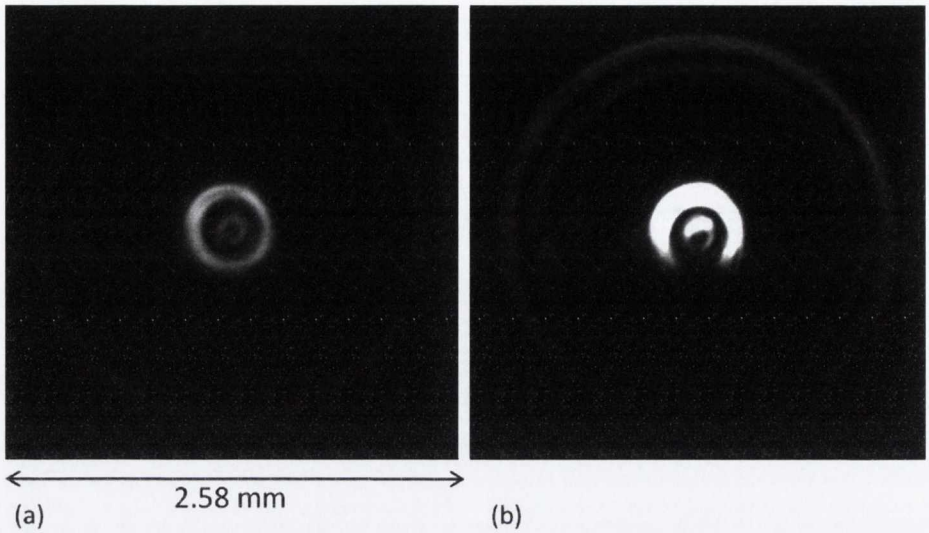

Figure 3.3.13: (a) CCD image taken using the experimental setup shown in Figure 3.3.12 with the order of the crystals as in the diagram. (b) An image of the beam shown in part (a) after propagation through a linear analyser.

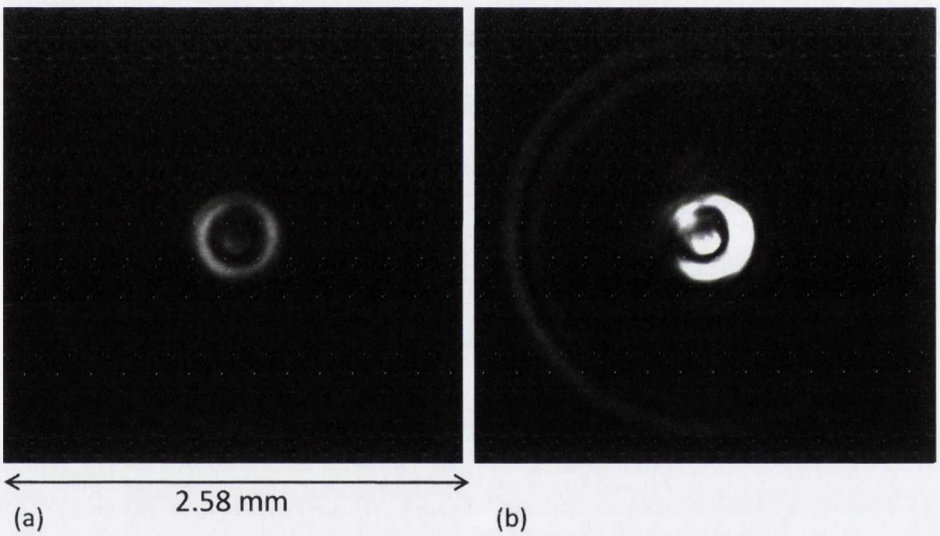

Figure 3.3.14: (a) CCD image taken using the experimental setup shown in Figure 3.3.12 with the order of the crystals reversed. (b) An image of the beam shown in part (a) after propagation through a linear analyser.

The arrangement shown in Figure 3.3.12 was also used to validate the intensity profiles predicted by equation 3.2.39 for cascade conical diffraction in unequal crystals. Figure 3.3.15 (a) and (b) show, respectively, a CCD image of the FIP recorded at the CCD with a rotation of 40° between the crystals and a comparison of the radial intensity distribution with theory. The experimental radial intensity distribution was taken across an azimuthally smoothed version of the image in Figure 3.3.15 (a). This smoothed image is included in Appendix B (Figure B.5).

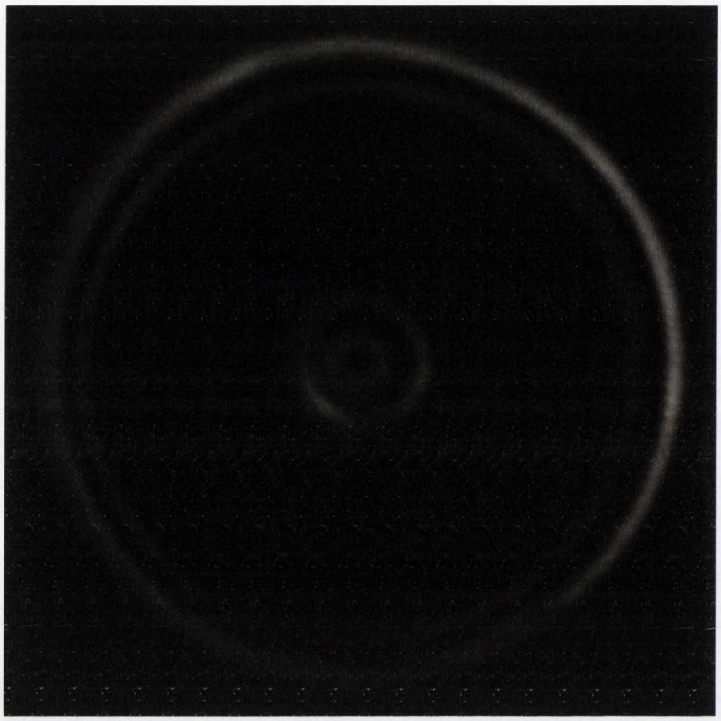

(a)

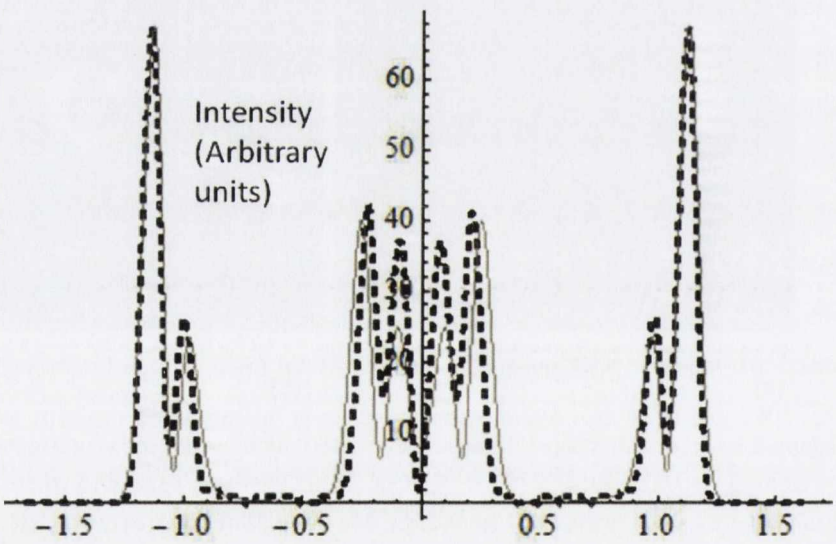

(b)

Figure 3.3.15: (a) An image recorded at the CCD of the beam generated with the setup shown in Figure 3.3.12 with $\alpha = 40^{\circ}$. (b) Measured radial intensity profile (black dashed line) compared with theory (grey line).

Chapter 4. Generation of Radially and azimuthally polarized beams via conical diffraction

In this Chapter we describe how the unique polarization properties of the conically diffracted Gaussian beam can be used to generate radially and azimuthally polarized light beams. The concepts of beams with radially and azimuthally oriented polarization vectors are introduced in Section 4.1. In Section 4.2 two distinct interferometric methods are shown to be capable of transforming a linearly polarized Gaussian beam into a radially (azimuthally) polarized B_1 beam. Both methods described in Section 4.2 were carried out in the laboratory and the results are analyzed and discussed in Section 4.3.

4.1. Radially and azimuthally polarized beams

Radially and azimuthally polarized beams are a class of circularly symmetric vector beams that have the property that their polarization vectors are oriented in the radial or azimuthal directions respectively (in a system of polar co-ordinates centred on the propagation axis of the beam).

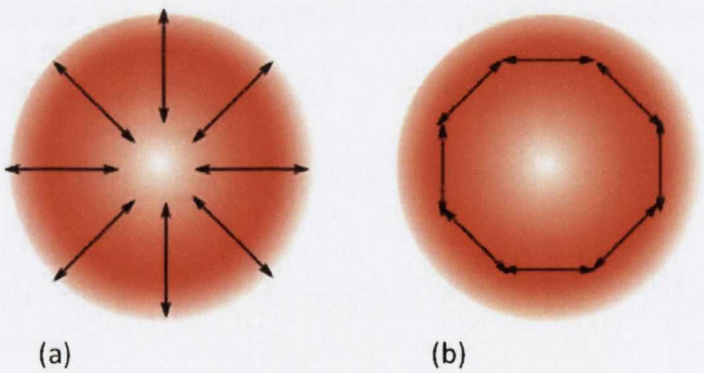

Figure 4.1.1: (a) A transverse slice of a radially polarized beam with the polarization vectors (black arrows) superimposed on the circularly symmetric intensity profile (red). (b) The same image for an azimuthally polarized beam.

They can be generated via a number of different methods such as interferometrically (Tidwell, Ford, & Kimura, 1990), by propagation through a conical Brewster prism (Kozawa & Sato,

2005) and by propagation through a segmented spiral phase plate (Lai, Lim, Phua, Tiaw, Teo, & Hong, 2008). They have a number of interesting characteristics including a tighter focused spot than a linearly or elliptically polarized beam (Quabis, Dorn, Eberler, Glokl, & Leuchs, 2000) and a large longitudinal electric field component when tightly focused (Youngworth & Brown, 2000) which can be used for z-polarization spectroscopy (Saito, et al., 2008).

The interferometric methods that are used to generate radially polarized beams (we will focus on the generation of radially polarized beams from now on since an azimuthally polarized beam can be generated from a radial one by propagation through a pair of half wave plates with their fast axes orthogonal to each other) generally consist of the superposition of orthogonally polarized Hermite-Gaussian TEM_{01} and TEM_{10} beams. This procedure is depicted schematically in Figure 4.1.2.

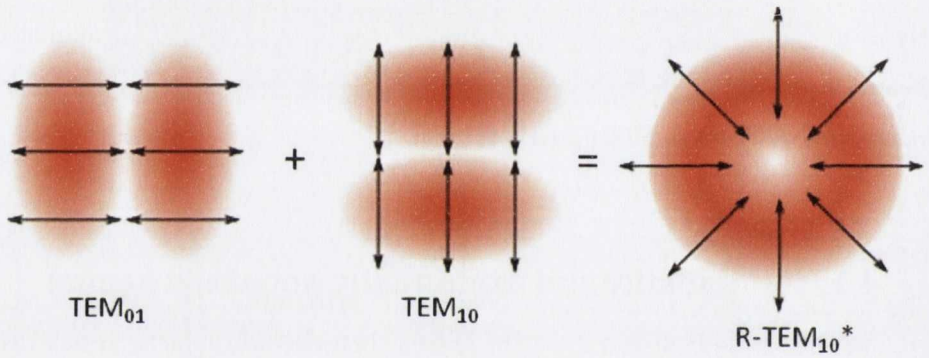

Figure 4.1.2: The superposition of orthogonal Hermite Gaussian beams leading to the formation of a radially polarized beam. The notation R-TEM_{10}* is used to distinguish the radially polarized doughnut mode from the linearly or circularly polarized one.

In the following section we will develop two distinct interferometric methods of converting a linearly polarized Gaussian into a radially polarized beam using conical diffraction.

4.2. Forming radially and azimuthally polarized beams interferometrically

We are considering the conversion of a linearly polarized Gaussian beam into a radially or azimuthally polarized beam via conical diffraction. In what follows we will describe two similar but distinct interferometric methods that can be used to achieve this.

The starting point for both methods is to conically diffract a linearly polarized Gaussian beam, converting it into a crescent beam. It was shown in Chapter 2 that if the incident Gaussian is

linearly polarized at an angle α to the positive x axis, the beam that emerges from the crystal has the following form:

$$\vec{E}(r,\theta,Z) = \mathrm{B}_0(r,Z)\begin{pmatrix}\cos\alpha\\ \sin\alpha\end{pmatrix} + \mathrm{B}_1(r,Z)\begin{pmatrix}\cos\varphi & \sin\varphi\\ \sin\varphi & -\cos\varphi\end{pmatrix}\begin{pmatrix}\cos\alpha\\ \sin\alpha\end{pmatrix}, \qquad 4.2.1.$$

where it has been assumed that the lateral displacement of the beam caused by conical diffraction is in the positive x direction. This beam will have an intensity profile with a maximum at an azimuthal angle of 2α, where the polarization has the same orientation as the incident beam, and a minimum at the azimuthal position of $2\alpha + \pi$ where the polarization is orthogonal to that of the incident beam. A schematic that represents the conversion of a Gaussian into the crescent beam is given in Figure 4.2.1.

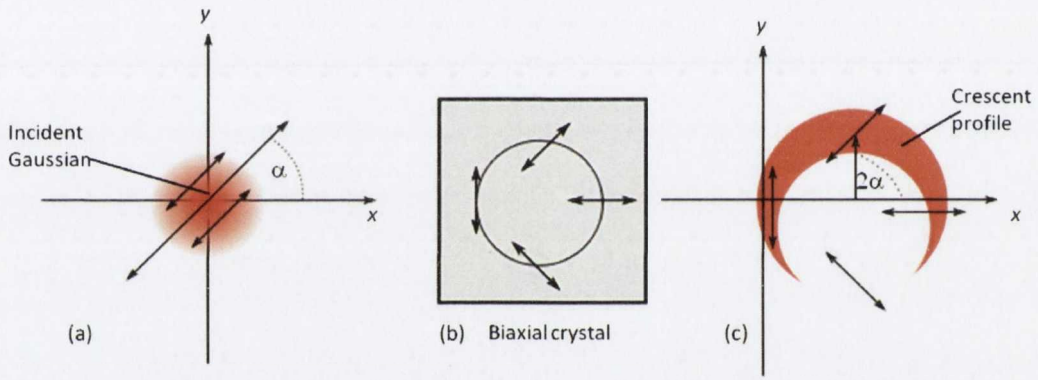

Figure 4.2.1: A schematic representation of the conversion of a Gaussian beam, polarized at an angle of α to the positive x axis (part (a)) into a beam with an intensity maximum at the angular position of 2α (part(c)) by propagation through a biaxial crystal with the orientation shown in part (b).

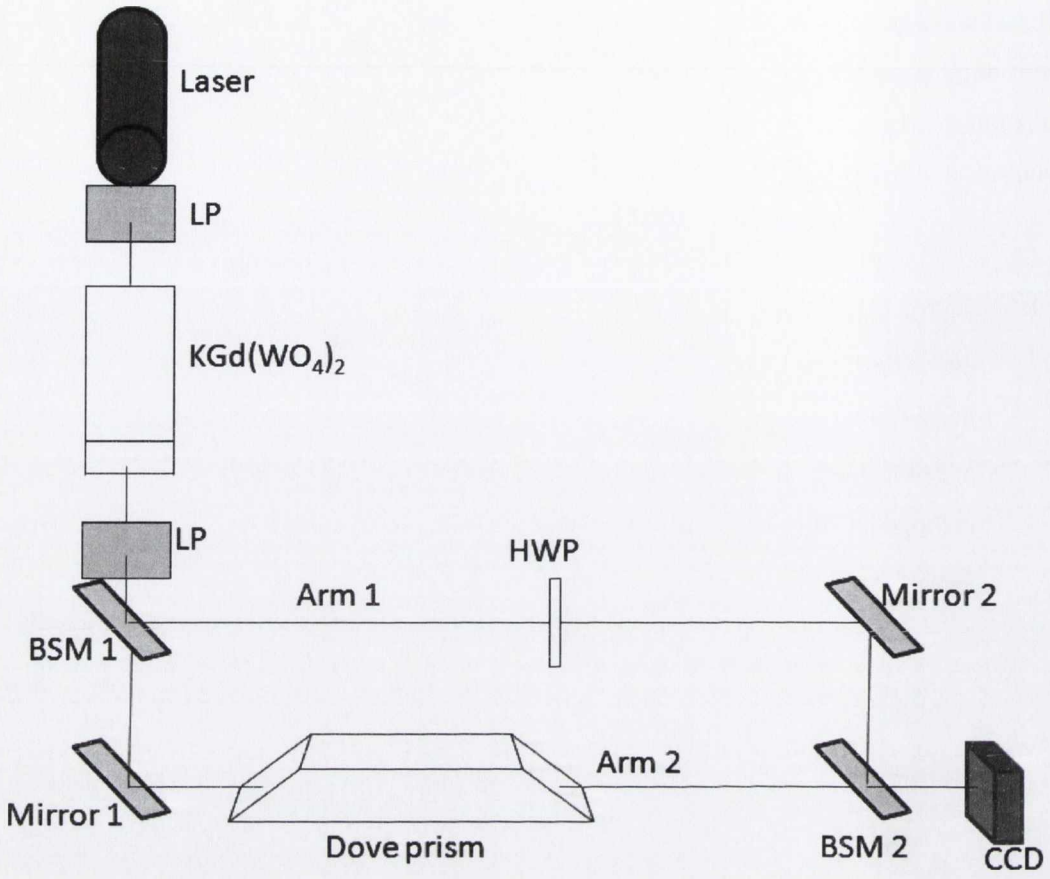

Figure 4.2.2: The experimental setup used to convert a linearly polarised Gaussian into an azimuthally or radially polarized beam. The radially polarized beam is formed at the BSM 2 (beam splitting mirror).

The basic idea behind the first method is to superimpose orthogonally polarized Hermite-Bessel like beams (described in chapter 2) that also have their transverse profiles rotated relative to each other by 90°. This process is represented in Figure 4.2.3 (and Figure 4.1.2). In order to generate these orthogonal Hermite-Bessel beams, the crescent beam, represented by equation 4.2.1, is propagated through a linear analyzer before entering a Mach-Zehnder interferometer (Figure 4.2.2). The beam that enters the interferometer has the form:

$$\vec{E}(r,\theta,Z) = \mathrm{B}_1(r,Z)\sin\varphi\begin{pmatrix}\sin\alpha\\-\cos\alpha\end{pmatrix}. \qquad 4.2.2.$$

In one arm of the interferometer (Arm 2 in Figure 4.2.2) this beam is propagated through a Dove prism oriented such that it rotates the transverse profile by 90° relative to the beam that propagates in the other arm. A Dove prism is a trapezoidal shaped prism that, when lying on its base (longest side in the diagram), will flip the profile of the beam that enters it in the vertical direction changing its handedness. If the Dove prism is rotated about the optic axis from this position it will rotate the incident beam profile by twice that angle. Hence in our setup the

Dove prism is oriented at 45° to the *x* axis (i.e. the edges joining the base and entrance/exit faces make 45° angles with the *x* axis). A half wave plate on one of the arms of the interferometer (Arm 1 in Figure 4.2.2) with its fast axis at 45° to the polarization vector of the beam that propagates along that arm rotates the polarization of that beam by 90°. Thus at the beam splitting mirror on Arm 2 of the interferometer we have a superposition of orthogonally oriented, orthogonally polarized Hermite – Bessel like beams as required. This superposition beam has the following form:

$$\vec{E}(r,\varphi,z) = \mathrm{B}_1 \sin\varphi \begin{pmatrix} \sin\alpha \\ -\cos\alpha \end{pmatrix} + e^{i\delta}\mathrm{B}_1 \cos\varphi \begin{pmatrix} \cos\alpha \\ \sin\alpha \end{pmatrix}, \qquad 4.2.3.$$

where δ is the phase difference between the beams on Arm 1 and Arm 2. This superposition beam is not necessarily radially polarized or azimuthally polarized. However we can arrange that it is radially polarized if we set the incident polarization to be horizontal (α=0) and set the phase difference $\delta = \pi$. In this case equation 4.2.3 becomes

$$\vec{E}(r,\theta,z) = -\mathrm{B}_1(r,Z) \begin{pmatrix} \cos\varphi \\ \sin\varphi \end{pmatrix}. \qquad 4.2.4.$$

This describes a radially polarised beam with an intensity profile given by $\mathrm{B}_1^*\mathrm{B}_1$. Hence it will have a near field double ring profile that diffracts into a diverging first order Bessel profile in the far field.

If we set the incident polarisation to be vertical (α=½π) and arrange that there be a π phase difference between the beams ($\delta = \pi$) then equation 4.2.3 becomes

$$\vec{E}(r,\theta,z) = \mathrm{B}_1 \begin{pmatrix} \sin\theta \\ -\cos\theta \end{pmatrix}. \qquad 4.2.5.$$

This describes an azimuthally polarized beam with the same intensity profile, $\mathrm{B}_1^*\mathrm{B}_1$, as the radially polarized beam (equation 4.2.4) . Note that there is no need to alter the orientation of the half wave plate or the dove prism when switching from radial to azimuthal polarization. In figure 4.2.3 the intensity profiles of the two orthogonal Hermite Bessel beams are plotted alongside their sum which is just the familiar far field B_1 profile. The polarization (Jones) vectors for the cases of radial and azimuthal polarization are plotted beneath the intensity profiles.

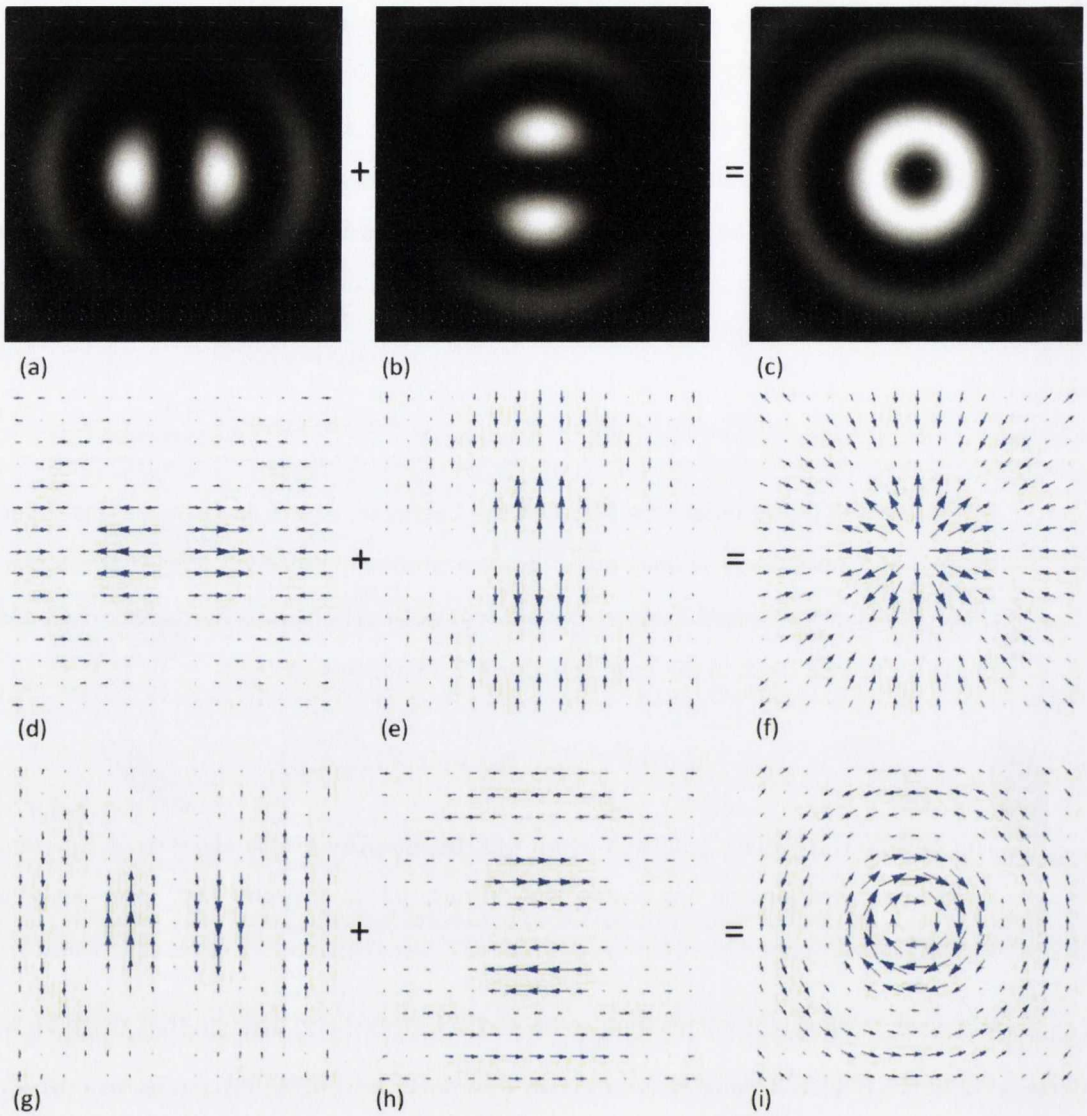

Figure 4.2.3: A simulation of the intensity profile of (a) the beam that emerges from Arm 1 of the interferometer in Figure 4.2.2; (b) the beam that emerges from Arm 2; (c) the beam that is formed by the superposition of the beams emerging from Arm 1 and Arm 2. (d), (e) and (f) show the polarization vectors of the beams leaving Arm1, Arm 2 and the recombined beam for the case of radial polarization. (g), (h) and (i) for the case of azimuthal polarization. The intensity profiles of the radially and azimuthally polarized beams are identical (equations 4.2.4, 4.2.5).

The second method for converting a Gaussian into a radially (azimuthally) polarized beam via conical diffraction is similar to the first, the main difference being that we remove the linear polarizer from in front of the exit face of the crystal so that a crescent beam enters the interferometer. In the setup in Figure 4.2.4 all of the power of the incident Gaussian propagates into the interferometer.

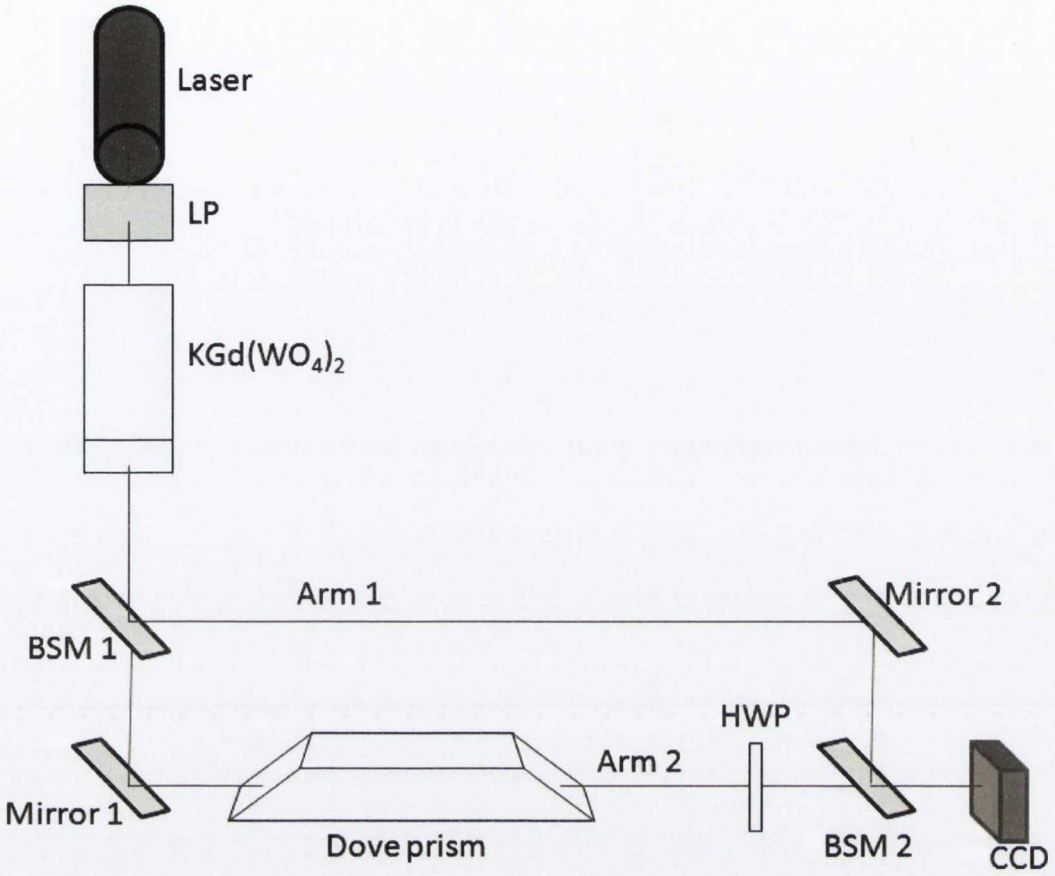

Fig 4.2.4: The experimental setup used to convert a linearly polarised Gaussian via the superposition of diffracting crescent beams. The only differences between this setup and the one used to superimpose orthogonal HB beams are that the linear polarizer between the crystal and interferometer is removed and the orientations of the HWP and Dove prism are changed.

The basic idea behind this method is to superimpose two crescent beams with one having been rotated by 180° about the propagation axis. This is depicted schematically in Figure 4.2.5.

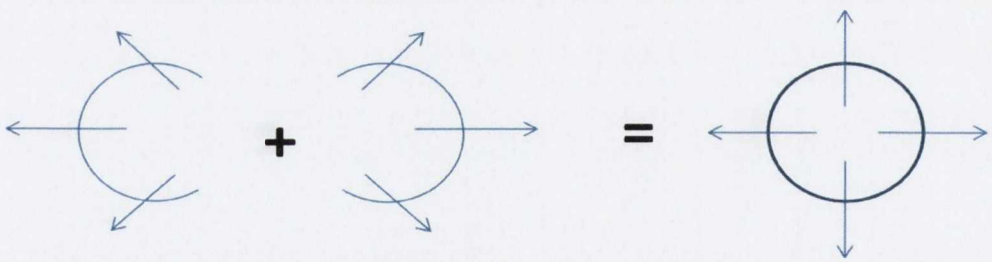

Figure 4.2.5: A superposition of two crescent profiles with a 180° relative rotation of their images about the propagation axis results in a circularly symmetric radially polarized beam.

This is achieved via the following method: Light from the laser is linearly polarized along the direction that corresponds to the radial direction in the polarization profile of the ring plane of conical refraction. If we choose this polarization to be horizontal (by appropriately setting the

azimuthal orientation of the crystal) then the electric field of the beam incident on the crystal is proportional to

$$e^{-r^2/\omega^2}\begin{pmatrix}1\\0\end{pmatrix}. \qquad 4.2.6.$$

Propagation through the crystal converts this into

$$B_0\begin{pmatrix}1\\0\end{pmatrix} + B_1\begin{pmatrix}\cos\theta\\\sin\theta\end{pmatrix}, \qquad 4.2.7.$$

which is a superposition of a linearly polarized (B_0) and radially polarized (B_1) electric field and has the polarization structure shown in Figure 4.2.6 and a crescent intensity profile in the FIP. In Arm 1 of the interferometer this beam is allowed to freely propagate. In Arm 2 the crescent shaped beam is rotated by 180° by propagation through a Dove prism oriented at 90° to the *x* axis so that its radially polarized intensity maximum is on the opposite side of the ring (Figure 4.2.5) to that of the beam emerging from Arm 1. This beam then passes through a half wave plate that has its fast axis oriented orthogonally to the radially polarized component (the polarization of the intensity maximum). This half wave plate has the effect of rotating the non-radial polarization components such that the polarization of the beam on Arm 2 is as depicted in Figure 4.2.5 relative to the polarization vectors of the beam on Arm 1. The electric field of the beam that exits the half wave plate on Arm 2 is given by:

$$B_0\begin{pmatrix}1\\0\end{pmatrix} - B_1\begin{pmatrix}\cos\theta\\\sin\theta\end{pmatrix}. \qquad 4.2.8.$$

The polarization vectors of the beams that emerge from Arm 2 (equation 4.2.8) and Arm 1 (equation 4.2.7) are plotted in Figure 4.2.6 (a) and (b) respectively.

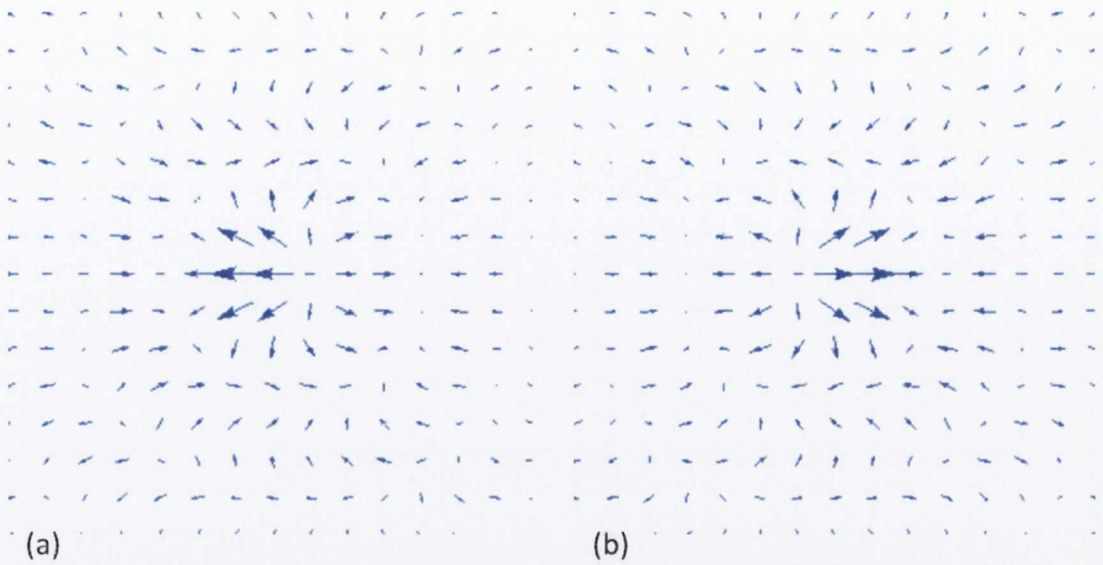

Figure 4.2.6: (a) A snapshot of the polarization vectors of the beam described by equation 4.2.8 that emerges from Arm 2 of the interferometer. (b) The polarization vectors of the beam that emerges from Arm 1 of the interferometer (The beam that enters both arms of the interferometer has the same polarization profile).

The crescent beams in the two arms are brought together at a beam splitting mirror and the superposition beam that propagates towards the CCD has the form

$$B_0 \begin{pmatrix} 1 \\ 0 \end{pmatrix} + B_1 \begin{pmatrix} \cos\theta \\ \sin\theta \end{pmatrix} + e^{i\delta} \left\{ B_0 \begin{pmatrix} 1 \\ 0 \end{pmatrix} - B_1 \begin{pmatrix} \cos\theta \\ \sin\theta \end{pmatrix} \right\}, \qquad 4.2.9.$$

where δ is the phase difference between the crescent beams resulting from slightly different propagation distances. From equation 4.2.9 it is clear that by controlling the phase difference between the crescent beams we can select between a uniformly linearly polarized B_0 beam ($\delta = 0$) and a radially polarized B_1 beam ($\delta = \pi$). This has the consequence that the intensity profile of the superposition beam described by equation 4.2.9 depends upon the phase difference between its two components and we can tell if we have the radially polarized beam by checking that we have a B_1 profile.

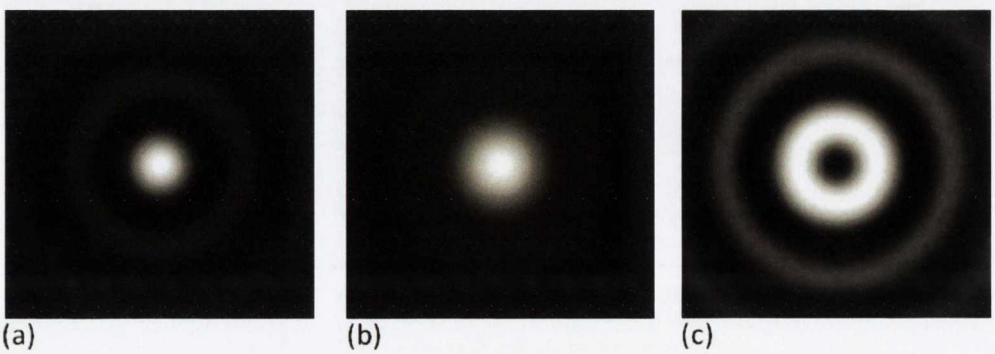

Figure 4.2.7: The far-field radial intensity patterns predicted by equation 4.2.9 for (a) $\delta = 0$; (b) $\delta = \pi/2$ and (c) $\delta = \pi$ (the radially polarized beam).

The far-field intensity profiles predicted by equation 4.2.9 are shown in Figure 4.2.7 for three values of δ. The near-field profiles corresponding to these far field profiles are just the ring profiles of the FIP which depend on incident beam waist in the manner outlined in Section 2.1. In Figure 4.2.8 we plot the polarization vectors of the beam described by equation 4.2.6 for a range of values of δ. As the phase difference, δ, is increased from zero to π the polarization state of the beam changes continuously from linear to radial polarization.

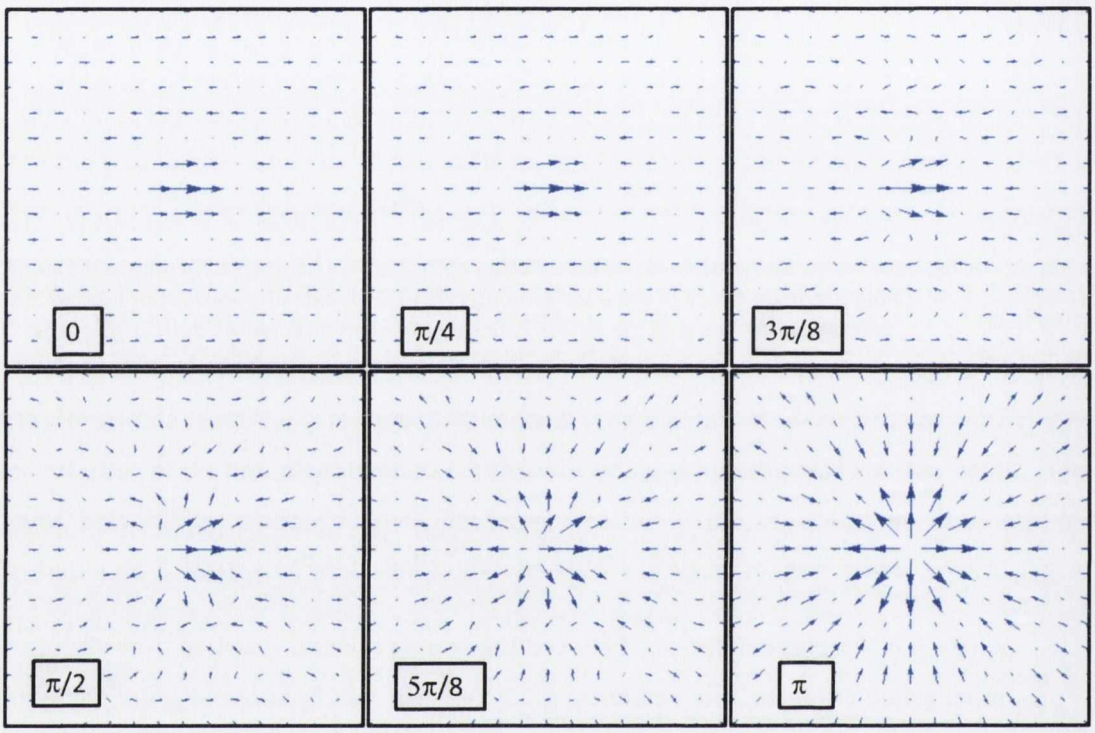

Figure 4.2.8: The polarization profile of the beam formed by the superposition of crescent beams. As the phase difference between the crescent beams is increased from zero to π the polarization state of the beam continuously changes from uniform linear polarization to radial polarization. These simulations were done in the far field.

In Figure 4.2.9 the distribution of normalized Stokes vectors is plotted in the transverse plane in the FIP for the case of radial polarization. This normalized Stokes vector is defined in the following way.

$$\vec{S} = \{{}^{S_1}/_{S_0}, {}^{S_2}/_{S_0}, {}^{S_3}/_{S_0}\} \qquad 4.2.10.$$

$$S_0 = I = \left(E_x^2 + E_y^2\right) = \left(E_a^2 + E_b^2\right) = \left(E_{LC}^2 + E_{RC}^2\right) \qquad 4.2.11.$$

$$S_1 = \left(E_x^2 - E_y^2\right)/\left(E_x^2 + E_y^2\right), \qquad 4.2.12.$$

$$S_2 = \left(E_a^2 - E_b^2\right)/\left(E_a^2 + E_b^2\right) \qquad 4.2.13.$$

$$S_3 = (E_{LC}^2 - E_{RC}^2)/(E_{LC}^2 + E_{RC}^2) \qquad 4.2.14.$$

where E_x^2 is the intensity transmitted by a linear analyser that transmits x (horizontal) polarization. The $\{a, b\}$ axes are an alternative set of transverse axes that are rotated clockwise by 45° relative to the $\{x, y\}$ axes. $E_{LC}^2$and E_{RC}^2 refer to the intensities transmitted by left and right circular analysers. In the plots of the Stokes vector distributions $S_1$is the x component, S_2 is the y component and S_3 is the z component (pointing out of the page in the positive direction).

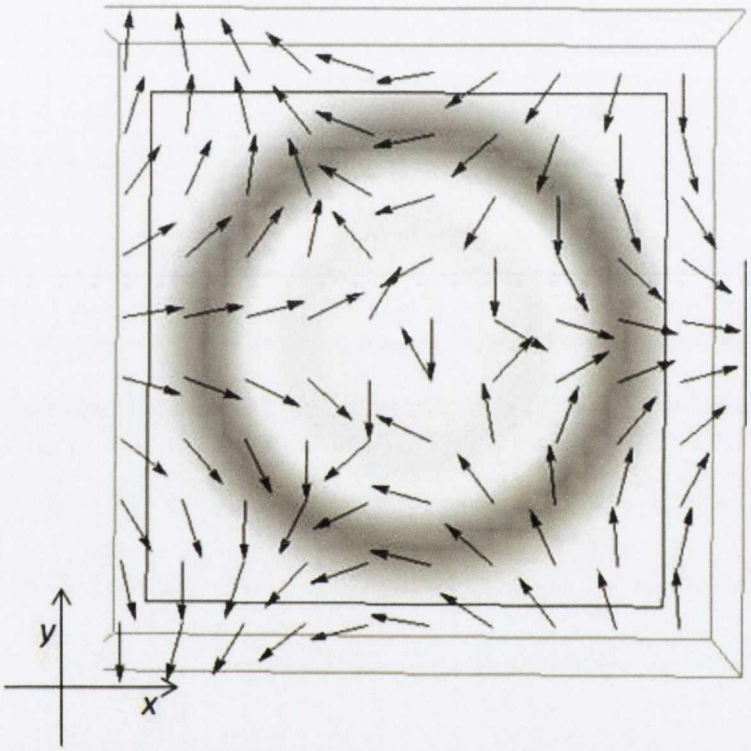

Figure 4.2.9: The Stokes vector of the radial polarized beam in the focal image plane. The vector has no z component at any point in the transverse plane.

If we set $\delta = \pi/2$ the superposition beam has an interesting polarization profile. The polarization is linear at two diametrically opposite points on the ring and circular at two diametrically opposite points with the line connecting the linearly polarized points being orthogonal to the line connecting the circularly polarized points. The polarization state of the beam as a function of azimuth is indicated in Figure 4.2.10. Equation 4.2.7 also tells us that the polarization at the centre of the beam is linear horizontal.

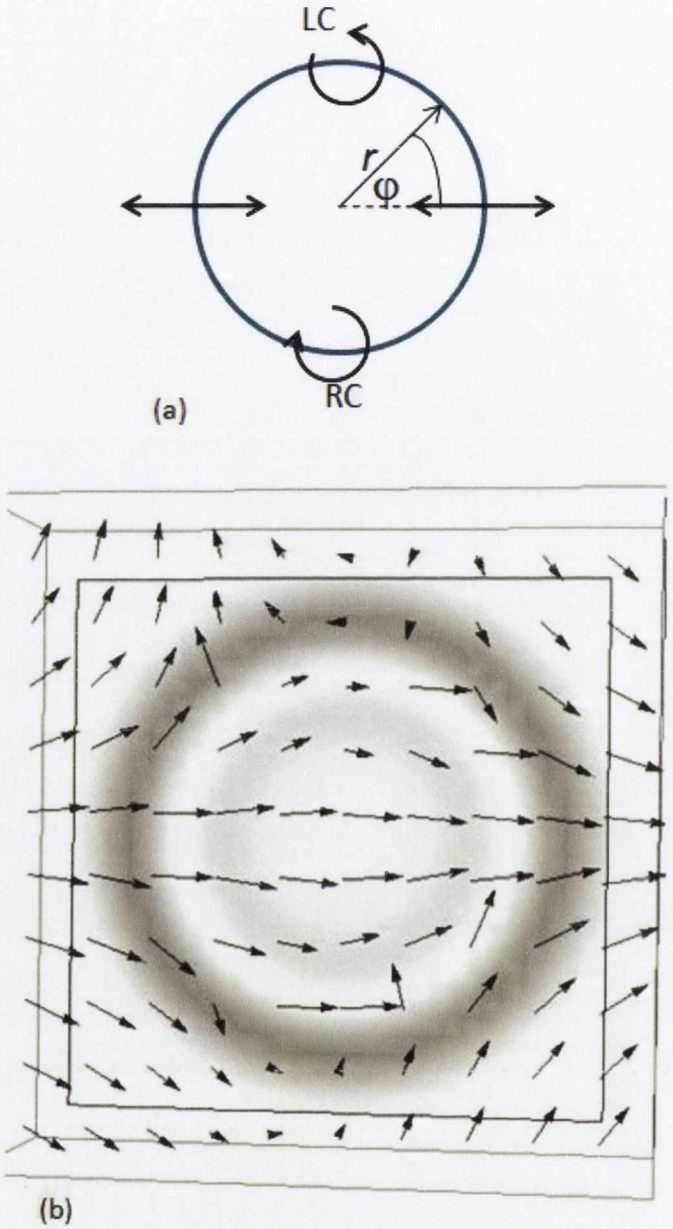

Figure 4.2.10: (a) The polarization state of the crescent superposition beam (equation 4.2.6) with $\delta = \pi/2$. The polarization changes continuously from linear to left circular to linear to right circular and back again to linear in a 2π azimuthal circuit. (b) A plot of the Stokes vector shows the line of linear polarization in the horizontal direction and the two points of circular polarization (arrows pointing out of the page) at diametrically opposite points.

An azimuthally polarized beam can be generated using the same steps but with the light incident on the crystal being polarized along the direction that is azimuthal with respect to the polarization profile of the ring. In Figure 4.2.4 we would just have to insert a half wave plate with its fast axis oriented at 45° to the horizontal between the laser and the interferometer to convert the radially polarized beam to an azimuthally polarized one. The electric field of the azimuthally polarized beam generated this way is

$$B_0\begin{pmatrix}0\\1\end{pmatrix} + B_1\begin{pmatrix}\sin\theta\\-\cos\theta\end{pmatrix} + e^{i\delta}\left\{B_0\begin{pmatrix}0\\1\end{pmatrix} - B_1\begin{pmatrix}\sin\theta\\-\cos\theta\end{pmatrix}\right\}. \qquad 4.2.15.$$

Figure 4.2.11 shows the polarization vectors of this beam for a range of values of δ.

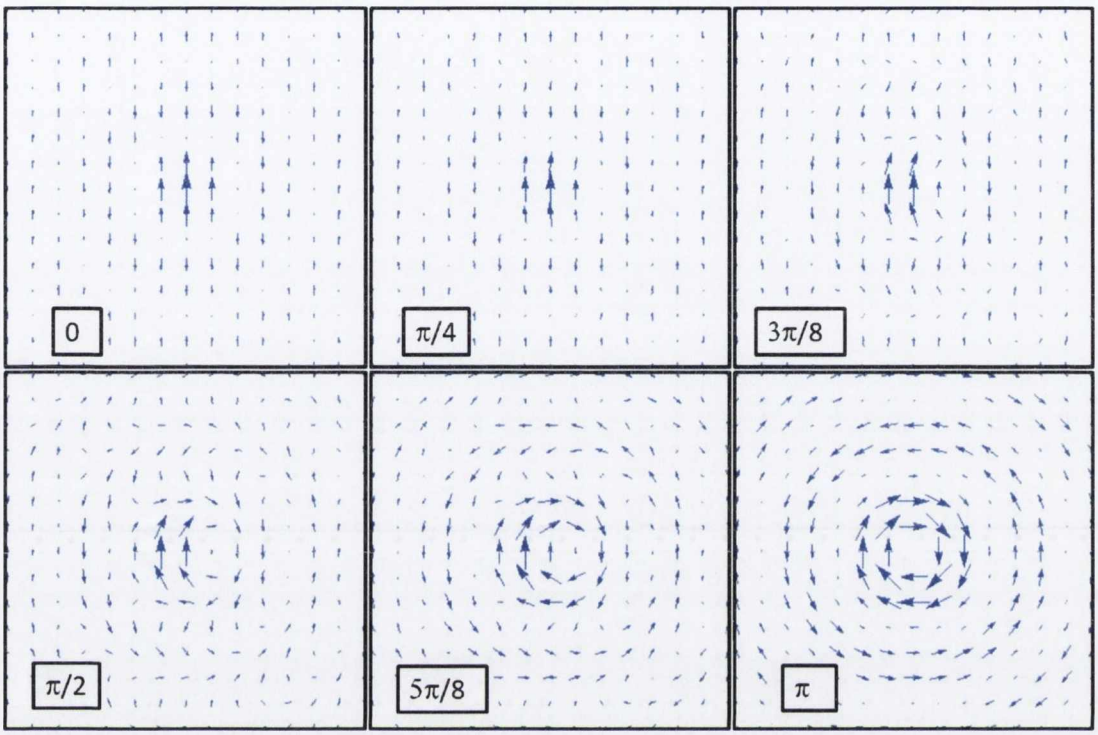

Figure 4.2.11: The formation of an azimuthally polarized beam via the superposition of crescent beams. The number on each polarization profile is the phase difference between the two interfering crescent beams.

4.3. Experimental realisation

Both methods described in section 4.3.2 were used to generate radially polarized beams in the laboratory. The results are presented in this section.

A: A superposition of linearly polarized Hermite-Bessel beams.

The interferometer used to generate a radially polarized beam via the superposition of orthogonal Hermite – Bessel like beams was described in the last section. Figure 4.3.1 shows this interferometer with the experimental parameters indicated.

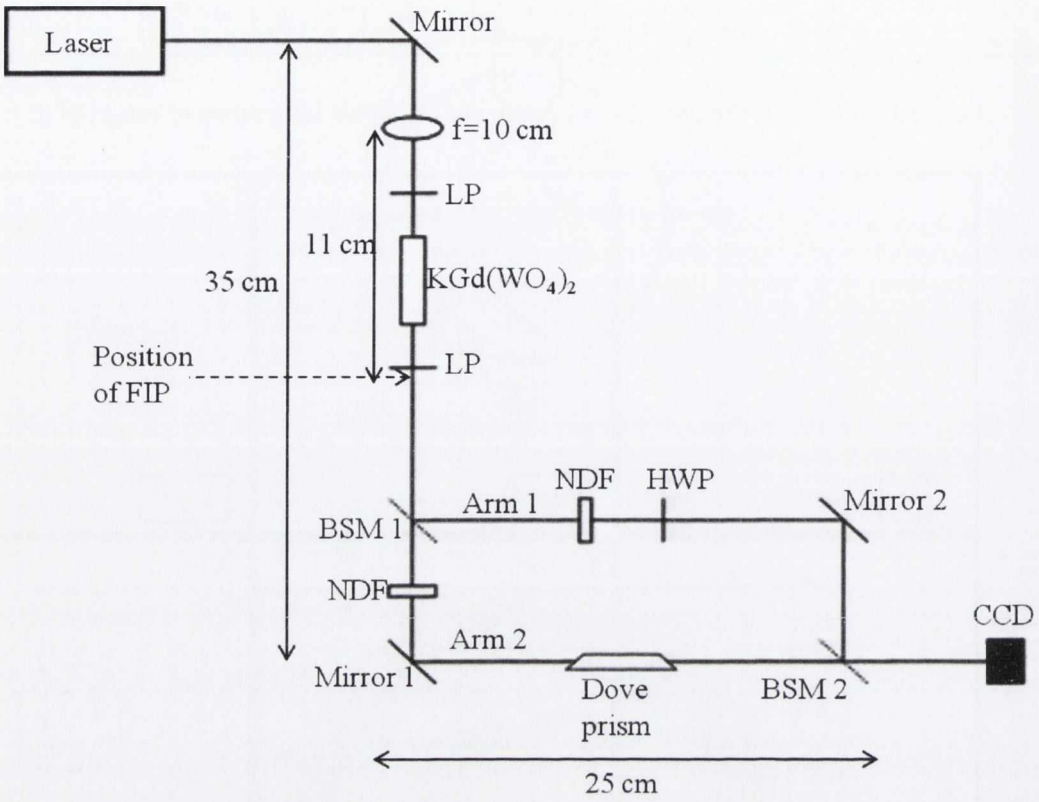

Figure 4.3.1: The experimental setup used to convert a linearly polarized Gaussian into a radially polarized beam. In this setup Hermite-Bessel like beams were superimposed.

The linearly (vertically, or along the *y* axis) polarized light from the laser (10 mW He-Ne) propagated through a 10 cm lens, transforming it into a beam with minimum beam waist ω_0 of 60 μm, before entering the crystal (the waist was formed beyond the crystal). The crystal used in this experiment was a 20.9 mm length slab of $KGd(WO_4)_2$ with an R_0 value of 0.37 mm at 632 nm (the wavelength of the laser). Upon exiting the crystal the beam propagated through another linear polarizer, this one transmitting horizontally (*x*) polarized light. This process is represented schematically in Figure 4.3.2.

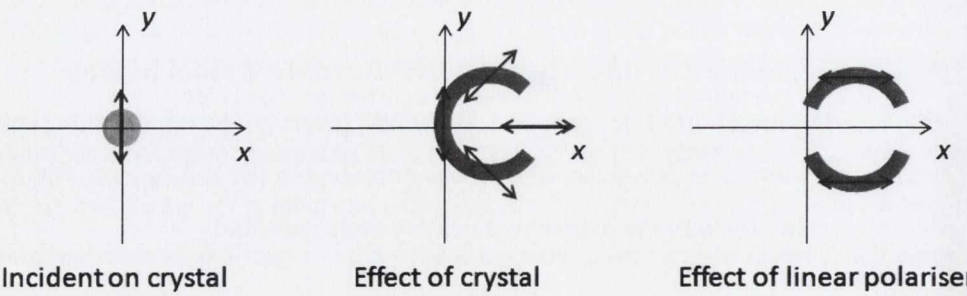

Figure 4.3.2: A schematic representation of the preparation of the beam that enters the interferometer in Figure 4.3.1. The transverse co-ordinates we use throughout this section are indicated on the diagram.

This horizontally polarized beam propagated through a half wave plate in Arm 1 of the interferometer and through a Dove prism in Arm 2. The beams were re-combined at the beam splitting mirror (BSM 2). The phase difference between the beams was controlled by controlling the mirror (mirror 2) which was mounted on a piezo-electric stage. In order to track the polarization state of the beam as it propagated through the optical system we describe the beam and the crystal orientation in a co-ordinate system with the beam propagating along the z axis. The *x* axis is the horizontal direction and the *y* axis is the vertical direction. In this co-ordinate system the crystal is oriented so that the generated cone of refraction leads to a displacement of the centre of the incident beam (by a distance of R_0) in the positive *x* direction. The incident polarization was vertical which means that the Hermite-Bessel beam formed (that entered the interferometer) had horizontal polarization as well as a horizontal line of zero intensity. This beam propagated through a half wave plate on Arm 1 that converted its polarization to vertical. The beam propagating through Arm 2 was rotated by 90° by the Dove prism so that its line of zero intensity was along the *y* axis and the polarization remained horizontal. Images of the intensity profiles of the beams that emerged from Arm 1 and Arm 2 of the interferometer are shown in Figure 4.3.3(a) and Figure 4.3.3 (b) respectively. The beam that resulted from their superposition is shown in Figure 4.3.3 (c). A linear intensity profile of the superposition beam from Figure 4.3.3 (c) is given in Figure 4.3.4. It compares well with the profile given by $B_1^* B_1$ at 65 cm from the FIP.

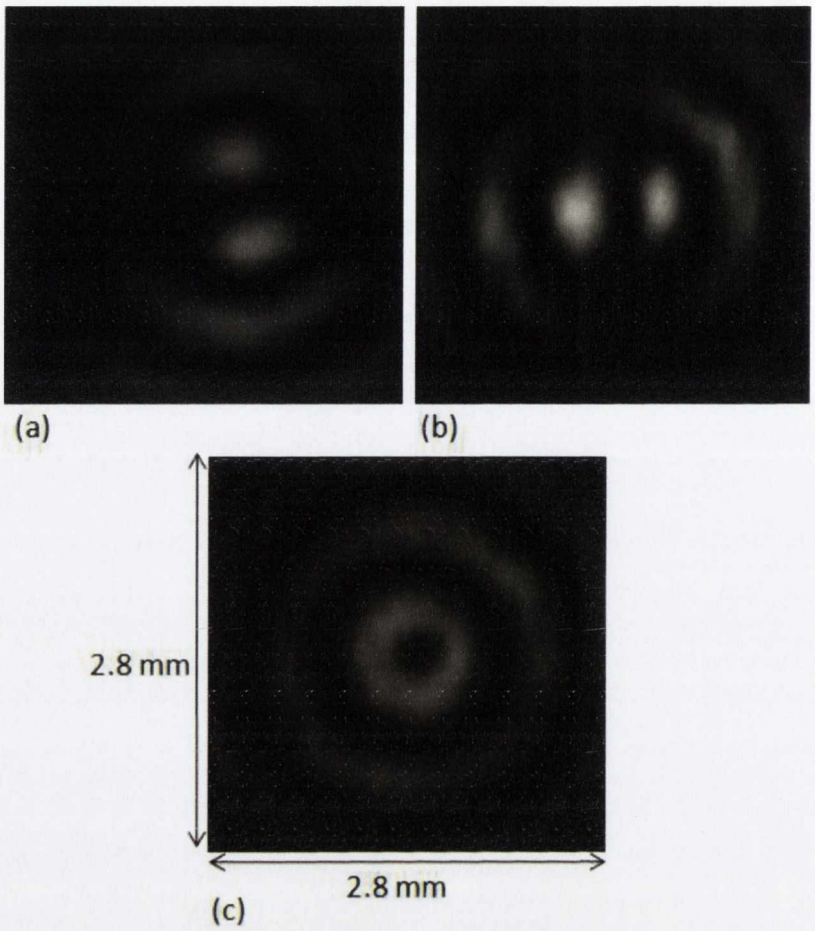

Figure 4.3.3: Intensity profiles of the beams that propagated along arms 1 and 2 of the interferometer ((a) and (b) respectively) and their superposition (c). Each image was recorded by the CCD without changing the position of the CCD. The Arm 2 beam was blocked to record the Arm 1 beam and vice versa.

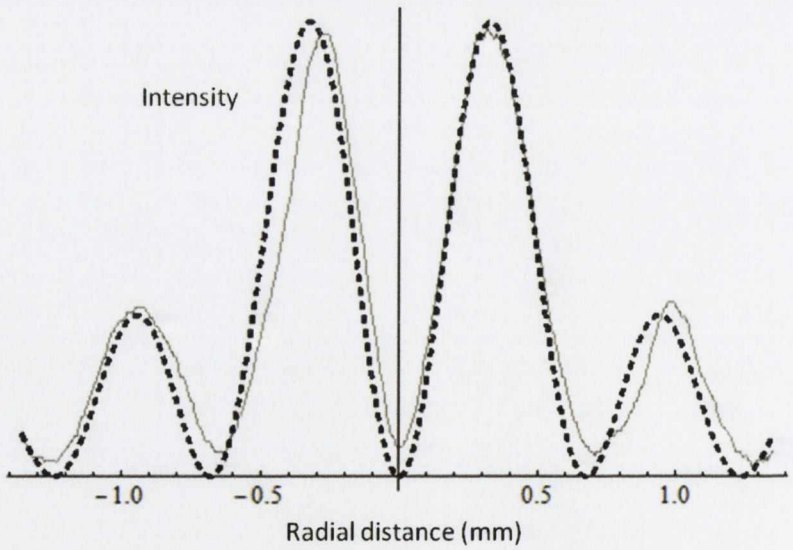

Figure 4.3.4: The radial intensity distribution of the radially polarized beam taken along the diagonal from the top left to the bottom right corners of the Figure 4.3.2 (c) plotted alongside the B_1 intensity profile (black dashed line) at 65 cm from the FIP.

In combining these beams we also had to adjust the phase difference to 90° between them. To ensure that this is the case it sufficed to place a linear polarizer in the path of the beam that emerges from the interferometer and rotate the polarizer by 180°. If the beam was radially polarized then a dark line that cuts the B_1 profile in half should appear and as the polarizer is rotated the line should rotate with the polarizer. Figure 4.3.5 shows the images taken at the CCD of the radially polarized beam without the polarizer and of the beam transmitted propagation through a linear polarizer set at various angles. These images were taken at a distance of ~65cm from the FIP. Figure 4.3.6 shows simulations of the expected intensity profiles for these parameters.

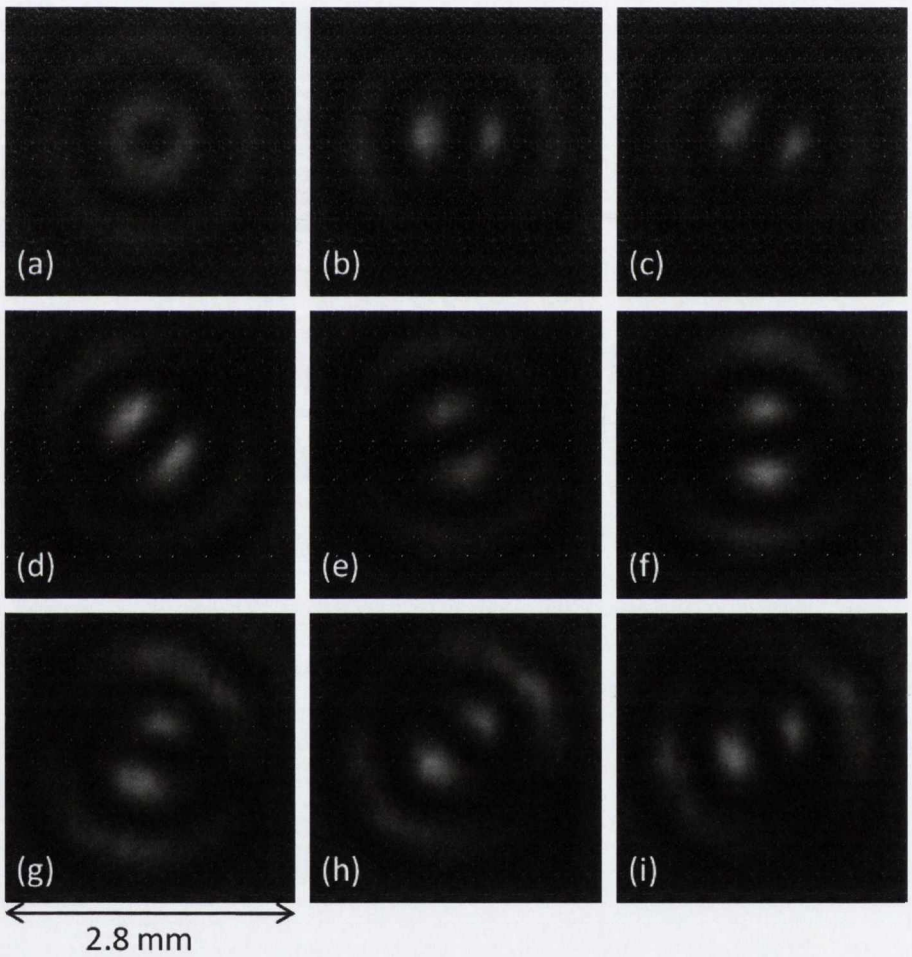

Figure 4.3.5: (a) A CCD recording of the intensity profile of the radially polarized beam. (b)-(i) The radially polarized beam after propagation through a linear analyzer. The analyzer is rotated in steps of 22.5° starting from (b). The analyzer is set to transmit horizontally polarized light in image (b).

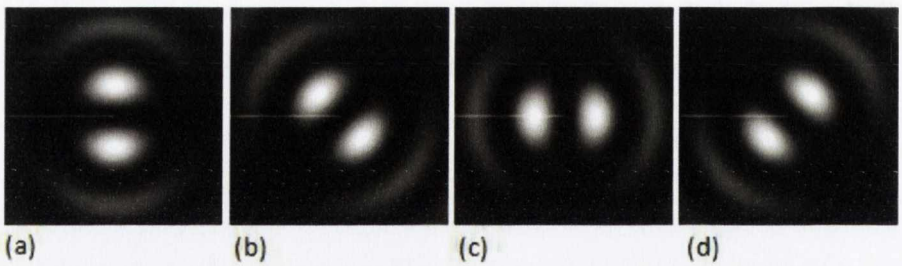

Figure 4.3.6: Numerical simulations of the intensity profiles corresponding of the radially polarized beam after propagation through a linear polarizer. These 2D plots were generated from Equation 4.2.4 with the experimental parameters mentioned in this section and Berry's far field approximate formula for B_1 (Equation 6.5 in (Berry, 2004)).

The Stokes parameters that characterize the linearly polarized state of the beam are calculated from the experimental data in Figure 4.3.5 and plotted in Figure 4.3.7. These Stokes parameters are defined in the standard way as

$$S_0 = I = E_x^2 + E_y^2 = E_a^2 + E_b^2 = E_L^2 + E_R^2,$$

$$S_1 = (E_x^2 - E_y^2)/(E_x^2 + E_y^2),$$

$$S_2 = (E_a^2 - E_b^2)/(E_a^2 + E_b^2),$$

where the $\{a, b\}$ axes are rotated by 45° relative to the $\{x, y\}$ axes and I is the total intensity. E_x^2 is the intensity transmitted by a linear polarizer that transmits light polarized in the x direction. In Figure 4.3.5 we have images of E_x^2 in part (b); E_y^2 in part (f); E_a^2 in part (d); E_b^2 in part (h). Theoretical simulations of the same Stokes parameters are given in Figure 4.3.8.

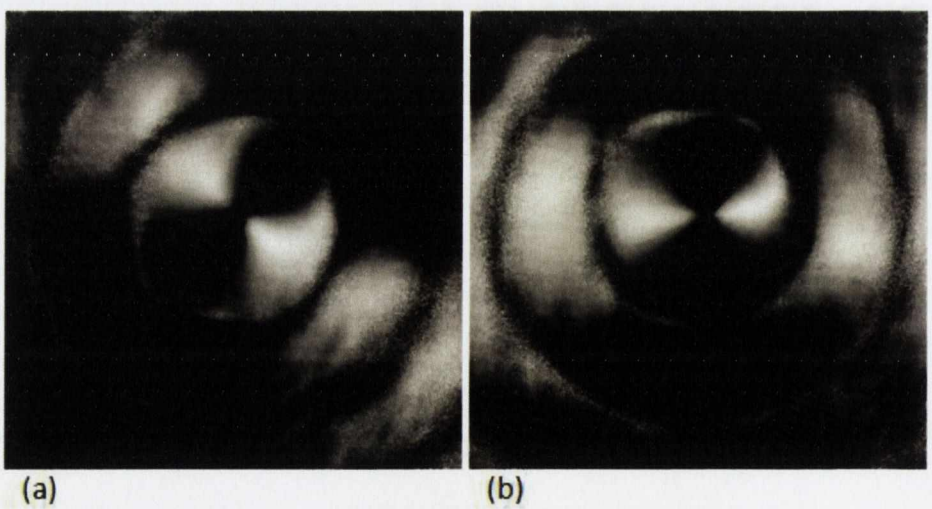

Figure 4.3.7: The normalized Stokes parameters describing the linear polarization state of the radially polarized beam calculated from the experimental images in Figure 4.3.3. (a) S_2:The normalized difference in intensities measured with the analyser at 45° and 135°. (b) S_1:The normalized difference in intensities measured with the analyser at 0° and 90°.

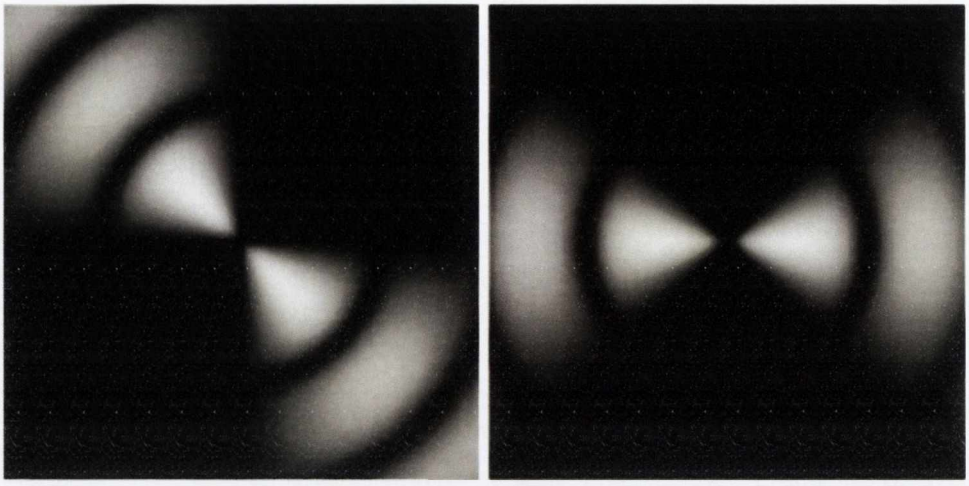

Figure 4.3.8: Numerical simulation of the normalized Stokes parameters corresponding to the experimental ones in Figure 4.3.5. (a) S_2. (b) S_1. In these simulations the far field profile of the B_1 integral is approximated with a first order Bessel function (Berry, 2004).

It was noted in the previous chapter that since the {r, z} dependence of the radially polarized beam is proportional to B_1, the radially polarized beam should have a ring profile as well as a diverging first order Bessel profile. Using the lens arrangement shown in Figure 4.3.9 the ring (FIP) plane of the radially polarized beam was imaged onto the CCD.

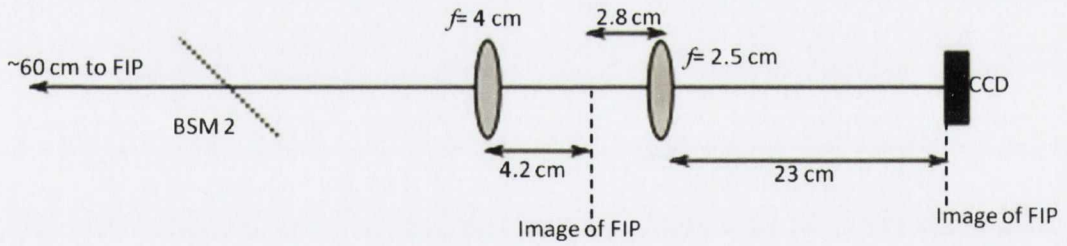

Figure 4.3.9: The lens arrangement used to image the ring plane (FIP) of the radially polarized beam onto the CCD.

Figure 4.3.10 shows images of the radially polarized ring (part (c)) as well as the Arm 1 (a) and Arm 2 (b) components of the ring. A linear intensity profile of the ring plane is plotted in Figure 4.3.11 based on the data in Figure 4.3.10 (c).

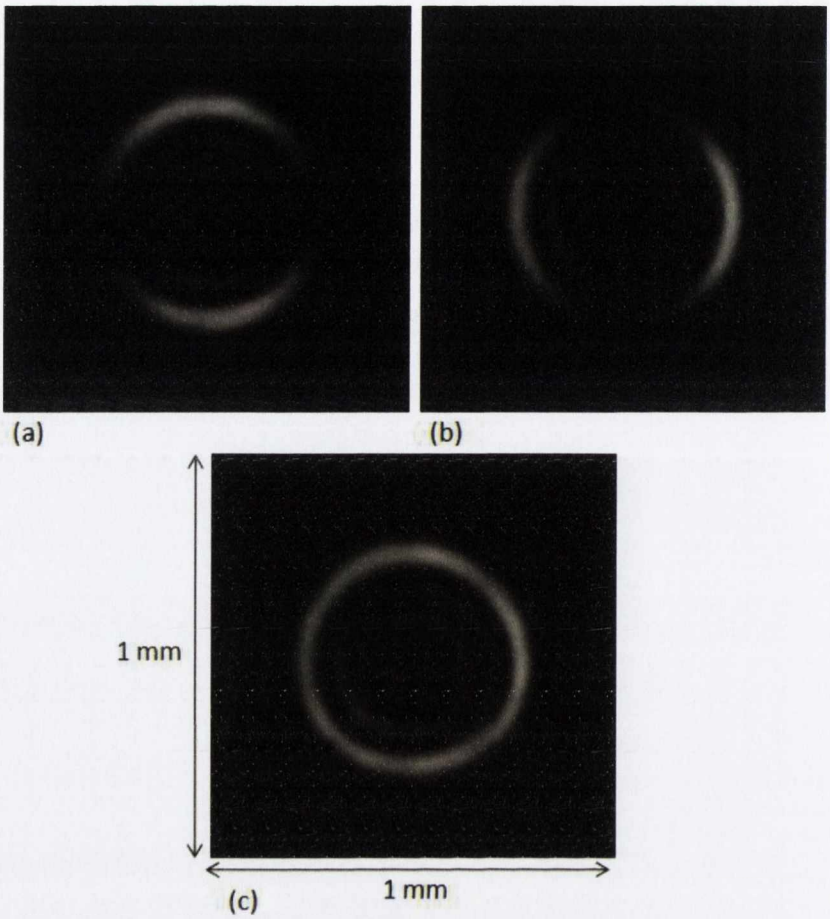

Figure 4.3.10: Intensity profiles of the beams that propagated along arms 1 and 2 of the interferometer ((a) and (b)) and their superposition (c).

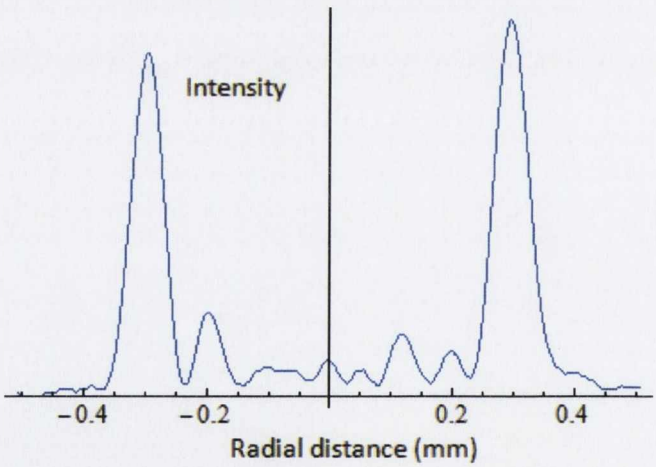

Figure 4.3.11: A linear plot of the intensity of the radially polarized ring. The line along which the intensity is plotted was taken across the ring in the vertical direction in Figure 4.3.10 (c).

B: A superposition of linearly polarized crescent beams.

The method for generating radially polarized beams via the superposition of diffracting crescent beams was carried out with the experimental parameters indicated in Figure 4.3.12. The same He-Ne laser was used in this experiment but this time the conically diffracted beam was formed by bringing the laser light to a focus in a 30 mm slab of $KGd(WO_4)_2$ with a 15 cm focal length lens which focused the incident beam to a minimum beam waist of 100 μm. The other (minor) differences are indicated in Figure 4.3.12.

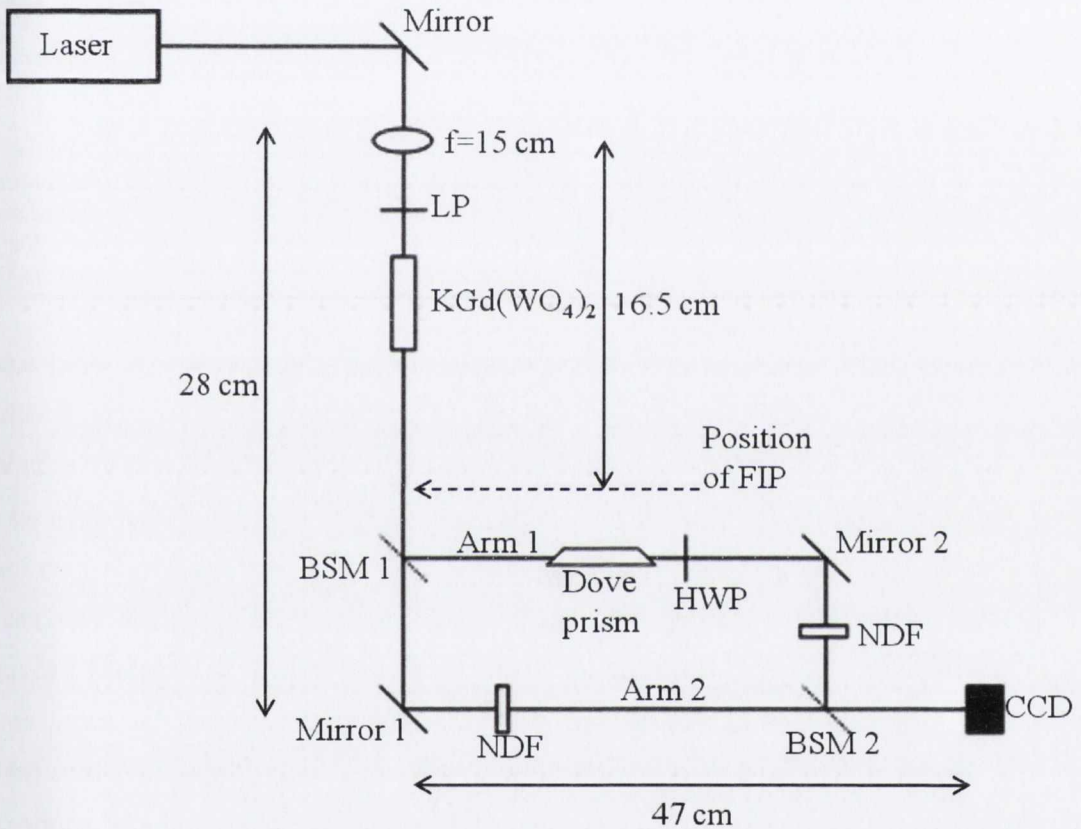

Figure 4.3.12: The setup used to convert a linearly polarized Gaussian into a radially polarized beam via the superposition of crescent beams. A quarter wave plate and linear polarizer were inserted between the BSM on Arm 2 to measure the Stokes parameters.

The crystal was oriented such that the cylinder that the Gaussian was refracted into was refracted in the positive *y* direction in our laboratory co-ordinated introduced earlier. This implies that the vertical polarization vector is the only direction on the cylinder of conical refraction that is aligned with a radius drawn from the centre of the cylinder. Figure 4.3.13 shows the polarization vectors of the conically diffracted cylinder and the position of the incident Gaussian relative to the conically diffracted crescent in the FIP.

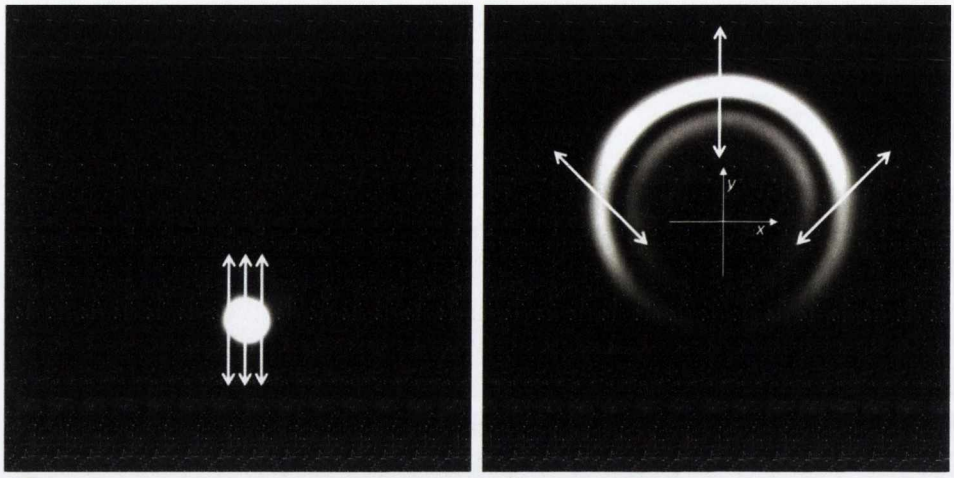

Figure 4.3.13: Experimental transverse intensity profiles of (a) the linearly (vertically) polarized Gaussian that entered the biaxial crystal and (b), the crescent that the Gaussian was conically diffracted into. The linear polarization state of each beam (white arrows) is superimposed on the intensity profile. The co-ordinate system we use to describe the radially polarized beam is drawn on part (b) with its origin at the centre of the crescent. These images were taken with the CCD placed at the FIP.

On Arm 1 of the interferometer this beam propagated through a Dove prism which rotated its beam profile by 180°. A half wave plate with its fast axis aligned with the horizontal (x) direction rotated each linear polarization vector by twice the angle that they made with the horizontal. Figures 4.3.14 and 4.3.15 show the effect that the Dove prism and half wave plate have on the crescent beam. Figure 4.3.14 shows the beam that propagates on Arm 1 with the Dove prism and half wave removed and Figure 4.3.15 ((a) and (b)) show the same beam after propagation through a linear polarizer oriented at two different angles. Figure 4.3.15 (parts (c)-(f)) show the effect of propagation through the Dove prism has on this beam as well as propagation through the combination of Dove prism followed by half-wave plate. The images in Figures 4.3.14 and 4.3.15 were taken at approximately 1.8 cm from the FIP so the crescent profile has undergone some broadening due to diffraction.

Figure 4.3.14: Experimental transverse intensity profile of the diffracted crescent beam measured on Arm 1 of the interferometer (Figure 4.3.12) at 18 cm from the FIP with the half-wave plate and Dove prism removed.

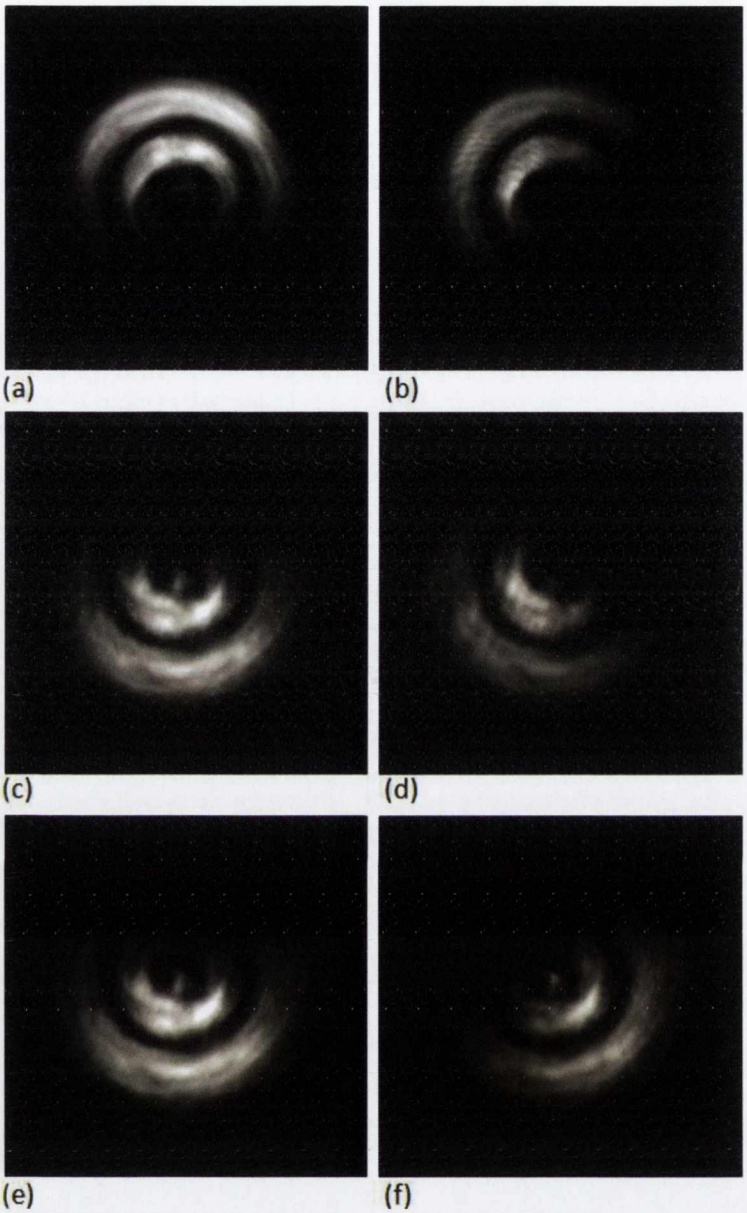

Figure 4.3.15: Experimental transverse intensity profiles of the diffracted crescent beam profile measured on Arm 1 of the interferometer (Figure 4.3.12) at 18 cm from the FIP. Parts (a) and (b) show the profiles of the beam featured in Figure 4.3.14 after propagation through a linear polarizer transmitting vertically polarized light and transmitting light at 45° to the vertical respectively. Parts (c) and (d) show the same beam after propagation through the Dove prism and linear polarizer at the same respective orientations as in parts (a) and (b). Parts (e) and (f) show the beam after propagation through the Dove prism followed by the half wave plate with its fast axis along the horizontal and then linear polarizer at the same respective orientations as in parts (a) and (b.

The beams that propagated through Arm 1 and Arm 2 were recombined at the beam splitting mirror on Arm 2. It was noted in the section 4.2.2 that the radially polarized beam would only be formed if the phase difference between the beams was half a wavelength (π). We can tell that this is the case if the beam at the CCD acquires a B_1 profile since for all other cases the

intensity profile is a mixture of B_0 and B_1 (Equation 4.2.9). Figure 4.3.16 shows the B_1 profile formed at the CCD (a) and a radial intensity plot based on the same data.

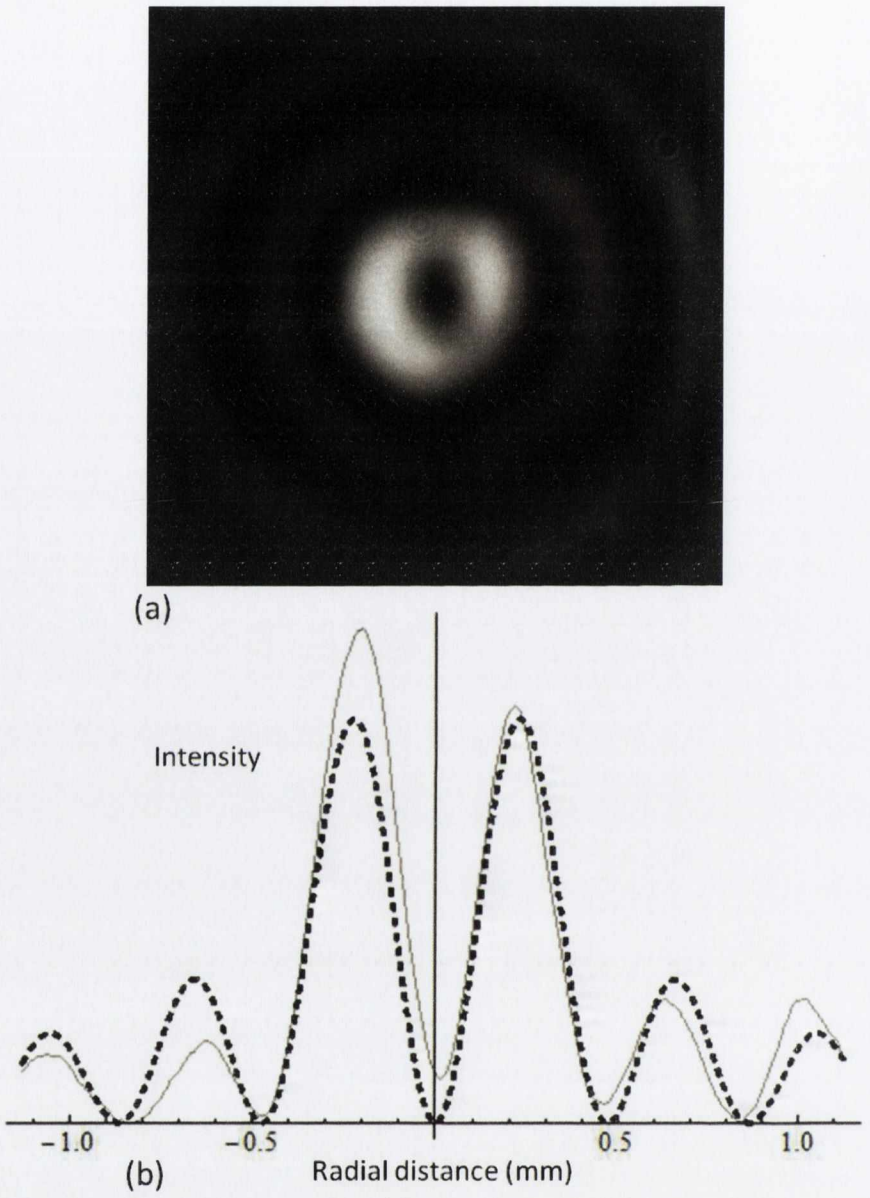

Figure 4.3.16: The radially polarized beam formed via the superposition of crescent beams. (a)The intensity profile measured at the CCD. The image shows some blurring due to the unstable optical bench. (b) The linear intensity profile taken across the horizontal axis in part (a) compared with theory (dashed black line).

Measurement of the Stokes parameters was difficult for this experimental setup due to the sensitivity of the optical bench to vibrations. Experimental images of the Stokes parameters are given in Figure 4.3.17. The theoretical Stokes parameters are the same as those depicted in Figure 4.3.8.

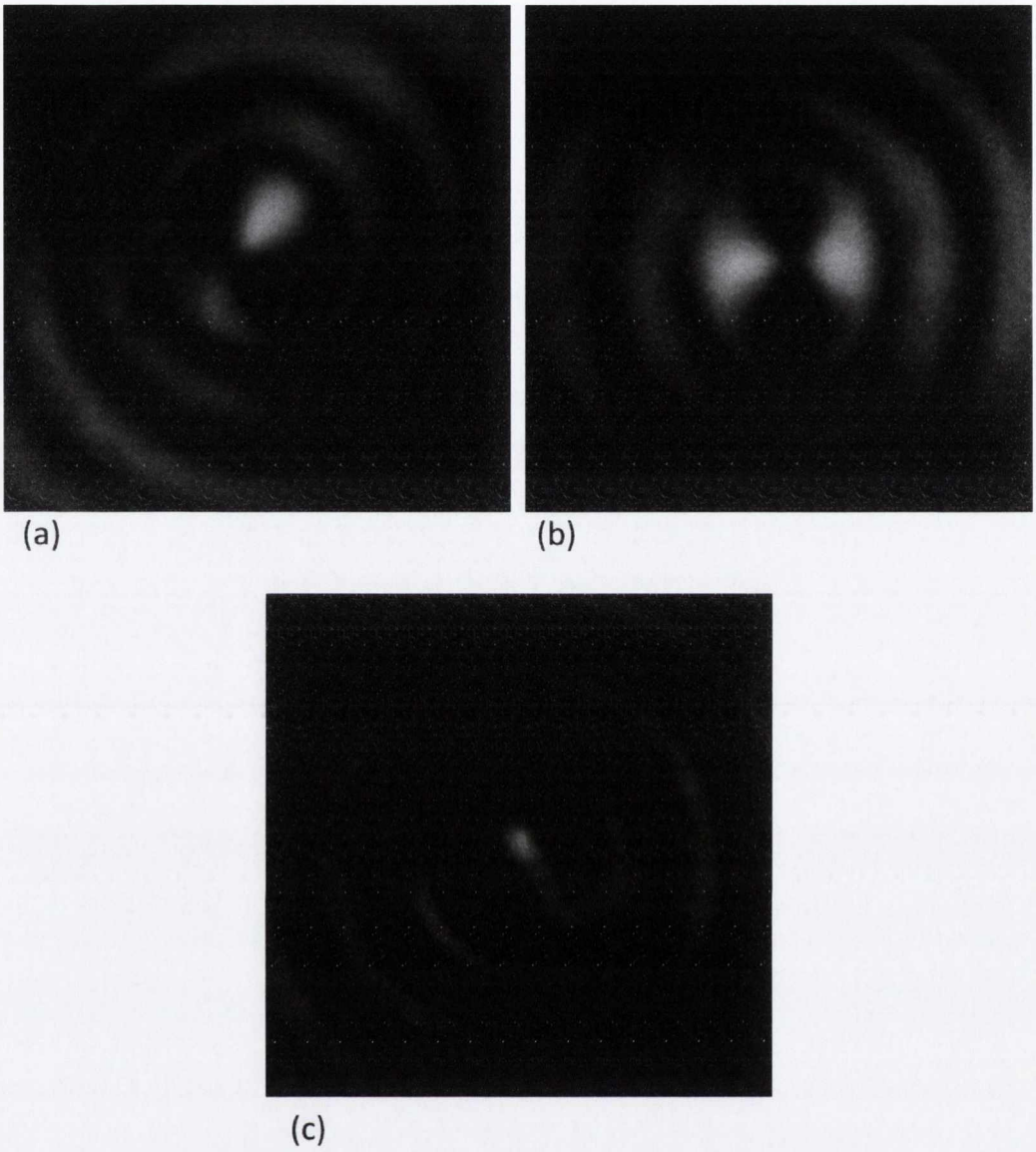

Figure 4.3.17: The Stokes parameters measured for the radially polarized beam. Using the definition 4.3.1 (a) shows S_2; (b) shows S_1 and (c) shows S_3.

Referring to Figure 4.3.17 (c), it is seen that the beam retained a small circularly polarized component. This could presumably be eliminated with a more stable optical bench since the intensity profile depends more sensitively on phase in this experiment than in the other method.

Chapter 5. Two-photon polymerization of ring, wall and pillar structures

In this Chapter we make use of the shape of the conically diffracted beam to write micron and sub-micron scale structures via two photon polymerization. The advantages of using beams with Bessel-like intensity profiles for two-photon polymerization are discussed in Section 5.1. The experimental setup is introduced in Section 5.2 and the associated geometrical optics is outlined. In Section 5.3 the results of the two-photon polymerization experiment, including polymerized ring, pillar and wall structures, are presented and discussed. Structures written with the B_1 beam are also reported on.

5.1. Two-photon polymerisation with Bessel like beams

Two-photon polymerisation (TPP) of liquid and sol-gel resins is a well established method used for fabrication of a wide range of three-dimensional structures with sub-micron critical dimensions (Park, Yang, & Lee, 2009). The rate of two-photon polymerisation depends upon the rate of two-photon absorption. Since this is proportional to the square of the light intensity it follows that structures can be written with a higher resolution than with photo-polymerisation based on single photon absorption (Maruo, Nakamura, & Kawata, 1997), (Park, Yang, & Lee, 2009). For some applications of TPP, such as writing wall structures, the process efficiency can be improved if the focussed laser beam has a large depth of focus, such as in a zero order Bessel beam. In that case polymerisation occurs simultaneously at different depths without the need to translate the focal point or the sample along the beam axis (Bhuian, Winfield, O'Brien, & Crean, 2007). The Bessel beam comprises a central spike surrounded by concentric rings, with the property that the optical power in each ring is equal (Durnin, Miceli, & Eberly, 1987), (Herman & Wiggins, 1991). For the zero order Bessel beam the overall optical power can be chosen such that there is negligible TPA in the rings as compared to the on-axis spike (Figures 5.1.1 and 5.1.2). To see why this is, consider a beam with total power P. Say there are n rings, then the power density of the central spot is roughly $P/\pi s^2$. The power density of the m^{th} ring is $P/2\pi^2 m s^2$ (Here we have written the radius of the m^{th} ring as

πms). The TPA density is $P^2/\pi^2 s^4$ in the spot compared to $P^2/4\pi^4 m^2 s^4$ in the ring. It follows that the TPA density in the spot is approximately $4\pi^2 m^2$ times that in the m^{th} ring.

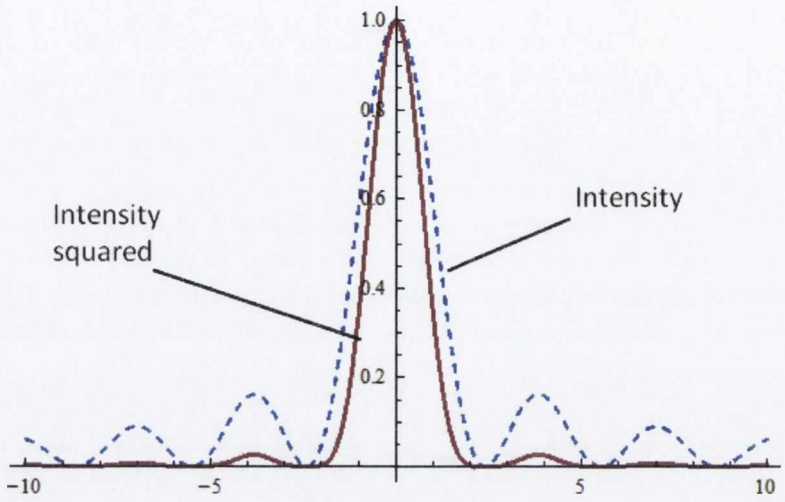

Figure 5.1.1: The intensity squared (TPA) profile of a zeroth order Bessel beam compared to its intensity profile (dashed line).

Bhuian et al formed the zero order Bessel beam using an axicon and imaged it with a high power objective into the resin to write microwires (Bhuian, Winfield, O'Brien, & Crean, 2007). By laterally translating the sample in the Bessel region, wall and grid structures with wall thickness of 1 μm and wall height 20 μm were written (Li, Winfield, O'Brien, & Crean, 2009). In the focal plane of the objective a narrow ring profile is formed (i.e. an image of the far field profile of the non-diverging region); this was used to write thin ring-shaped structures without the use of motorized translation stages. Conical diffraction, as we have described in section 2.3, offers an alternative method for the transformation of a Gaussian beam to a Bessel beam.

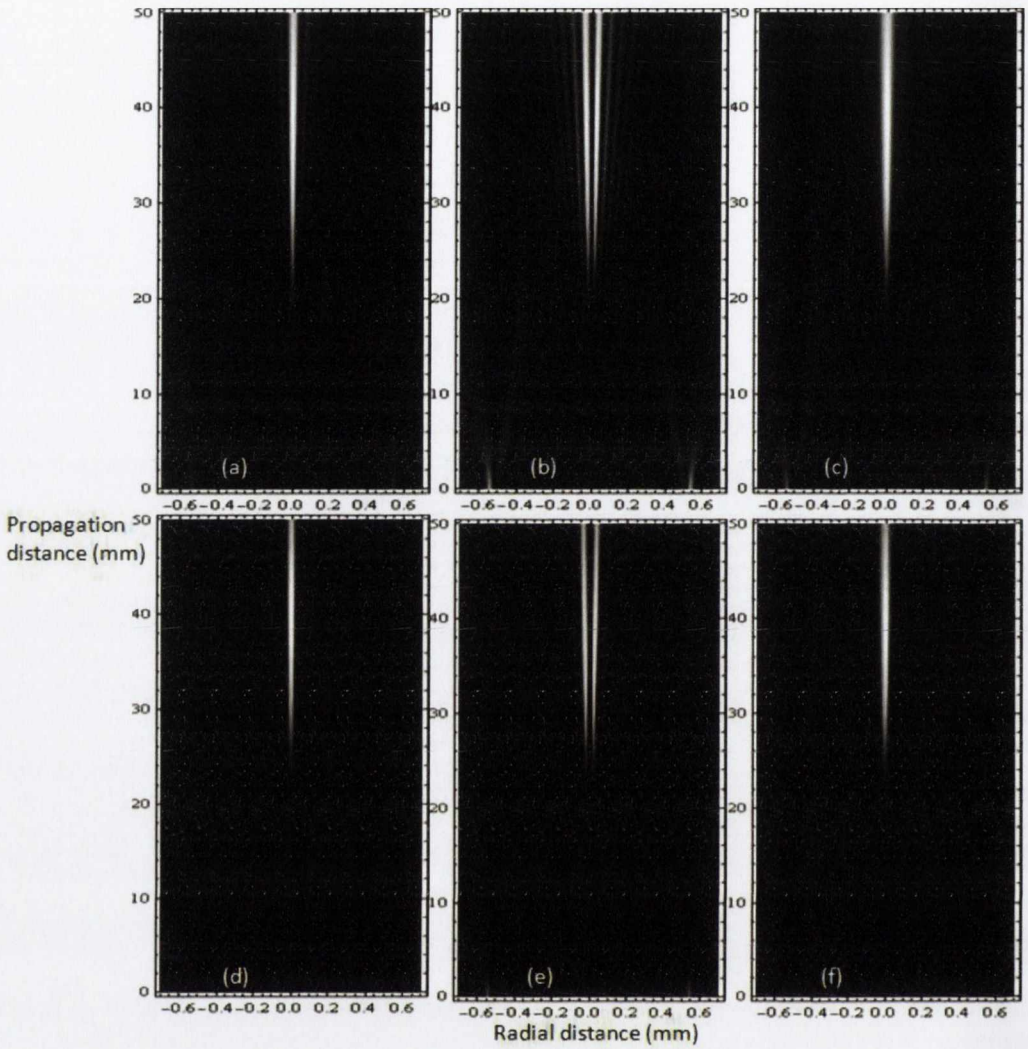

Figure 5.1.2: A comparison of the intensity and two photon absorption (intensity squared) profiles of the conically diffracted beam. Parts (a), (b) and (c) show the intensity profiles of the zeroth order, first order and composite beams respectively. Parts (d), (e) and (f) show the TPA profiles of the zeroth order, first order and composite beams respectively.

5.2. Experiment

The optical setup used to form the non-diverging Bessel beam and image it into the resin is shown in Figure 5.2.1.

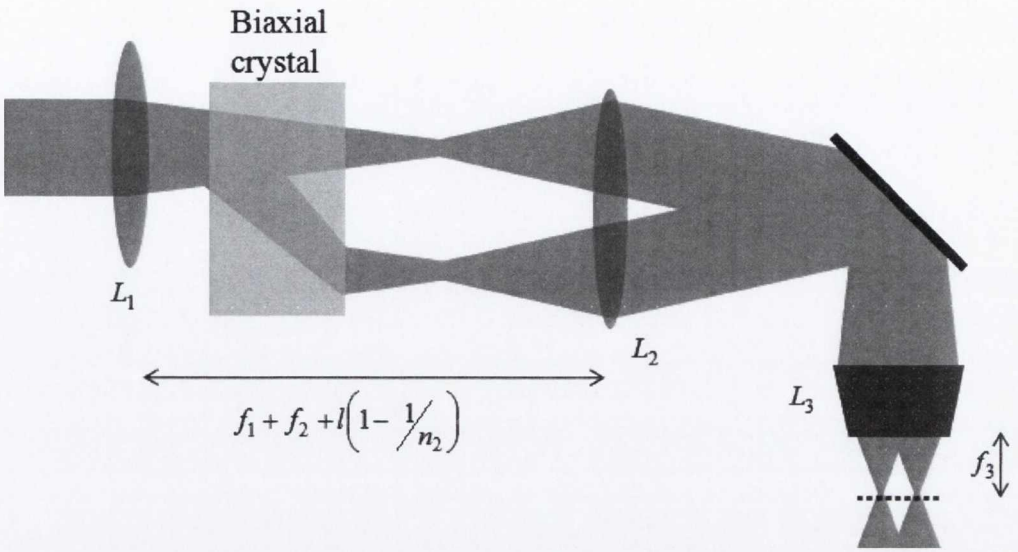

Figure 5.2.1: The optical arrangement used to form a beam beyond the objective (L_3) with a ring profile at the focal plane (of L_3) and a Bessel like profile at either side of it. In the diagram the ring is focused on the sample (dashed line beneath L_3) with the Bessel region being formed beneath.

The optical source used was a Ti: sapphire laser (Spectra Physics Mai Tai) with 100 fs pulse width and wavelength 795 nm. The repetition rate was 80 MHz and the average power measured at the laser was 750 mW. A converging lens L_1 with focal length f_1 = 10 cm was used to focus the laser beam to a Gaussian spot with a $1/e^2$ radius ω = 50 μm. The biaxial crystal was placed between the lens and the beam waist to minimise the optical intensity in the crystal (Figure 5.2.1). The crystal used was a 30 mm long slab of $KGd(WO_4)_2$ cut perpendicular to one of the optic axes. At the laser wavelength the principal refractive indices are: $n_1 = 2.01183, n_2 = 2.04235, n_3 = 2.09528$. Thus for this wavelength our cone of refraction has the semi-angle A = 0.019 radians and the geometrical ring radius of the emergent cylinder is R_0 = 0.57 mm. Figure 5.2.2 shows a numerical simulation of the beam profile in the FIP using the experimental parameters just mentioned.

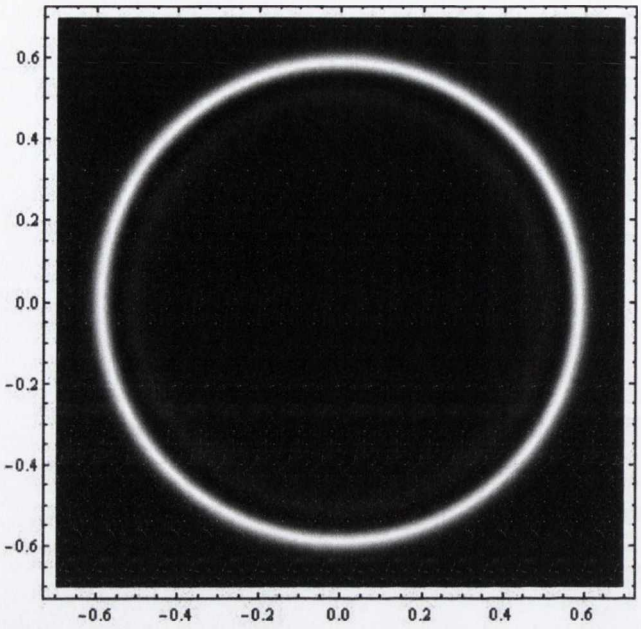

Figure 5.2.2: A simulation of the beam profile that occurs at the back focal plane of L_2. This double ring approximates a ring of point sources that are focused by L_2 into a converging cone of waves.

The second converging lens L_2 (f_2 = 20 cm) was positioned such that the FIP lies at its back focal plane and a non-diverging Bessel beam is formed in the region of the focus on the other side of the lens. The is analogous to the formation of a zero order Bessel beam using a annular aperture located at the back focal plane of a converging lens, as described in (Durnin, Miceli, & Eberly, 1987)except that our non-diverging beam is a superposition of zeroth & first order Bessel beams.

A ×100 oil immersion microscope objective (L_3) was used to form a de-magnified image of the Bessel beam in a sol-gel resin sample placed on the underside of a 170 μm thick glass slide, as shown in Fig. 5.2.3. This de-magnified image of the Bessel beam is not quite non-diverging; rather it diverges with a semi-angle of ~4^0. The distance d_{23} between L_2 and L_3 was 23 cm (The reason for the specific distance of 23 cm was the limited available space on the optical bench). The minimum radius of the de-magnified central spot of the 0^{th} order beam is:

$$r = {}^{1}/_{M}\left({}^{2.405}/_{(k_0 \sin\theta)}\right) \qquad 5.2.1.$$

where M is the magnification of the objective, k_0 is the wave-number of 795 nm wavelength light in free space and

$$\theta = \tan^{-1}\left({}^{R_0}/_{f_2}\right) \qquad 5.2.2.$$

is the semi-angle of the conical superposition of wave-vectors produced by lens L_2. A de-magnified image of the FIP is formed at the focus of the objective and the diameter, *d*, of that ring-shaped profile is:

$$d = 2R_0 \times {}^{f_3}/_{f_2} \qquad 5.2.3.$$

which, for our setup, gives a value of 9.12μm.

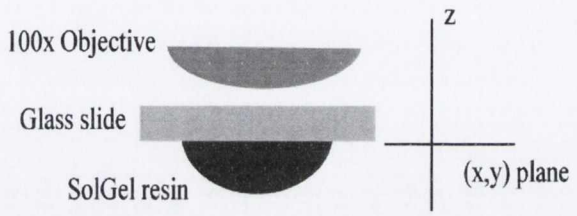

Fig. 5.2.3 A schematic showing the relative positions of the objective, glass slide and sample. The glass slide is movable in the x & y directions. The objective can be moved in the z direction to switch between the ring and Bessel regions for polymerisation. We use the convention of setting z=0 when the ring is focused on the glass-sample interface.

The position of the glass slide (plus resin) in the x- and y-directions and the objective in the z-direction were controlled using computerised translation stages as shown in Fig 5.2.3. The objective could be positioned so that either the ring-shaped beam or the Bessel-like beam lies in the resin. Both of these positions were used for writing microstructures.

It is notable that since the distance d_{23} between L_2 and L_3 is (in the experiment) only marginally longer than the focal length of L_2, the double peaked non-diverging region described earlier (section 2.3) does not form between L_2 and L_3. Hence beyond L_3 we will have an axial intensity peak on either side of the ring plane. Had both axial intensity peaks of the non-diverging beam been formed between L_2 and the back focal plane of L_3 we would have beyond L_3 a ring profile diffracting into a double peaked axial profile. Figure 5.2.4 (a) shows the geometrical optics of the setup we used in the experiment. Figure 5.2.4 (b) shows the geometrical optics of an arrangement with the distance between L_2 and L_3 sufficiently large so as to allow the double peaked non-diverging region to occur.

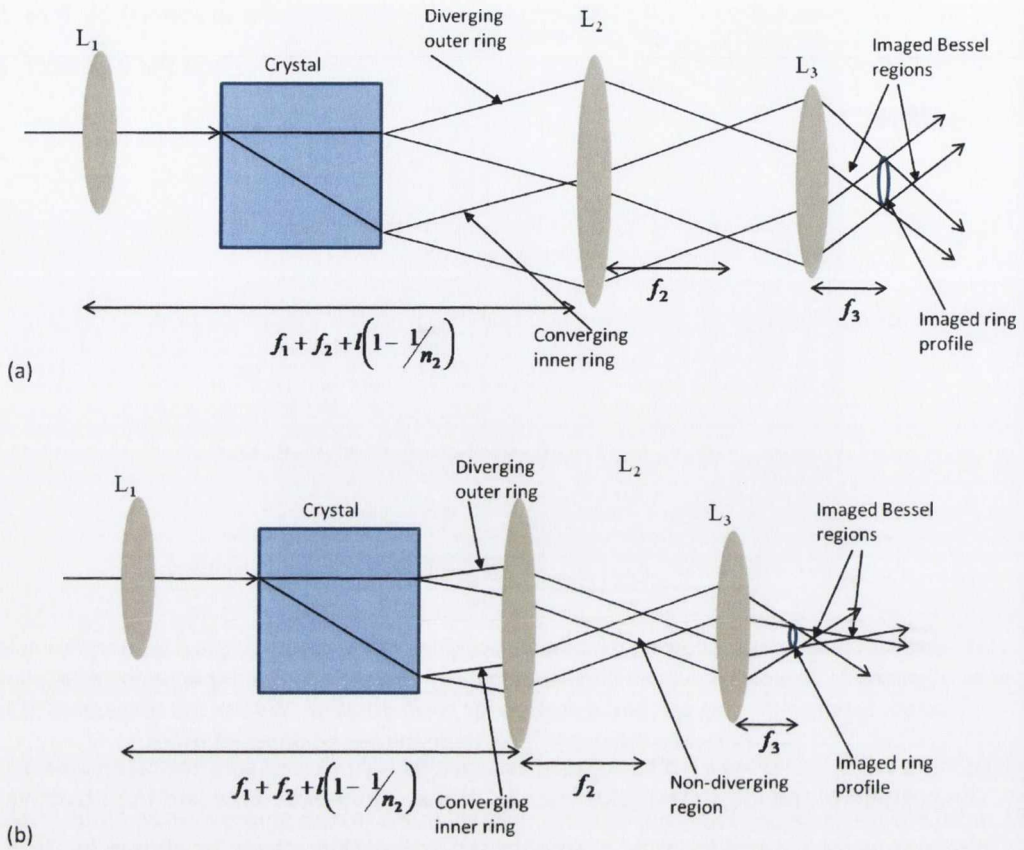

Figure 5.2.4: (a) A schematic of the optical arrangement used in the experiment showing the formation of the two "Bessel" regions on either side of the ring plane beyond the objective (L_3). (b) An alternative setup with the double peaked non-diverging being allowed to form between L_2 and L_3 leads to both Bessel regions being imaged beyond the focal plane (ring profile) of the objective.

Figures 5.2.5 ((a) & (b)) show ray trajectories near the focal plane of the objective (L_3) corresponding to both cases depicted in Figures 5.2.4 ((a) & (b)). In these ray diagrams that show the formation of the ring and quasi Bessel regions beyond L_3 the ray positions and directions were calculated using ray transformation matrices for the experimental parameters. The initial rays were assumed to lie on two concentric rings separated by a distance of ω with the outer ring diverging and the inner ring converging. This was intended to approximate the FIP profile. The initial location of the two concentric rings was the back focal plane of L_2. The intensity plots shown alongside the ray diagrams were generated from the ray diagrams by associating an intensity and phase with each ray and summing their contributions.

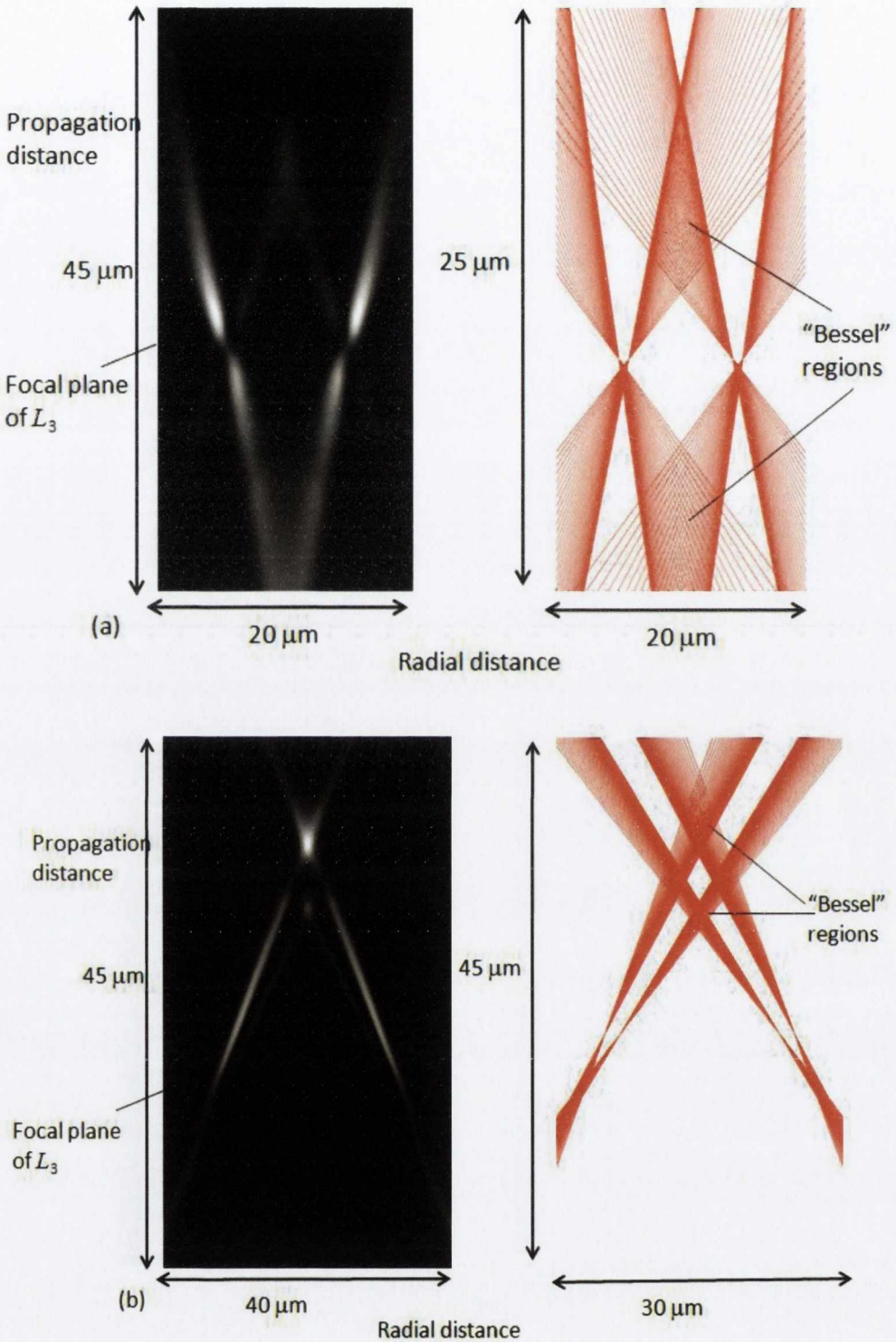

Fig 5.2.5: (a) Rays, represented by red lines, are focused to form a double ring at the focal plane of the objective with an image of the non-diverging Bessel beam (regions where rays intersect on-axis) on either side. **(b) The ring profile is again formed at the objective's focal plane but now** both peaks of the non-diverging region are imaged beyond the ring plane. The black and white diagrams alongside the ray diagrams are intensity plots generated from the ray diagrams.

The preparation of the sol-gel resin has been described previously (Bhuian, Winfield, O'Brien, & Crean, 2007). Essentially, a precursor containing 5 mol% Zr was prepared by hydrolysis of an organo-silane to which chelated zirconium alkoxide was added. Condensation reactions were promoted between the hydrolised precursors by the addition of water. The photo-initiator used was 4,4′-bis(diethylamino) benzophenone (2% by weight) which has a high absorption cross-section at 400 nm. The sol-gel was allowed to dry on the glass substrate before inverting and mounting on the translation stage. The photo-polymerisation process was monitored *in situ* using a CCD camera. The exposure time was varied using an optical shutter and was typically in the range of 10 ms to 1s. The distance between the objective and the glass slide was also varied to explore the range of possible structures. Designating the position of the objective at which the ring profile is in focus on the glass-resin interface to be $z = 0$ (Figure 5.2.3), structures were written at $z = 0$, 5, 10, 15 and 20 μm as the objective was moved away from the glass slide. Grid patterns with sub-micron thick walls were written by translating the sample in the x and y directions at constant speeds of 0.005 mm s^{-1} in the Bessel region of the beam. After photopolymerisation the excess resin was washed away using isopropyl alcohol. A Zeiss He ion microscope and a Zeiss SEM were used to examine the polymerised microstructures.

5.3. Results and discussion

An overview of the main results of our experiment, as well as the potential of the conically diffracted beam for two-photon polymerisation, can be most easily gained by taking a look at Figure 5.3.1 which shows a plan view of the structures formed using the optical setup described in section 5.2. The exposure times increase from 75 ms to 1000 ms from bottom to top and the position of the glass-resin interface increases from zero to 25 μm (keeping in mind the measurement convention introduced in the previous section) from left to right.

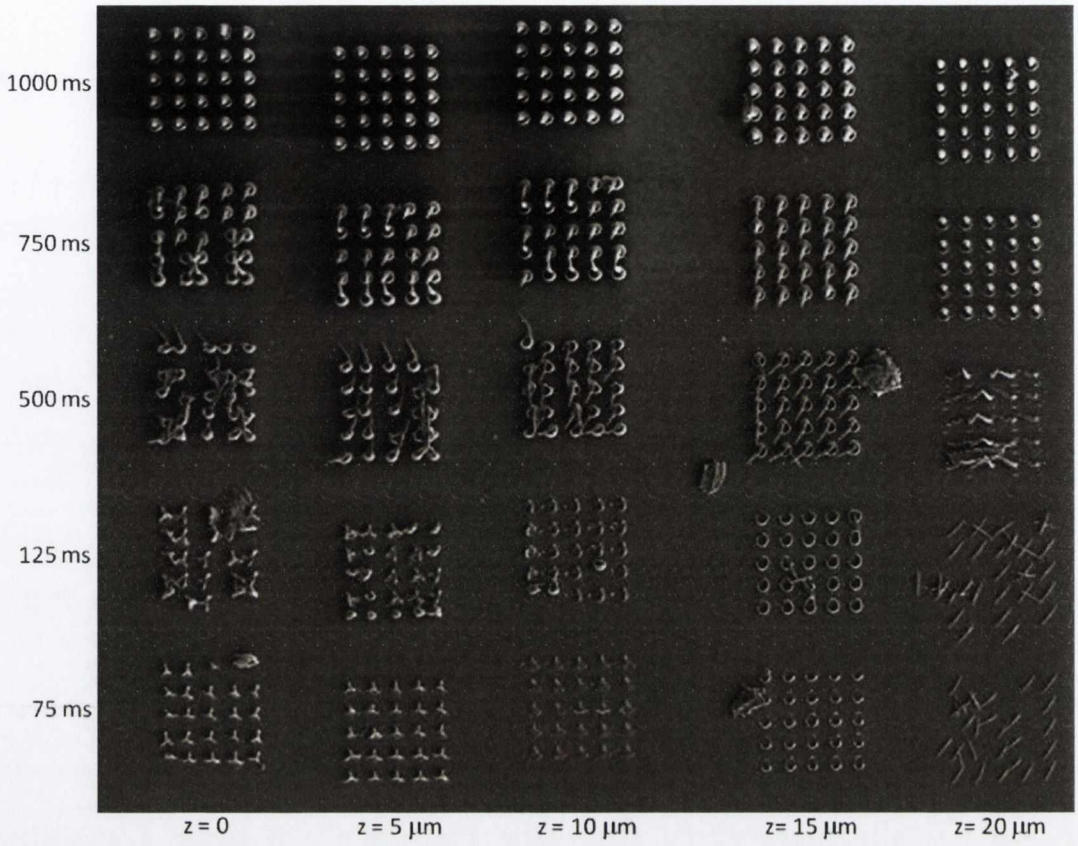

Figure 5.3.1: An SEM image showing all the polymerised structures written at five different focus depths and five different exposure times. For a given exposure time and focus depth there is a 5 x 5 square array of polymerised structures.

The structure in Figure 5.3.2 was written with a large exposure time (1s).This structure is interesting insofar as it displays roughly the shape of the beam in the region of the ring plane. We can see the shape of both the ring plane and the Bessel regions on either side of the ring plane on this structure.

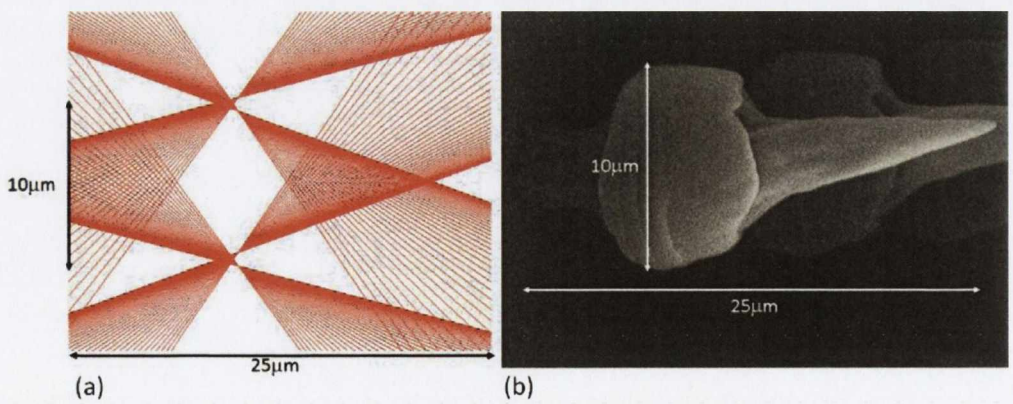

Figure 5.3.2: (a) A ray diagram showing the formation of the ring and Bessel regions beyond L_3 and (b) the structure that was formed by exposure to this beam. The image on the right was taken at a tilt of 30° to the horizontal axis. The 25 μm scale on the image on the left takes this tilt into account and measures the real dimension of the object.

Figure 5.3.3 shows He-ion microscope images of microstructures written at the position of the objective with the image of the FIP in focus at the resin/glass interface (z = 0). The exposure times for these structures were (a) 1 s, (b) 500 ms and (c) 125 ms. Since the beam is ring-shaped at this position, the part of the microstructure connected to the glass slide is cylindrical. For high exposure times the Bessel region beyond the ring plane also contributes to the structure. As the exposure time is decreased the Bessel "pillar" detaches from the ring until it becomes so small that it is washed away with the un-polymerised material during development. The diameter of the polymerised ring is ~8 μm as compared to the expected value of 9.1 μm from equation 5.2.3. It seems that the ring structure is not sufficiently robust to be self-supporting (Figure 5.3.3(c)) and has partially collapsed, making it difficult to estimate the thickness of the cylinder wall. However it seems to be ~0.4 μm, which may explain its fragility. Its thickness was estimated to be 0.5μm by applying equation 5.2.3 to the ring thickness rather than radius and measuring the thickness from the intensity plot in Fig 5.2.2.

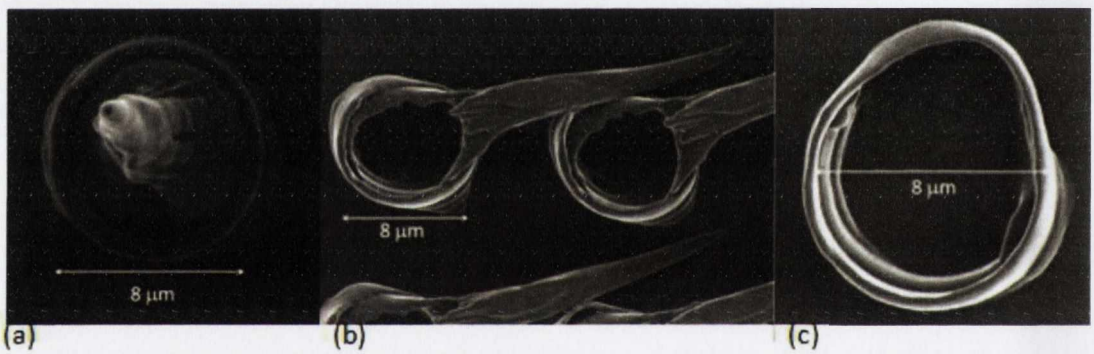

Figure 5.3.3: The structures written by focusing the ring plane on the glass resin interface. The exposure times were (a) 1 s, (b) 500 ms and (c) 125 ms.

Figure 5.3.4 shows an image of an array of pillar microstructures formed when the objective was positioned at z = 10 μm. The image was recorded by viewing the sample at 45^0 above the plane of the slide. The exposure time for these structures was 125 ms, which corresponds to 10^7 laser pulses. The pillars are self-supporting and anchored on the glass slide and are very reproducible. The pillars are 9.4 μm long and taper from 1.3 μm at the base on the glass slide to 0.7 μm near a rounded apex.

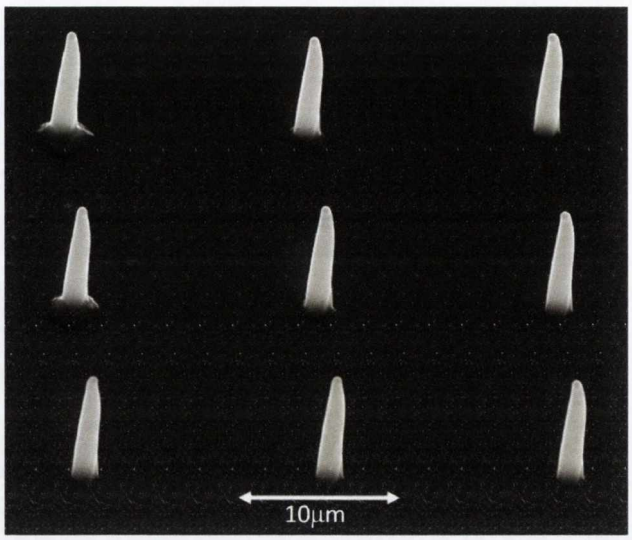

Figure 5.3.4: Pillars written using the Bessel region of the focussed beam. Viewing angle was 45^0 above the plane of the glass slide. The exposure time for these pillars was 125 ms.

The dependence of pillar height on exposure time at z = 20 μm was measured. As the exposure time was increased up from zero to 200 ms the pillar height increased steadily reaching a value of ~10 μm at 200 ms. Above 200 ms the dependence of pillar height on exposure time was much weaker. This saturation behaviour is probably due to the fact that the length of imaged Bessel region that occurs beyond the ring plane is in the region of 10 μm (see Figure 5.3.2). Outside this region the on axis intensity should be weak. The pillar height as a function of exposure time is plotted in Figure 5.3.5.

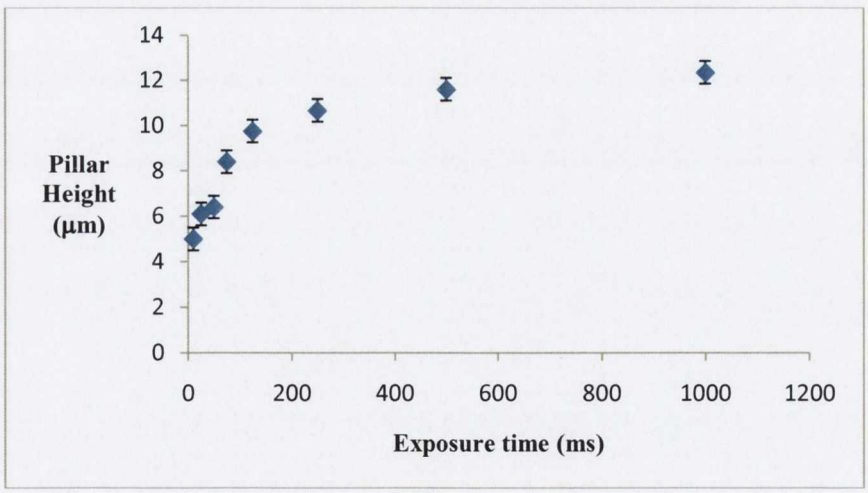

Figure 5.3.5: The height of the polymerised pillars as a function of exposure time. Each pillar considered was polymerised at z = 20 μm.

A grid structure with 2.5 μm period was written by translating the sample in the x and y directions with a velocity of 0.005 mm s^{-1} while maintaining the glass/resin interface 20μm beyond the ring plane. The grid walls were less than 0.5 μm thick near the top but are wider near the base (Figure 5.3.6), in a manner similar to the pillars in Figure 5.3.4.

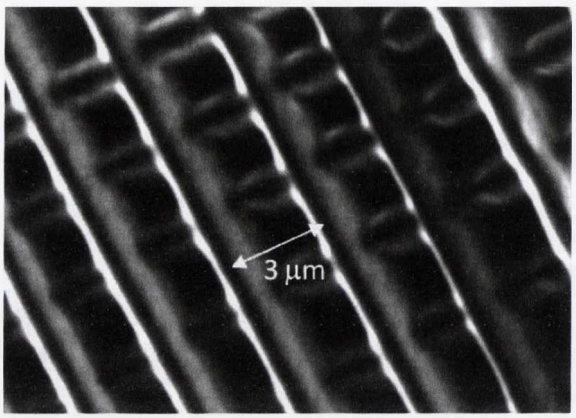

Figure 5.3.6: Grid structure with a period of 3 μm. This grid was written at a velocity of 0.005 mm s^{-1}.

Two photon polymerisation using the 1st order Bessel profile

As mentioned earlier, the major differences between a non-diverging beam formed by conical diffraction and one formed by the axicon or annular slit methods are that the non-diverging beam formed by conical diffraction has a double peaked axial profile (related to the fact that a double ring is collimated into a cone of rays) and that it is a superposition of 0th and 1st order Bessel beams.

As well as using the composite beam for TPP, we also used each component beam separately. We were particularly interested in the effect of the 1st order Bessel region on the sol-gel resin as its spatial structure (Figure 5.1.2) suggests that it could be used to polymerise tube like structures with sub-micron diameter.

The experimental layout for TPP with the 1st order beam was the same as that shown in Figure 5.2.1 except for a circular polarizer consisting of a quarter wave plate and Glan-Taylor polarizer (a type of linear polarizer made of two right angled prisms which has the effect of splitting a circularly polarized beam into its linear components) which was used to select the 1st order component. The sol-gel was exposed to the laser for durations of ranging between 10ms and 1s.

Images of the objects polymerised by the 1st order beam are shown in Figure 5.3.7. The objects formed by the imaged 1st order Bessel beam resemble the pillar structures formed by the composite beam. There is, however, a feature on each pillar that we can positively identify as being related to the shape of the B_1 beam. That feature is an indentation on the top of the pillars due to the axial intensity zero of the B_1 beam.

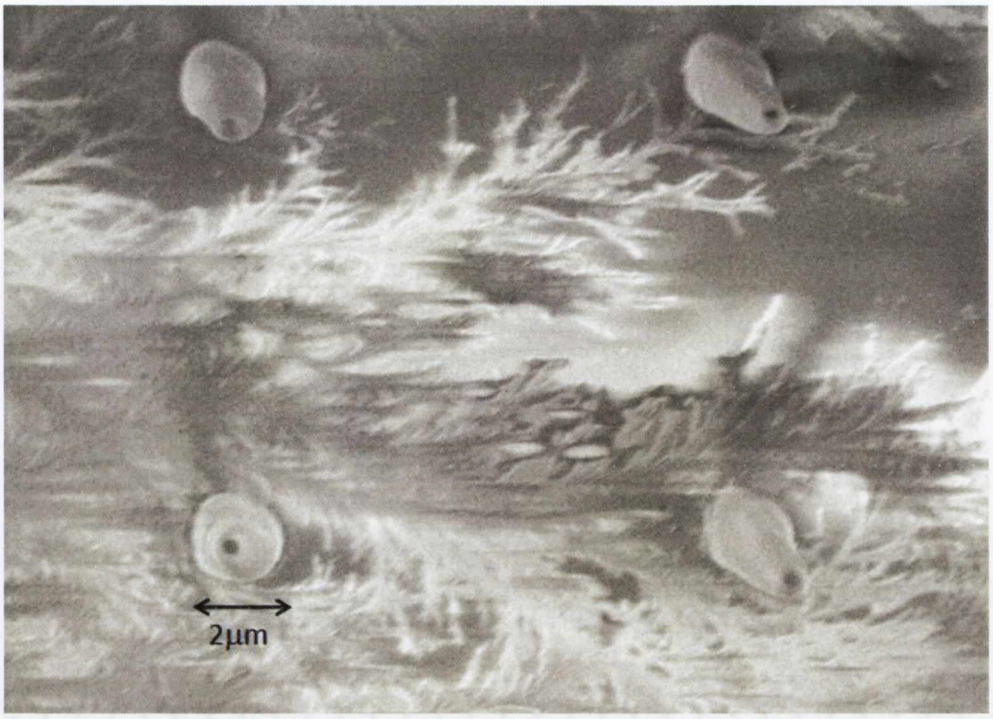

Figure 5.3.7: Four pillars formed by the 1st order beam showing what appears to be a slight indentation that could be due to the zero on-axis intensity of the 1st order beam.

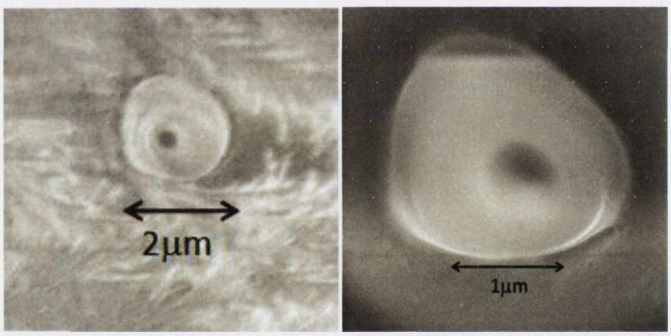

Figure 5.3.8: Close up images of the pillar in the bottom left corner of Fig 5.3.7. It appears that the tube would have a diameter of around 500 nm if it were properly formed.

Concluding remarks

The paraxial theory of conical diffraction has been shown to imply that conical diffraction, in combination with various simple optical arrangements, serves as a powerful beam shaping tool. Conical diffraction has been used to transform both the polarization and amplitude distributions of standard Gaussian beams leading to the generation of a wide range of commonly used laboratory beams. These transformations make extensive use of the dependence of the conically diffracted beam on incident beam waist and polarization and the fact that the conically diffracted beam can, for the case of circularly polarized incident light, be separated into two orthogonally polarized components, one of which contains an optical vortex.

Beams with novel and interesting intensity profiles have also been generated using the cascade arrangement discussed in chapter three. Some of these beams are already finding applications in optical trapping here in Trinity College Dublin that take advantage of the intensity distribution of the focal image plane profile generated by a cascade of two crystals of equal lengths. For these optical trapping applications, the dependence of the intensity distribution (and, hence gradient force distribution) on the polarization of the incident beam is used to trap and translate particles with sizes of the order of the ring thickness. In two crystal conical diffraction it is relatively easy to switch between different beam shapes, which should facilitate new possibilities in optical trapping.

Many more possibilities involving the cascade arrangement remain to be investigated. For example, the cascade beam could easily be converted into a radially polarized beam by propagation through an interferometer, as was done for the once conically diffracted beam in Chapter 4. Collimating the cascade conically diffracted beam into a converging cone of rays could form a non-diverging beam with several on axis intensity peaks (resulting from the on-axis interference pattern discussed in Chapter 3). Higher order non-diverging Bessel beams can also be produced using the cascade arrangement.

The conically diffracted Gaussian has been shown to be capable of writing similar micron and sub-micron scale structures to those that can be written with an imaged axicon beam as well as structures resembling the shape of the first order beam profile while possessing the advantage of easy transformation between zeroth and first order beam profiles. More

extensive experiments to test the usefulness of the various beams shaped by cascade conical diffraction in two photon polymerization are required.

In recent years conical diffraction has been receiving renewed interest in recent years from other research groups as well, with Peet et al demonstrating the conversion of Gaussian beams into LG_{01} and LG_{02} with both single crystals and two crystals in cascade (Peet, 2010(b)), (Peet, 2010(a)), (Peet & Zolotukhin, 2010). Abdolvand et al are have demonstrated a laser that emits a conically diffracted beam (a conically diffracted Gaussian in their experiments since they used a Gaussian pump beam) (Abdolvand, Wilcox, Kalkandjiev, & Rafailov, 2010). The gain medium for this laser is a slab of Nd:$KGd(WO_4)_2$. The operation of the laser is based on the result that a beam that is conically diffracted, then reflected back along its original path, is transformed back into the same beam. The demonstration of Abdolvand et al has opened up the possibility of developing lasers that emit beams with any of the beam shapes and polarization distributions that can be generated with cascade conical diffraction.

As mentioned in chapter 3, the cascade conically diffracted beam, in the case of two crystals of equal length, contains both spin and orbital angular momentum. The ratio of spin to orbital angular momentum in the beam is directly related to the relative rotation angle of one of the crystals and, thus, is easily controlled. This has obvious optical trapping applications.

It seems likely, then, that the unique polarization and the novel beam shapes that can be generated using conical diffraction will lead to the production of other novel beam shapes and the development of their applications in the future.

Appendix

A: Orbital angular momentum of the conically diffracted Gaussian

In section 2.1 it was mentioned that the conically diffracted Gaussian beam has orbital angular momentum of ½ħ per photon. It was shown in section 1.4 that the conically diffracted field has the form. If the incident beam is left circularly polarized it can be written:

$$\vec{E}(r,\phi,Z) = B_0(r,Z)\vec{e}_+ + e^{i\phi}B_1(r,Z)\vec{e}_- \qquad \text{A1}$$

where $\vec{e}_+/\vec{e}_-$ are the polarization vectors for left/right circular polarization. This describes a superposition of beams with one ($e^{i\phi}B_1(r,Z)$) having an azimuthal phase dependence, embodied in the $e^{i\phi}$ term, and a beam with no azimuthal phase dependence ($B_0(r,Z)$). It has been shown (Allen, Barnett, & Padgett, 2003) that in the case of a circularly symmetric beam, an azimuthal phase factor of the form $e^{i\phi}$ implies that the beam carries ħ OAM per photon. The effect of the azimuthal phase term on the beam's wave-front can be observed experimentally by interfering the conically diffracted beam with a plane wave and observing the resulting interference pattern. This can easily be done in the lab with a Mach-Zehnder interferometer. Figure A.1 shows a simulation of the interference pattern resulting from superimposing the B_1 beam generated from a Gaussian beam with a waist of 40 μm with a Gaussian with a waist of 0.5 mm.

Figure A.1: The interference pattern generated by interfering the B_1 beam with a Gaussian in the region of the central ring of B_1 beam in the far field.

The fork shape at the centre of the interference pattern is indicative of the presence of a 2π azimuthal phase change. The fact that the interference fringes are closer together above the centre of the beam to below it is because the helical wave-front is inclined to the x axis, locally, in the same sense as the plane wave above the centre of the beam and in the opposite sense below.

B: Images referred to in Chapter 3

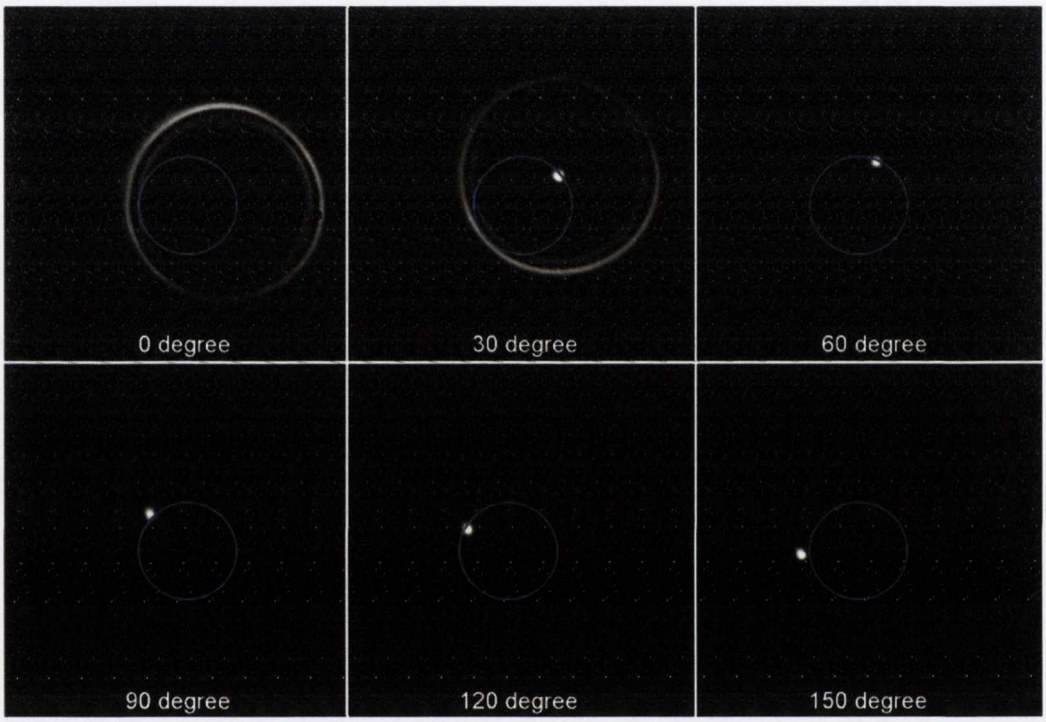

Figure B.1: Diagram showing how the position in the transverse plane of the centre of the beam that emerges from a two crystal cascade (identical crystals) rotates on a circle with the radius equal to the geometric ring radius associated with each crystal (blue ring).

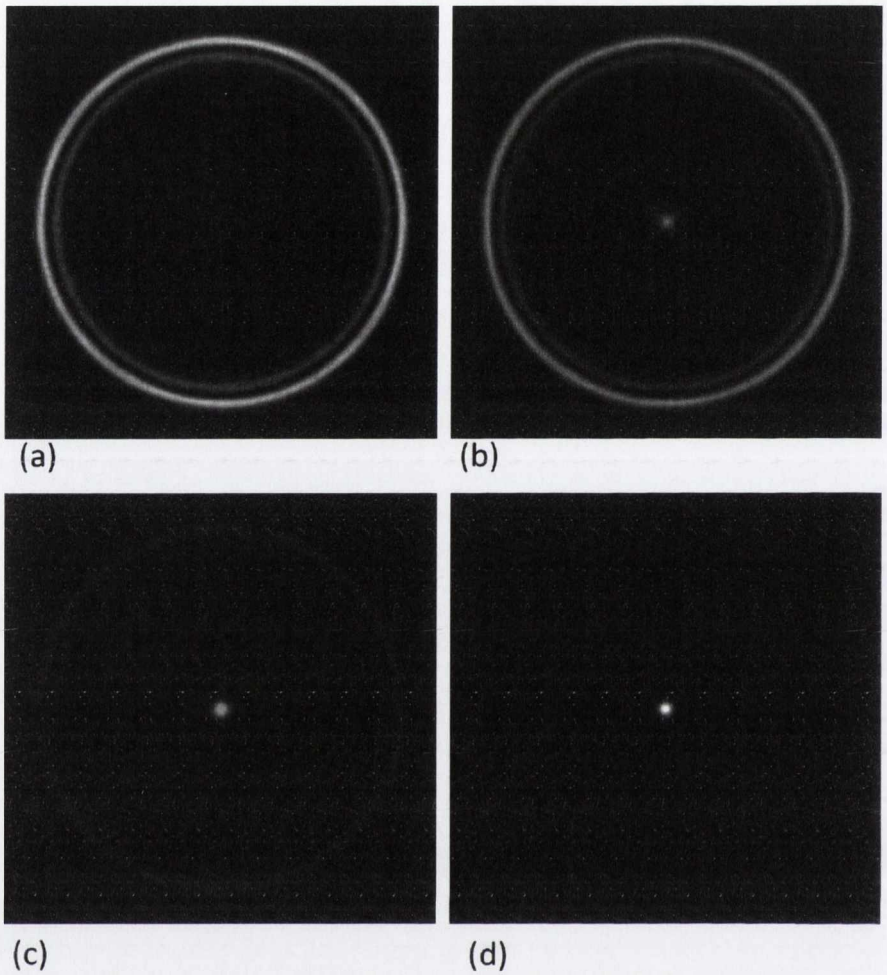

Figure B.2: Smoothed FIP cascade images (a): α=0°; (b): α=15°; (c) α=30°; (d) α=180°. These images were used for the comparison of experiment with theory in Figures 3.3.3 and 3.3.4.

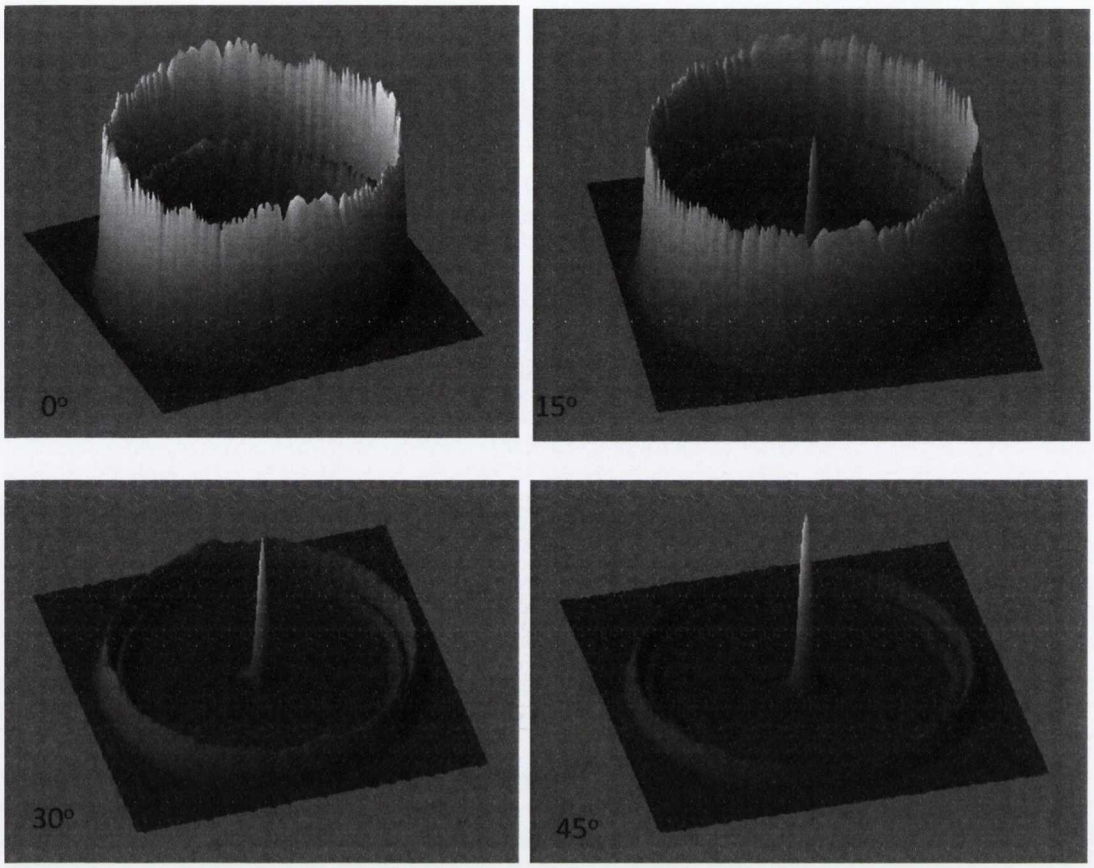

Figure B.3: Surface plots of the beams generated from a two crystal cascade with the relative rotation between the crystals indicated on each image.

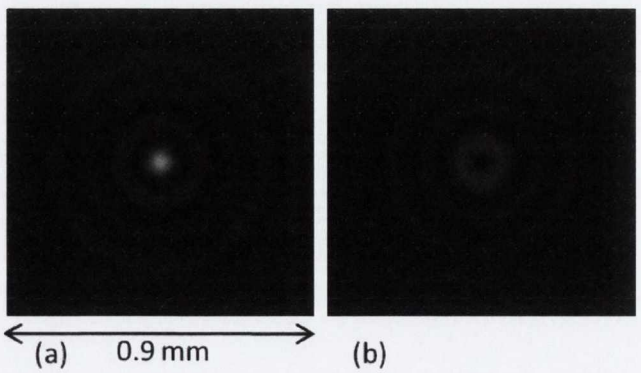

Figure B.4: Smoothed far field cascade with $\alpha = 45^{\circ}$ images used in the comparison of experiment with theory in Figure 3.3.9.

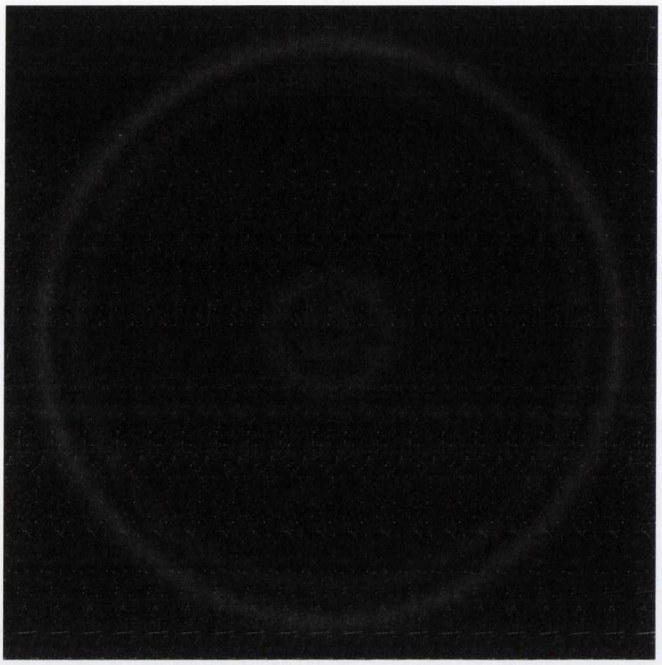

Figure B.5: Smoothed FIP image of the cascade beam with two crystals with geometric ring radii with the ratio of 3:2 and a relative rotation of 45°.

C: Glossary of abbreviations

CR: Conical refraction

ICR: Internal conical refraction

CD: Conical diffraction

CCD: Cascade conical diffraction

FIP: Focal image plane

LG: Laguerre-Gaussian

HG: Herrmite-Gaussian

HB: Hermite-Bessel

SAM: Spin angular momentum

OAM: orbital angular momentum

HWP: Half wave plate

LP: Linear polariser

NDF: Neutral density filter

BSM: Beam splitting mirror

TPA: Two photon absorption

TPP: Two photon polymerisation

References

Abdolvand, A., Wilcox, K. G., Kalkandjiev, T. K., & Rafailov, E. U. (2010). Conical refraction Nd: $KGd(WO_4)_2$ Laser. *Optics Express , 18* (3), 2753-2759.

Allen, L., Barnett, S. M., & Padgett, M. J. (2003). *Optical angular momentum.* Bristol: Institute of Physics publishing.

Arnaud, J. A. (1976). *Beam and fiber optics.* Academic Press.

Bartholin, E. (1669). Experimenta crystalli Islandici disdiaclastici: Quibus mira & insolita refractio detegitur. Hafnia/Copenhagen

Belskii, A. M., & Khapalyuk, A. P. (1978(a)). Internal conical refraction of bounded light beams in a biaxial crystal. *Opt. Spectrosc. , 44*, 436-439.

Belskii, A. M., & Khapalyuk, A. P. (1978(b)). Propagation of confined light beams along the beam axes (axes of single ray velocity) of biaxial crystals. *Opt. Spectrosc. , 44*, 312-315.

Belsky, A. M., & Stepanov, M. A. (1999). Internal conical refraction of coherent light beams. *Opt. Commun. , 167*, 1-5.

Berry, M. V. (2004). Conical diffraction asymptotics. *J. Opt. A: Pure Appl. , 6*, 289-300.

Berry, M. V. (2010). Conical diffraction from an N-Crystal cascade. *J. Opt. , 12*, 075704 (8pp).

Berry, M. V., & Dennis, M. R. (2003). The optical singularities of birefringent dichroic chiral crystals. *Proc. R. Soc. A , 459*, 1261-1292.

Berry, M. V., & Jeffrey, M. R. (2007). Conical diffraction: Hamilton's diabolical point at the heart of crystal optics. *Progress in Optics , 50*, 13-50.

Berry, M. V., Jeffrey, M. R., & Lunney, J. G. (2006). Conical diffraction: Observations and theory. *Proc. R. Soc. A , 462*, 1629-1642.

Berry, M. V., Jeffrey, M. R., & Mansuripur, M. (2005). Orbital and spin angular momentum in conical diffraction. *J. Opt. A: Pure Appl Opt , 7*, 685-690.

Bhuian, B., Winfield, R. J., O'Brien, S., & Crean, G. M. (2007). Pattern generating using axicon lens beam shaping in two-photon polymerisation. *Appl. Surf. Sci , 254*, 841-844.

Born, M., & Wolf, E. (2001). *Principles of optics* (7th ed.). Cambridge University Press.

Brosseau, C. (1998). Part 1 Historical survey of understanding of polarized light. In C. Brosseau,

Fundamentals of Polarized Light (pp. 1-9). John Wiley and Sons.

Buchwald, J. Z. (1989). *The rise of the wave theory of light.* The University of Chigago Press.

Deschamps, G. A. (1971). Gaussian beam as a bundle of complex rays. *Electron. Lett. , 7* (23), 684-685.

Dreger, M. A. (1999). Optical beam propagation in biaxial crystals. *J. Opt. A , 1*, 601-616.

Durnin, J. (1987). Exact solutions for nondiffracting beams. I. The scalar theory. *J. Opt. Soc. Am. A , 4*, 651-654.

Durnin, J., Miceli, J. J., & Eberly, J. H. (1987). Diffraction-free beams. *Phys. Rev. Lett. , 58*.

Erdélyi, M., & Gajdátsy, G. (2008). Radial and azimuthal polarizer by means of a birefringent plate. *J. Opt. A: Pure Appl. Opt. , 10*, 055007(6pp).

Fresnel, A. J. (1866). *Ouvres completes.* Paris: L'Imprimerie Impériale.

Hamilton, W. R. (1837). Third supplement to an essay on the theory of systems of rays. *17*, 1-144.

Herman, R. M., & Wiggins, T. A. (1991). Production and uses of diffraction free beams. *J. Opt. Soc. Am. A , 8* (6), 932-942.

Huygens, C. (1690). *Traité de la lumiére.* Van der Aa.

King, T. A., Hogervorst, W., Kazak, N. S., Khilo, N. A., & Ryzhevich, A. A. (2001). Formation of higher order Bessel light beams in biaxial crystals. *Opt. Commun. , 187*, 407-414.

Kozawa, Y., & Sato, S. (2005). Generation of a radially polarized laser beam by use of a conical Brewster prism. *Opt. Lett. , 30* (22), 3063-3065.

Lai, W. J., Lim, B. C., Phua, P. B., Tiaw, K. S., Teo, H. H., & Hong, M. H. (2008). Generation of radially polarized beam with a segmented spiral varying retarder. *Optics Express , 16* (20), 15694-15699.

Landau, L. D., Lifshitz, E. M., & Pitaevskii, L. P. (1984). *Electrodynamics of continuous media* (2nd ed.). Pergamon press.

Li, X. F., Winfield, R. J., O'Brien, S., & Crean, G. M. (2009). Application of Bessel beams to 2D microfabrication. *Appl. Surf. Sci. , 255*, 5146-5149.

Lloyd, H. (1833). *Phil. Mag. , 1*, 112-120 and 207-210.

Lunney, J. G., & Weaire, D. L. (2006). The ins and outs of conical refraction. *Europhys. News , 37*, 26-29.

Maruo, S., Nakamura, O., & Kawata, S. (1997). Three-dimensional microfabrication with two-photon-absorbed photopolymerization. *Opt. Lett , 22*, 132-134.

O'Dwyer, D. P., Phelan, C. F., Rakovich, Y. P., Eastham, P. R., Lunney, J. G., & Donegan, J. F. (2010). Generation of continuously tunable fractional optical orbital angular momentum using internal conical diffraction. *Optics Express , 18* (16), 16480-16485.

Park, S. H., Yang, D. Y., & Lee, K. S. (2009). Two photon stereolithography for realizing ultraprecise three dimensional nano/microdevices. *Laser & Photon. Rev. , 3*, 1-11.

Peet, V. (2010(b)). Biaxial crystal as a versatile mode converter. *J. Opt. , 12*, 095706 (4pp).

Peet, V. (2010(a)). Improving directivity of laser beams by employing the effect of conical refraction in biaxial crystals. *Optics Express , 18* (19), 19566-19573.

Peet, V., & Zolotukhin, D. (2010). Free-space evolution of focused Gaussian beams transformed by conical diffraction in a biaxial crystal. *Opt. Commun. , 283* (15), 3011-3016.

Phelan, C. F., O'Dwyer, D. P., Rakovich, Y. P., Donegan, J. D., & Lunney, J. G. (2009). Conical diffraction and Bessel beam formation with a high optical quality biaxial crystal. *Optics Express , 17*, 12891.

Portigal, D. L., & Burstein, E. (1969). Internal conical refraction. *J. Opt. Soc. Am. , 59*, 1567-1573.

Potter, R. (1841). An examination of the phaenomena of conical refraction in biaxial crystals. *Phil. Mag. , 18*, 343-353.

Pujol, M. C., Rico, M., Zaldo, C., Solé, R., Nikolov, V., Santos, X., et al. (1999). Crystalline structure and optical spectroscopy of Er^{3+}-doped $KGd(WO_4)_2$ single crystals. *Appl. Phys. B , 68*, 187-197.

Quabis, S., Dorn, R., Eberler, M., Glokl, O., & Leuchs, G. (2000). Focusing light to a tighter spot. *Opt. Commun , 179*, 1-7.

Saito, Y., Kobayashi, M., Hiraga, D., Fujita, K., Kawano, S., Smith, N. I., et al. (2008). z-Polarization sensitive detection in micro-Raman spectroscopy by radially polarized incident light. *J. Raman Spectrosc. , 39*, 1643-1648.

Tidwell, S. C., Ford, D. H., & Kimura, W. D. (1990). Generating radially polarized beams interferometrically. *Appl. Opt. , 29*, 2234-2239.

Voigt, W. (1905). *Phys. Z , 6*, 672-673.

Warnick, K. F., & Arnold, D. V. Secondary dark rings of internal conical refraction. *Phys. Rev. E ,*

55, 6092-6096.

Youngworth, K. S., & Brown, T. G. (2000). Focusing of high numerical aperture cylindrical vector beams. *Optics Express , 7*, 77-87.

Zhan, Q. (2004). Trapping metallic Rayleigh particles with radial polarization. *Optics Express , 12* (15), 3377-3382.